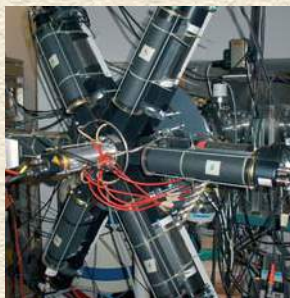
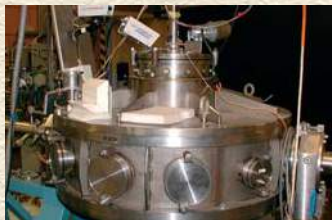


ATOMKI

ANNUAL REPORT

2011



INSTITUTE OF NUCLEAR RESEARCH
OF THE HUNGARIAN ACADEMY OF SCIENCES
DEBRECEN, HUNGARY

INSTITUTE OF NUCLEAR RESEARCH
OF THE HUNGARIAN ACADEMY OF SCIENCES
DEBRECEN, HUNGARY

ANNUAL REPORT
2011



ATOMKI

Postal address:

P.O. Box 51
H-4001 Debrecen,
Hungary

Editors:

I. Rajta
E. Leiter

HU ISSN0 0231-3596

Preface

Nuclear physics was born in 1911 when the atomic nucleus was discovered. The existence of Atomki is also somewhat related, since the founder of the institute (A. Szalay) studied nuclear physics at Rutherford before he came back to Hungary. We devoted the entire Physicists' Days, a one week outreach event of Atomki to the history and future of nuclear physics. This was complemented in June with a traveling exhibition of CERN describing subatomic research for a general audience.

The first half of the year 2011 was also important to the entire country, because of the Hungarian presidency of the Council of the European Union. Atomki shared this work and honor by hosting/organizing events such as the Week of Innovative Regions (WIRE) and the 37th ESFRI (European Strategy Forum on Research Infrastructures) meeting. We had a major facelift of our main lecture hall, it has become a multifunctional hall where different layouts can be arranged depending on the need of the event.

Two major laboratories have been opened in 2011. Our radiocarbon studies are boosted by the new AMS (Accelerator Mass Spectrometer) system developed in ETH Zürich and co-financed by the company Isotoptech Zrt. The primary target of the new device is environmental studies, reflected by its name: EnvironMICADAS. Atomki started a collaboration with the Richter pharmaceutical company, and as a first step our radiochemistry laboratory was renovated and equipped with top of the line instrumentation. This new entity is called PHARMATOM, indicating the synergy between pharma research and Atomki know how. Debrecen, a city where physics meets health industry, has a long range plan to host a proton therapy center. A letter of intent was signed by the interested parties, included Atomki in November 2011.

Among the about 300 publications let me point out one article in Nature, where a nuclear physics experiment was reported by an international collaboration, using the EXOGAM gamma-spectrometer array operational at GANIL, France, complemented by a detector system developed and maintained by Atomki researchers. This shows an important aspect how large and small scale laboratories can collaborate with great success.

The successes of Atomki researchers are recognized nationwide, two examples from 2011 are the Officer's Cross Order of Merit of Hungary received by Prof. R. G. Lovas and the Dennis Gabor Award of Dr. J. Molnár for his achievements in nuclear detector developments.

This year, the Atomki Annual Report features the excellent research of the Section of Experimental Nuclear Physics.

Further details of Atomki events, and back issues of the Annual Reports can be found on our homepage: www.atomki.hu

Debrecen, 25 August 2012



Zsolt Fülöp
Director

Organizational structure of ATOMKI

Director		
Dr. Zsolt Fülöp D.Sc.		
Deputy Directors		Finance Officer
Dr. Béla Sulik D.Sc.	Dr. József Molnár C.Eng.	Dr. Mária Pálinkás
Scientific Secretary: Zoltán Máté, C.Sc. Scientific Secretary: Beáta Király, Ph.D. Technology Transfer Coordinator: Mátyás Hunyadi, Ph.D.		
Scientific Sections		
<ul style="list-style-type: none"> ▪ Division of Nuclear Physics (Head: Attila Krasznahorkay, D.Sc.) <ul style="list-style-type: none"> • Section of Experimental Nuclear Physics (Head: János Timár, D.Sc.) • Section of Ion Beam Physics (Head: István Rajta, Ph.D.) <ul style="list-style-type: none"> ◦ Nuclear Astrophysics Group ◦ Laboratory of Ion Beam Applications • Section of Theoretical Physics (Head: András Kruppa, D.Sc.) 		
<ul style="list-style-type: none"> ▪ Division of Atomic Physics (Head: Ákos Kövér, D.Sc.) <ul style="list-style-type: none"> • Section of Atomic Collisions (Head: László Gulyás, D.Sc.) • Section of Electron Spectroscopy and Materials Science (Head: Kálmán Vad, C.Sc.) <ul style="list-style-type: none"> ◦ Laboratory of Secondary Ion/Neutral Mass Spectrometry 		
<ul style="list-style-type: none"> ▪ Division of Applied Physics (Head: Ferenc Tárkányi, C.Sc.) <ul style="list-style-type: none"> • Section of Environmental and Earth Sciences (Head: László Palcsu, Ph.D.) <ul style="list-style-type: none"> ◦ Hertelendi Laboratory of Environmental Studies ◦ Radon Group ◦ K-Ar Laboratory ◦ QMS Laboratory • UD - ATOMKI Department of Environmental Physics (Head: István Csige, Ph.D.) • Section of Cyclotron Applications (Head: Ferenc Ditrói, Ph.D.) • Section of Electronics (Head: Iván Valastyán, Ph.D.) <ul style="list-style-type: none"> ◦ Computational Group 		
<ul style="list-style-type: none"> ▪ Accelerator Centre (Head: Sándor Biri, Ph.D.) <ul style="list-style-type: none"> • Cyclotron Laboratory • Laboratory of Electrostatic Accelerators • ECR Laboratory • Isotope Separator Laboratory 		
<ul style="list-style-type: none"> ▪ Services <ul style="list-style-type: none"> • Library (Librarian: Mária Nagy) • Accounting (Head: Mrs. J. Makai) • Basic Services and Maintenance (Head: István Katona) • Mechanical Workshop (Head: Zoltán Pintye) • Radiation- and Environmental Protection Group (Head: Gábor Dajkó) 		

Data on ATOMKI

At present the Institute employs 190 persons. The affiliation of personnel to units of organization and the composition of personnel are given below.

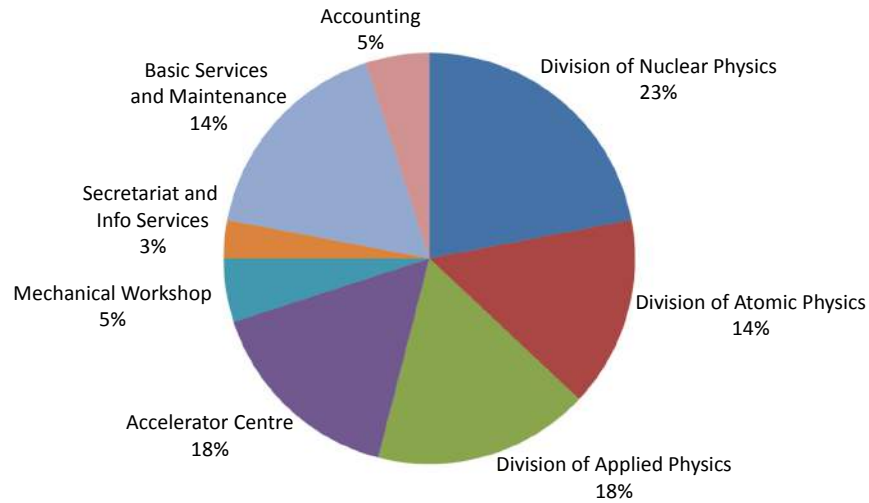


Figure 1. Affiliation of personnel to units of organization

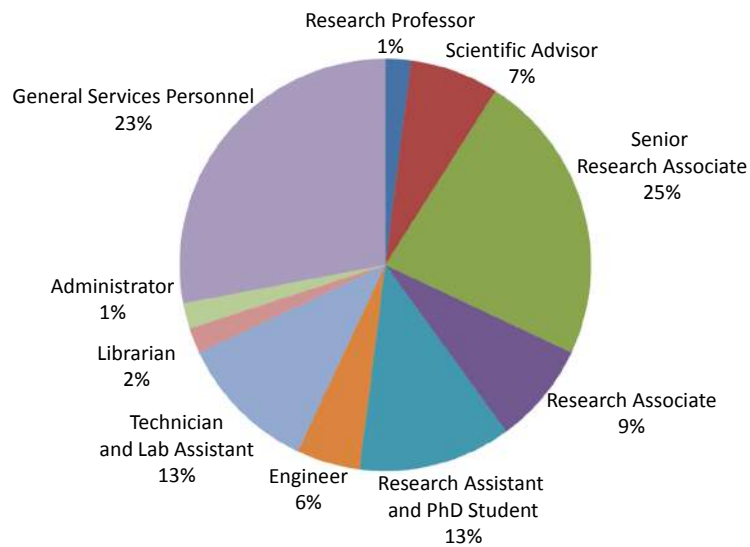


Figure 2. Composition of personnel

International connections

Multilateral international programs: 13

Cooperations based on S&T (TéT) bilateral intergovernmental agreements: 12

Cooperations based on MTA bilateral agreements: 18

Cooperations based on specific collaboration agreements between institutes:

- in nuclear physics and applications with 21 countries in 35 topics
- in atomic physics and applications with 21 countries in 39 topics
- in detection and signal processing technique with 5 countries in 6 topics
- in ion beam analysis with 6 countries in 7 topics
- in environmental research and dating with 12 countries in 14 topics

Membership in international scientific committees: 7

Running research projects, grants

European Research Council (ERC) Starting Grant: 1

Other EU projects: 11

European Organization for Nuclear Research (CERN) projects: 1

International Atomic Energy Agency (IAEA) projects: 2

Intercomparison programs (EURATOM): 2

Hungarian National Research Foundation (OTKA) projects: 14

National Office for Research and Technology (NKTH) projects: 12

Higher education activity

Number of researchers teaching at universities: 32

Number of researchers teaching in doctoral (PhD) schools: 20

Gradual and postgradual teaching: 79 courses, 971 hours

Number of undergraduate students participating in research work (organized by the Student's Science Association, TDK): 14

Number of students making diploma work: 14

Number of PhD students: 20

Supervision activity by Atomki researchers: 2620 hours

Finance

The total budget of the Institute for the year 2011 was 1576 million Hungarian Forints income, and 1469 million Hungarian Forints expenses. The composition of the budget and the share of personnel expenditure within the budget are shown below.

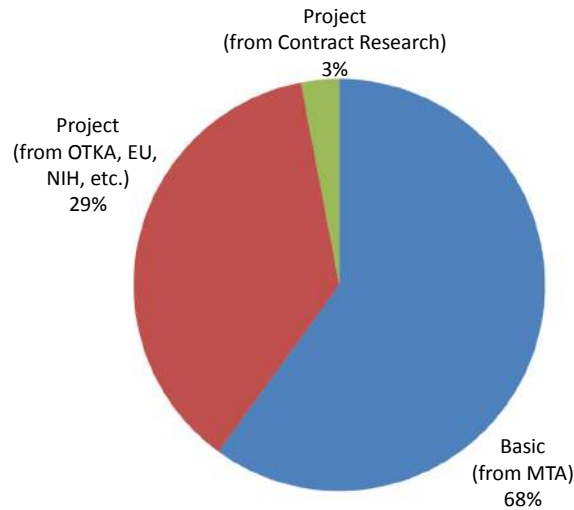


Figure 3. Composition of the budget of the Institute
MTA: Hungarian Academy of Sciences
OTKA: Hungarian Scientific Research Fund
EU: European Union
NIH: National Innovation Office

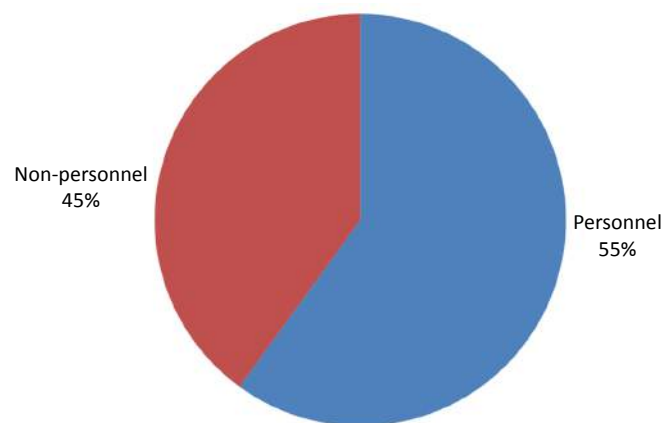


Figure 4. Breakdown of expenditure into personnel and non-personnel expenditures

Table of contents

Preface	i
Organizational structure of Atomki	ii
Data on Atomki	iii
International connections	iv
Running research projects, grants	iv
Higher education activity	iv
Finance	v
Table of contents	vi

Featured:

Research at the Section of Experimental Nuclear Physics of Atomki	1
---	---

1. General Physics

1.1 Systematic survey of a four-parameter subclass of Natanzon potentials	29
---	----

2. Particle Physics

2.1 Bosonization and functional renormalization group approach in the framework of QED_2	30
--	----

3. Nuclear Physics

3.1 On high precision astrophysical factor measurement for the ${}^3\text{He}+{}^4\text{He}$ reaction	31
3.2 Cross section measurements of astrophysically important proton capture reactions on Nitrogen isotopes	32
3.3 The ${}^{106}\text{Cd}$ family problem	33
3.4 Cross section measurements of the ${}^{121}\text{Sb}(\alpha, \gamma){}^{125}\text{I}$ reaction at astrophysical energies	34
3.5 In-beam γ -spectroscopic study of rotational bands in ${}^{132}\text{La}$	35
3.6 High precision determination of the half-life of ${}^{133\text{m}}\text{Ce}$ for nuclear astrophysical application	36
3.7 Medium- and high-spin band structure of the chiral-candidate nucleus ${}^{134}\text{Pr}$	37
3.8 Total reaction cross sections from ${}^{141}\text{Pr}(\alpha, \alpha){}^{141}\text{Pr}$ elastic scattering and α -induced reaction cross sections at low energies	38
3.9 Phase transitions in algebraic cluster models	39

4. Atomic and Molecular Physics

4.1 Ionization of noble gas atoms by H^0 impact	40
4.2 Investigation of MeV proton microbeam transmission between two flat plates – the cases of metallic and insulator plates	41
4.3 Time-resolved photoemission by attosecond streaking: extraction of time information	42
4.4 K-shell ionization of Cu by positron impact	43
4.5 K-shell ionization of copper by proton and antiproton impact	44
4.6 Can positrons be guided by insulating capillaries?	45

4.7	Ionization by intense and short electric pulses - classical picture	46
4.8	State selective electron capture in low energy positron and argon collisions	47
4.9	Iterative solution of the time dependent Schrödinger equation	48
4.10	Energy and angular differential recoil ion spectra in collisions between positron and helium atom	49
4.11	Experimental (e,2e) study of resonant Auger states of Ar	50
4.12	Broadening of electron beams through a single glass macrocapillary	51
4.13	Charge evolution associated with electron transmission through a single glass macrocapillary	52
4.14	Mutual neutralization in low-energy $H^+ + F^-$ collisions	53
4.15	Resonances in photoionization: Cross section for vibrationally excited H_2	54
4.16	Photon energy dependence of left-right asymmetry parameters of Kr 4p photoelectrons in the vicinity of 3d resonant excitations	55
4.17	Interaction between 4p photoionization and 3p resonant excitation channels of krypton	56
4.18	Lifetime measurement of the metastable $1s2s2p^4P_J^o$ state of the He^- ion in a cryogenically cooled electrostatic ion-beam trap	57
4.19	Classical Monte Carlo code for the determination of atomic cross sections for fusion related collision systems	58
4.20	Fragmentation of H_2O and CH_4 molecules induced by 1 MeV N^+ ion impact	59
4.21	Electron cloud simulation of the ECR plasma	60

5. Condensed Matter, Materials Science and Analysis

5.1	Stabilization of intermediate NiSi phase in NiPt/Si(001) and Ni/Pt/Si(001) nanodimensional film compositions	62
5.2	Effect of pressure on photo-induced expansion of $As_{0.2}Se_{0.8}$ layer	63
5.3	Enhancement of photoinduced transformations in amorphous chalcogenide film via surface plasmon resonances	64
5.4	Heat treatment induced structural modification of boron-doped ZnO layers	65
5.5	Determination of chemical state of Al doping element in ZnO layer	66
5.6	Scanning transmission ion microscopy of polycarbonate nanocapillaries	67
5.7	Compaction of PDMS due to proton beam irradiation	68
5.8	Chemical changes in PMMA as a function of depth due to proton beam irradiation	69
5.9	The use of electron scattering for studying atomic momentum distributions: the case of graphite and diamond	70
5.10	Interpretation of eRBS for H quantification at surfaces	71
5.11	Test of image acceleration by distant collision of proton microbeam	72
5.12	Charging dynamics in electron transmission through Al_2O_3 capillaries	73
5.13	Ultrathin tellurium nanowires in polymer assisted solution-phase process	74
5.14	Nucleation and growth dynamics of ultrathin tellurium nanowires	75
5.15	Iron ion implantation into C^{60} layer	76
5.16	Total and angular differential elastic cross sections of fusion related materials	77

6. Earth and Cosmic Sciences, Environmental Research

6.1	Fourth interlaboratory comparison exercise for δ^2H and $\delta^{18}O$ analysis of water samples (WICO2011)	78
6.2	Noble gas constraint on genesis of the multistacked Répcelak $CO_2-CH_4-N_2$ gas field Western-Hungary	79

6.3	Soil C-14 dating of the Lyukas-halom kurgan	80
6.4	C-14 dated paleoenvironmental changes on Lake Kolon during the last 25,000 years . .	81
6.5	Noble gas measurements from 1-3 μ l of AEW	82
6.6	C-14 signal of the Paks Nuclear Power Plant in the nearby treerings	83
6.7	Fossil carbon in the winter time aerosol in Debrecen city, 2010	84
6.8	Chemical characterization of workplace aerosol particles at Atomki	85
6.9	Determination of radioactivity of ^{79}Se in waste of NPP using ^{75}Se as tracer	86
7.	Biological, Chemical and Medical Research	
7.1	Major and trace elements in mouse bone measured by surface and bulk sensitive methods	87
8.	Developments of Methods and Instruments	
8.1	Status report on the accelerators operation	88
8.2	Creation of convex microlenses in PDMS with focused MeV ion beam	91
8.3	Sample holder for studying temperature dependent particle guiding	92
8.4	Feasibility test for production and separation of ^{103}Pd	93
8.5	γ - and X-ray sensitivity comparison of a LEPS and a coaxial HPGe detector for astrophysical γ -process experiments	94
8.6	Simulations for a compact electron-positron spectrometer	95
8.7	Investigation of the absolute full-energy peak efficiency of a large LaBr_3 detector	97
9.	Conferences organized by Atomki	
9.1	International Workshop on Dynamics and Control of Atomic and Molecular Processes Induced by Intense Ultrashort Pulses	98
9.2	The FLAME project in Atomki	99
10.	Appendix	
10.1	Events	100
10.2	Hebdomadal Seminars	101
10.3	Awards	103
10.4	List of Publications	104
10.4.1	Highlights	104
	Author index	106

Research at the Section of Experimental Nuclear Physics of ATOMKI

A. Krasznahorkay, T. Fényes, Zs. Dombrádi, B.M. Nyakó, J. Timár, A. Algora, M. Csatlós, L. Csige, Z. Gácsi, J. Gulyás, M. Hunyadi, I. Kuti, Z. Máté, D. Sohler, L. Stuhl, T. Tornyi, Zs. Vajta, L. Zolnai

1 Introduction

Nuclear physics research was started in Debrecen by Alexander Szalay (1909-1987) back in the 30's. He had been a postdoc of the Nobel-laureate biologist Albert Szent-Györgyi in Szeged and of Lord Rutherford in Cambridge. ATOMKI was founded in Debrecen later, in 1954. The Institute was meant to pursue scientific research in certain areas of experimental nuclear physics and to develop research instruments

In the early years the country was pretty isolated, but the institute's state of isolation was gradually easing up from the mid-sixties. During the period 1962-1975 the research work was performed in collaboration with Joint Institute for Nuclear Research (Dubna), where up-to-date high-energy accelerators were available for the production of desired isotopes.

After finishing the construction of a home-made 5 MV Van de Graaff accelerator (1972) and later on the installation of a K=20 light ion cyclotron (1985) the Institute has become the main centre of accelerator-based nuclear physics in Hungary. In the period 1975-1995 our group performed extensive nuclear structure studies in Debrecen by using γ and conversion electron spectroscopy. At the same time fruitful collaborations were initiated with Jyväskylä (Finland), with University of Kentucky and University of Zagreb.

In 1993 the former Nuclear Reaction Group (NRG) merged with our group. Parallel with this structural change, the main topics of our γ -spectroscopic work has also changed, which resulted that the location of our experiments were shifted from the home institute to foreign large-scale facilities.

New topics were brought partly by the emerging NRG, partly by group members returning from postdoctoral fellowships. They also brought important non γ -spectroscopic topics, which enriched our research palette. These new topics have by now become joint endeavours involving more and more group members.

The Nuclear Physics European Coordination Committee (NuPECC) has recently stated that the aim of present-day nuclear physics is to explore the origin, development, phases and structure of strongly interacting matter. Our group is studying the structure and dynamics of atomic nuclei, which is still one of the most important chapters of nuclear physics.

The traditions of the group are strong in experiments with accelerators. Our knowledge and experience are the strongest in detection techniques, including nuclear electronics, in electronic and computerised processing of measured data, in the planning of experiments by simulation and in data evaluation. This experience has been obtained through research work in various fields in conventional nuclear structure physics and through measurements and theoretical evaluation of nuclear reaction experiments. The above experience played an important part both in the local experiments and also in the experiments performed in bigger nuclear physics laboratories.

In spite of the economic crisis, we have maintained and updated our own experimental instruments in ATOMKI. Recently, in the National Inventory and Road Map of Research Infrastructure (NEK-IFUT) the Laboratory for Nuclear and Astrophysics at ATOMKI (MAGAL) has been qualified as strategic research infrastructure. The front cover of this report shows a few important instruments of MAGAL. We strongly believe that building and using new instruments in ATOMKI plays a very important role also in teaching the new generation.

After a short review of the works performed before 1995, we will concentrate mostly on the current nuclear physics topics of the group.

Our achievements during the past decade can be briefly characterised by the following statistical facts. We have performed many experiments, among which in about 30 we were spokespersons or co-spokespersons. These resulted about 280 articles which have received about 1500 citations. The results have been presented in 23 invited talks in nuclear-physics conferences, and served as a basis for 5 PhD and 3 DSc theses. In ATOMKI we also organised three international conferences.

2 Historical survey

The present Section of Experimental Nuclear Physics has grown out of the α -spectroscopic research group (later Nuclear Spectroscopy Department) of ATOMKI. The group was organized in 1962 with leadership of Tibor Fényes. The research work of the Section till 1995 can be divided in two parts. First period 1962-75: α -, γ -, and conversion electron spectroscopic studies based on the 680 MeV phasotron and U-400M heavy ion cyclotron of the Joint Institute for Nuclear Research, Dubna (JINR). Second period 1975-95: Complex nuclear structure studies based on the 5 MV Van de Graaff and MGC isochronous cyclotron accelerators of ATOMKI.

2.1 The philosophy of research

2.1.1 Period 1962-75

- Construction of a special spectrometer at home in ATOMKI and using it in Dubna, where unique accelerators could produce the desired isotopes. This spectrometer was a semiconductor Si(Li) α -spectrometer (with a special β -ray background suppression), new in Eastern-Europe that time.
- Search for new α -emitting isotopes in unconventional regions (among the rare earth elements and below ^{82}Pb).
- Application for the identification of investigated isotopes chemical separation, on-line thermochromatographic method and electromagnetic separator (in the case of spallation products), and excitation function measurements, recoil product collection with He gas sweeping technique (in the case of heavy ion reactions).
- Performance of the measurements in Dubna, and carrying out the evaluation of experimental results and nuclear structure calculations partly in Debrecen.

2.1.2 Period 1975-95

- Construction of special spectrometers for nuclear spectroscopic studies. These were: a superconducting magnetic transporter Si(Li) spectrometer (unique worldwide) and a minorange permanent magnet spectrometer for conversion electron studies, both built in ATOMKI.
- Investigation of the structure of nuclei with in-beam spectroscopic method, i.e. excitation of nuclear levels in nuclear reactions and study of the decay of products in the accelerator beam. This technique allowed to excite by order(s) of magnitude more levels in the investigated isotope, than in radioactive decay.
- In order to get as much as possible information on the structure of the investigated nucleus, performance of many different measurements: γ -spectrum, conversion electron spectrum, γ -ray angular distribution, different types of coincidence measurements, excitation function, Hauser-Feshbach analysis etc. See Fig. 1.

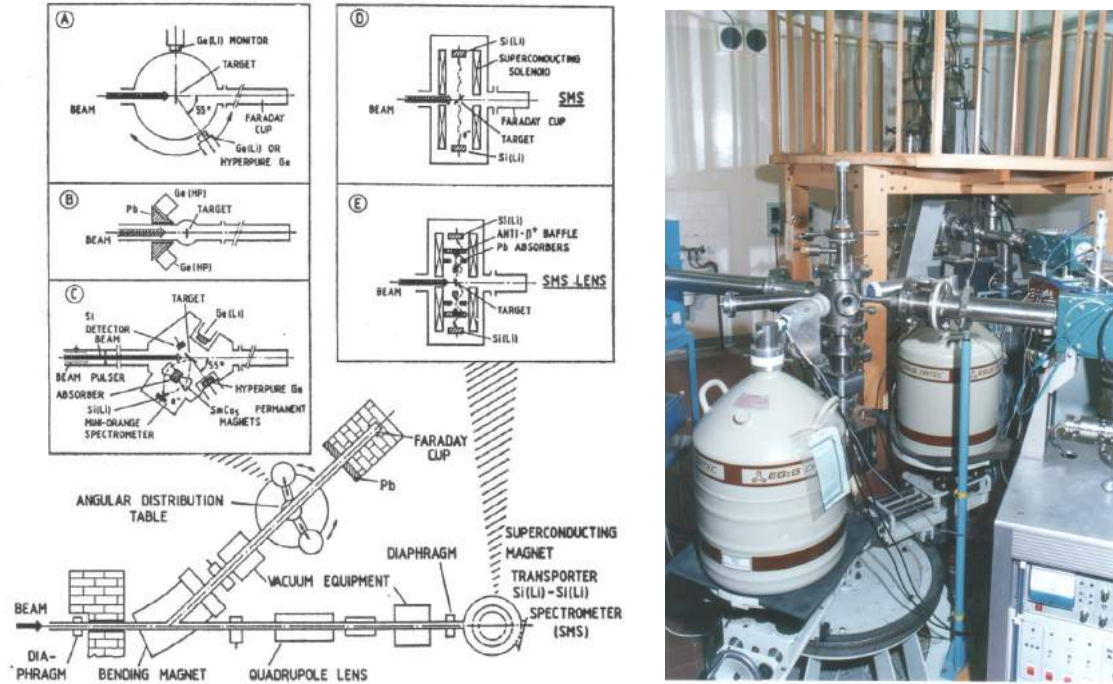


Figure 1. Layout of the γ - and electron-spectroscopic beam channels of the Debrecen K=20 cyclotron; reaction chambers, spectrometers and types of measurements. SMS: superconducting magnet transporter Si(Li)-Si(Li) electron spectrometer. See refs. [1,2].

- Investigation of odd-Z, odd-N nuclei, which have many excited levels, rarely studied formerly.
- Study of whole nuclear regions (not only single nuclei), both experimentally and theoretically. It was a great success, that the performed nuclear structure calculations could properly describe hundreds of nuclear level characteristics, static and transitional properties of many nuclei using the same input parametrization in the model. This is much more difficult, than the interpretation of some properties of single nuclei, but it gives much more information for the understanding of nuclear structure.

2.2 Results

2.2.1 Period 1962-75

The main results of this period were:

- α -spectroscopic study of about half-hundred isotopes of 16 elements. Determination of the characteristics of α -radiation at ≈ 30 Eu, Gd, Tb, Dy, Pt, Au, Hg, Bi, Po isotopes. First identification of fine-structure α -radiation in the rare earth region.
- Discovery of eight new Au, Hg, and Tl isotopes, furthermore two long-lived isomeric states.
- Complex nuclear spectroscopic study of eight light Tl isotopes. Observation of about 240 new Tl γ -radiation, determination of the multipolarities of radiations and other properties of the decaying nuclei. Nuclear structure calculation of the investigated daughter mercury isotopes and drawing conclusions on their structure.

The results were published in ≈ 30 scientific papers in this period, mainly in *Izv. AN SSSR, ser. fiz., Yadernaya Fizika, Phys. Rev.* etc. See for example refs. [3-5].

2.2.2 Period 1975-95

The main results of this period were:

- Complex in-beam study of ^{45}Sc , $^{97,98,100}\text{Tc}$, $^{94,96}\text{Nb}$, ^{76}As , ^{82}Br , ^{70}Ga nuclei in the external beam of the ATOMKI 5 MV Van de Graaff accelerator. Observation of more than half-hundred new γ -radiation in the Sc and Tc isotopes and determination of their properties.
- The structure of $^{114,112,110,108,106}\text{In}$ nuclei was studied with complex γ and electron spectroscopic methods via $(p,n\gamma)$ and (in cases of $^{112,110}\text{In}$) $(\alpha,n\gamma)$ reactions at 4.8-17.1 MeV bombarding particle energies. The bombarding p- and α -beams were extracted from the ATOMKI cyclotron. New level schemes have been deduced. The energy splitting of proton-neutron multiplet states of $^{116,114,112,110,108,106}\text{In}$ was calculated on the basis of the “parabolic rule”, and the results have been compared with the existing experimental data. The energy spectra and electromagnetic properties of odd-odd $^{116-106}\text{In}$ nuclei were calculated in the framework of the interacting boson fermion-fermion/odd-odd truncated quadrupole phonon model (IBFFM/OTQM). The main systematic trends and changes in nuclear structure have been reasonably well described by the theory. See ref. [1].
- The structure of $^{112,114,116,118}\text{Sb}$ nuclei was studied also with complex γ and electron spectroscopic methods via $(p,n\gamma)$ and also $(\alpha,n\gamma)$ reactions (in the case of $^{116,118}\text{Sb}$ at 5.5-9.2 MeV proton and 14.5-16.0 MeV α -particle energies. New level schemes have been deduced. The energy splitting of the proton-neutron multiplet states of $^{116,118,120,122,124}\text{Sb}$ was calculated on the basis of the “parabolic rule”. Many p-n multiplet states have been identified and conclusions have been drawn on the applicability of the parabolic rule as simple guideline for experimental investigations.

Detailed description of the energy spectra and electromagnetic properties of $^{116,118,120,122,124}\text{Sb}$ nuclei was given on the basis of the interacting boson-fermion-fermion/odd-odd truncated quadrupole phonon model (IBFFM/OTQM). The calculations give account both of the regular and irregular behaviour of the energy splitting of the p-n multiplets (see Fig. 2), as well as of the electromagnetic moments, γ -branching and γ -mixing ratios. Conclusions have been drawn on the role of different interactions in the multiplet energy splitting.

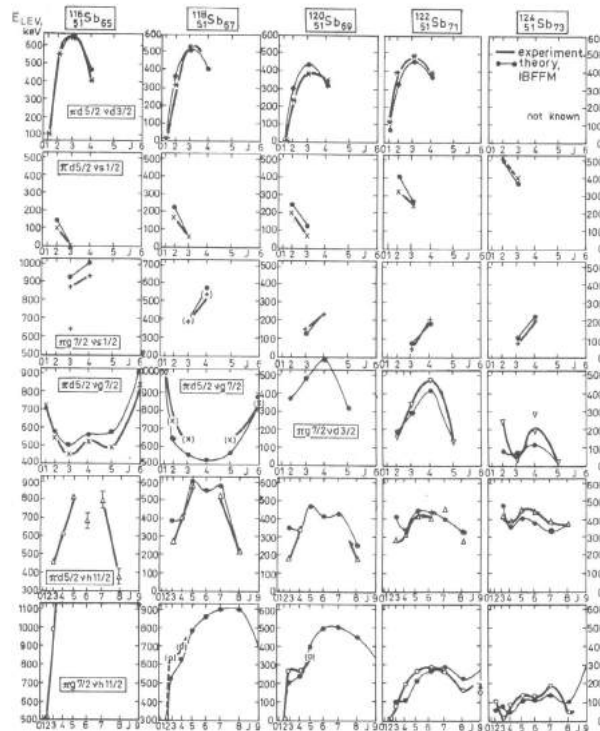


Figure 2. Systematics of energy splitting of different p-n multiplets in $^{116,118,120,122,124}\text{Sb}$. The abscissa is scaled according of $J(J+1)$, where J is the spin of the state. From [6].

The IBFFM interpretation of the high-spin intruder bands and the spectroscopic factors of the neutron transfer reactions are discussed for Sb nuclei. See ref. [6].

– The structure of $^{66,68,70}\text{Ga}$, $^{70,72,73,74,76}\text{As}$ was studied via $(p,n\gamma)$ (and in some cases) $(\alpha,n\gamma)$ reactions. In-beam γ -ray, two dimensional $\gamma\gamma$ -coincidence, internal conversion electron, and γ -ray angular distribution spectra, as well as $\sigma(E_{lev}, E_p)$ relative reaction cross sections were measured with Ge(HP), Ge(Li) γ and combined superconducting magnetic plus Si(Li) electron spectrometers at different bombarding particle energies. The proposed new level schemes contain 300 (among them 70 new) levels. Level spins, parities, γ -ray branching and mixing ratios have been deduced. Energy spectra, electromagnetic moments, reduced transition probabilities, γ -ray branching ratios, and one-nucleon transfer reaction spectroscopic factors were calculated in the framework of interacting boson model (IBM), interacting boson-fermion model (IBFM), and interacting boson-fermion-fermion model (IBFFM) for about 20 nuclei in the Ga-As region ($^{64-67}\text{Zn}$, $^{65-68}\text{Ga}$, $^{68-73}\text{Ge}$, $^{70-74}\text{As}$). The odd-odd nuclei were described on the basis of consistent parameterization deduced from the even-even core and the two neighbouring odd-A nuclei. Reasonable description of experimental data has been obtained. The energy splitting of proton-neutron multiplets in odd-odd Ga and As nuclei is discussed also with the use of the parabolic rule, which is associated with IBFFM in low perturbation order.

The energy spectra of $^{74}\text{Se}_{40}$, $^{75}\text{Se}_{41}$, $^{73}\text{As}_{40}$, $^{74}\text{As}_{41}$, supermultiplet nuclei were calculated on the basis of the $U_\pi(6/12) \otimes U_\nu(6/12)$ supersymmetry (SUSY) theory, using a simple closed energy formula. 44 states of these four different nuclei have been reasonably described using only 7 fitted parameters, see Fig. 3. The existence of supersymmetry was supported also by one-nucleon transfer reaction data, electromagnetic properties, as well as by IBFM, IBFFM and SUSY model wave functions of the levels considered. See ref. [7] and Fig. 3.

In summary ≈ 1500 new γ -radiations were observed and their properties have been determined.

In the second period of research about 66 scientific papers have been published. Some of them are listed in ref. [1-2, 7-17]. A comprehensive theoretical interpretation of the obtained results has been given in the book T. Fényes: Structure of atomic nuclei [18]. By-products of the investigations were also two other books: T. Fényes et al.: Nuclear physics [19], and T. Fényes: Particles and their interactions [20].

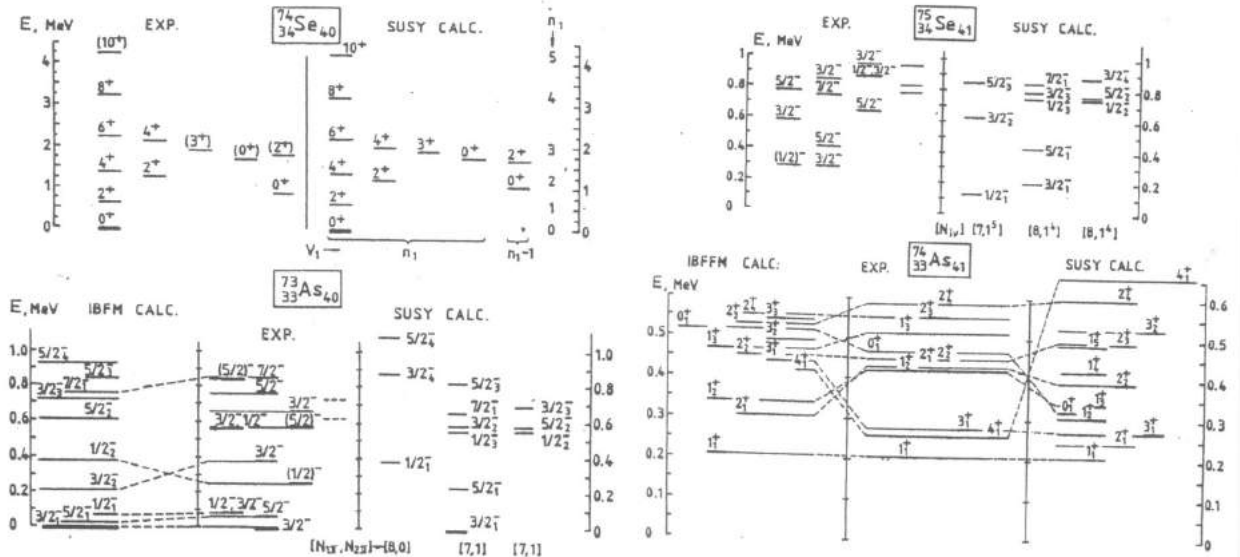


Figure 3. Experimental, IBFM, IBFFM and supersymmetry (SUSY) theoretical results on the level schemes of ^{74}Se , ^{73}As , ^{75}Se , ^{74}As . 44 states of these four supermultiplet nuclei have been reasonably described using only 7 fitted parameters of the supersymmetry theory. From [7], further refs. can be found in this article.

3 Super- and hyperdeformed states in the actinide region

A new line of experimental research was started in Debrecen by A. Krasznahorkay when, in 1992, a split-pole magnetic spectrograph was received from Vrije Universiteit, Amsterdam, as a gift. The spectrograph was installed at the Cyclotron Laboratory in the ATOMKI, it was equipped with a new focal-plane detector, and new data-acquisition system was built with the use of modern electronics.

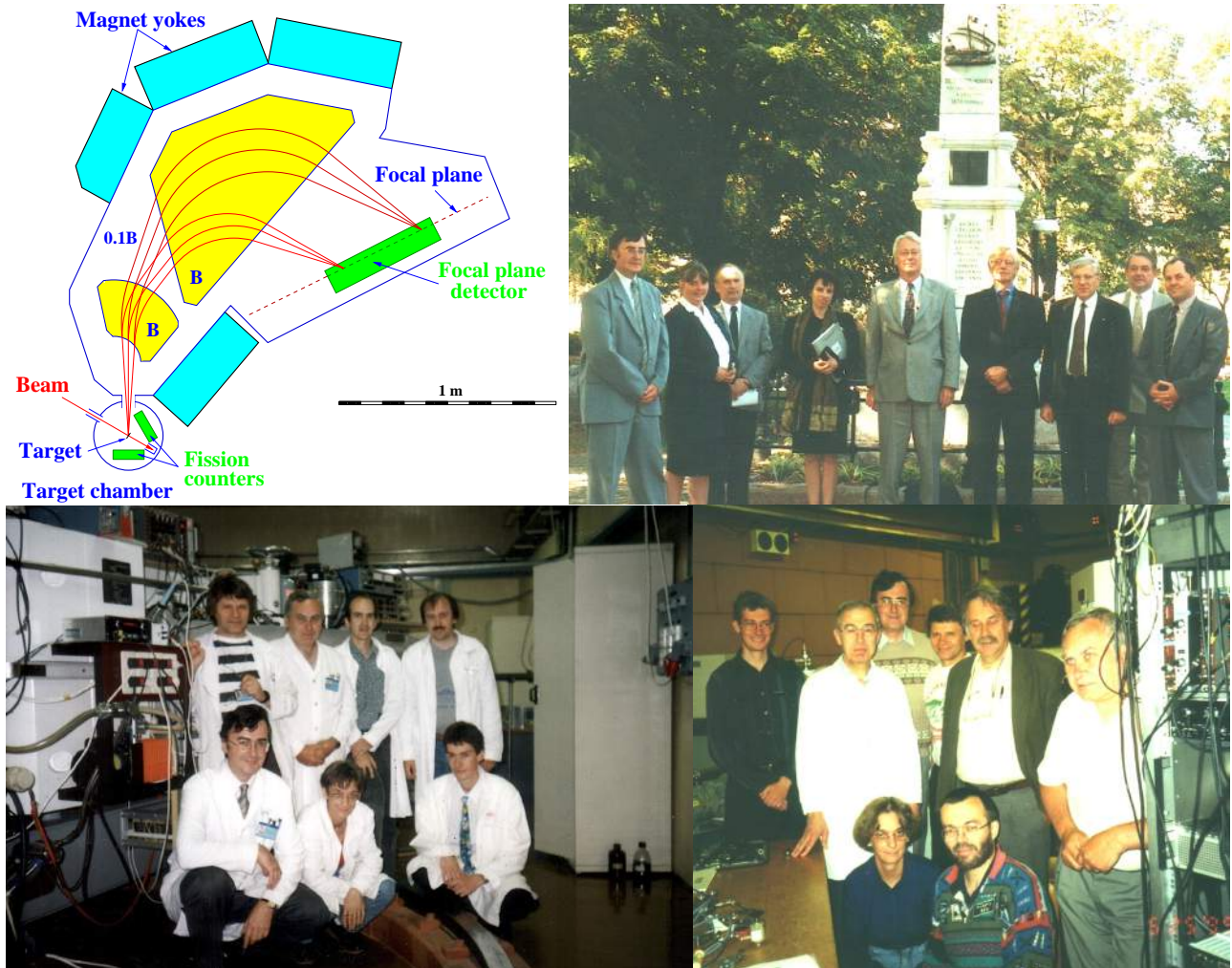


Figure 4. Working principle and dimensions of the split-pole magnetic spectrograph, a few members of the Dutch NWO (Ministry of Education) delegation, who supported the transport of the spectrograph to Debrecen, and the experimental groups (including Hungarian and Dutch members) who performed the first experiments with the spectrograph in ATOMKI.

This combination of a high-current accelerator and a magnetic spectrometer turned out to be an efficient tool for studying low cross section nuclear reactions.

One of the new projects using the unique possibility of this combination is the investigation of hyperdeformed states (states with a ratio of 3:1 for the long to the short axis) formed in the course of fission. These studies are complementary to the searches for hyperdeformed high-spin states, for which 4π γ -arrays are used elsewhere, but up till now indications for the existence of hyperdeformed bands have only been found, without any individual states identified. In a fissioning system hyperdeformed states may be accessible if the energy between the fission fragments as a function of the interfragment distance, interpreted as a potential, has at least three minima, and the third minimum is deep enough

to accommodate quasibound levels. Fig 5 schematically shows the potential-energy surface (PES) of ^{236}U as a function of deformation (axis ratio) with the triple-humped fission barrier as we deduced previously.

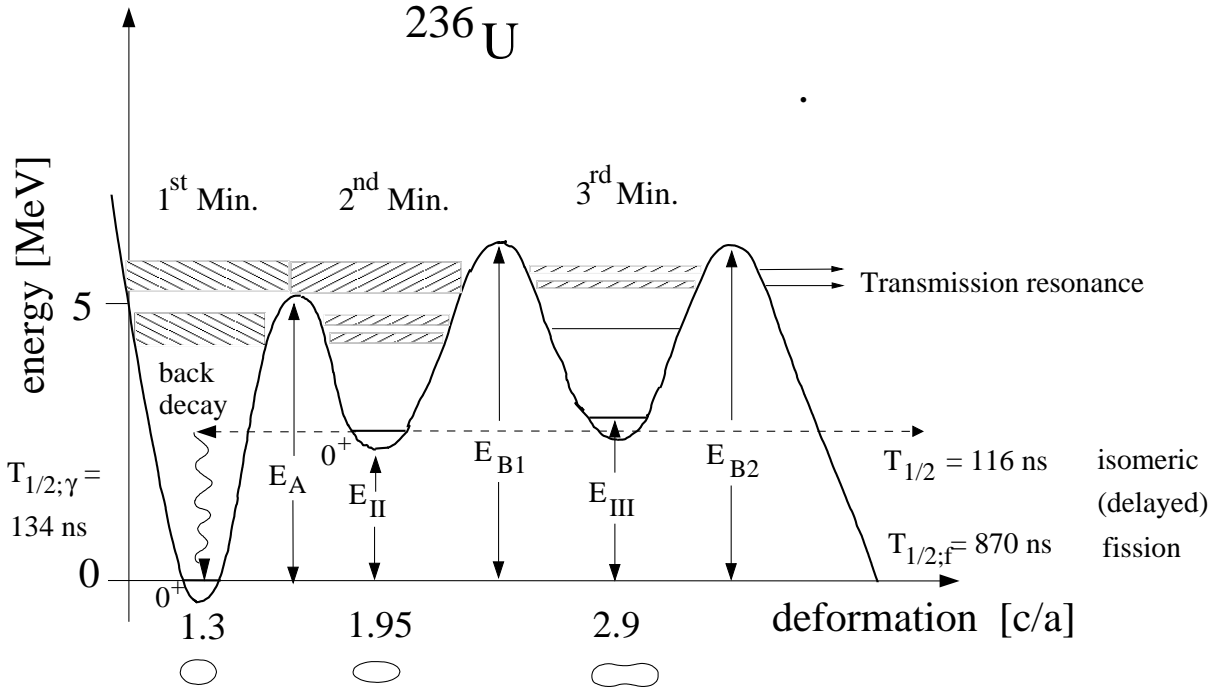


Figure 5. The triple-humped potential-energy surface of ^{236}U . Also damped class-I, class-II and class-III compound states are shown in the three minima. For strongly mixed class-I and class-II states, transmission resonances of class-III states can occur in fission.

Such states may be reached by exciting a fissioning state by a low-energy reaction. These states, viewed as rotational states, have moments of inertia compatible with axis ratio 3:1. We prepared fissioning states of ^{236}U by (d,p) reaction on ^{235}U and measured the fission probability as a function of the excitation energy below their fission barriers [21, 22, 23, 24]. The resonant tunneling effect caused peaks in the fission probability when the excitation energy on the nucleus was equal with an excited state in the third minimum. This effect was used for mapping the hyperdeformed states in the third minimum of the fission potential (see ref.[25] for more details). The basic measurements were done in Debrecen and were repeated with better energy resolution in Munich [24].

In Debrecen the energy of the outgoing protons was analysed by the split-pole magnetic spectrograph, and the fission fragments were detected in coincidence by two home-made position-sensitive avalanche detectors. These detectors have two wire planes, with delay-line read-out, corresponding to the horizontal and vertical directions. Rotational bands were found, with parameters corresponding to hyperdeformed shapes. Some representative results are shown below for ^{236}U taken from refs.[24, 26].

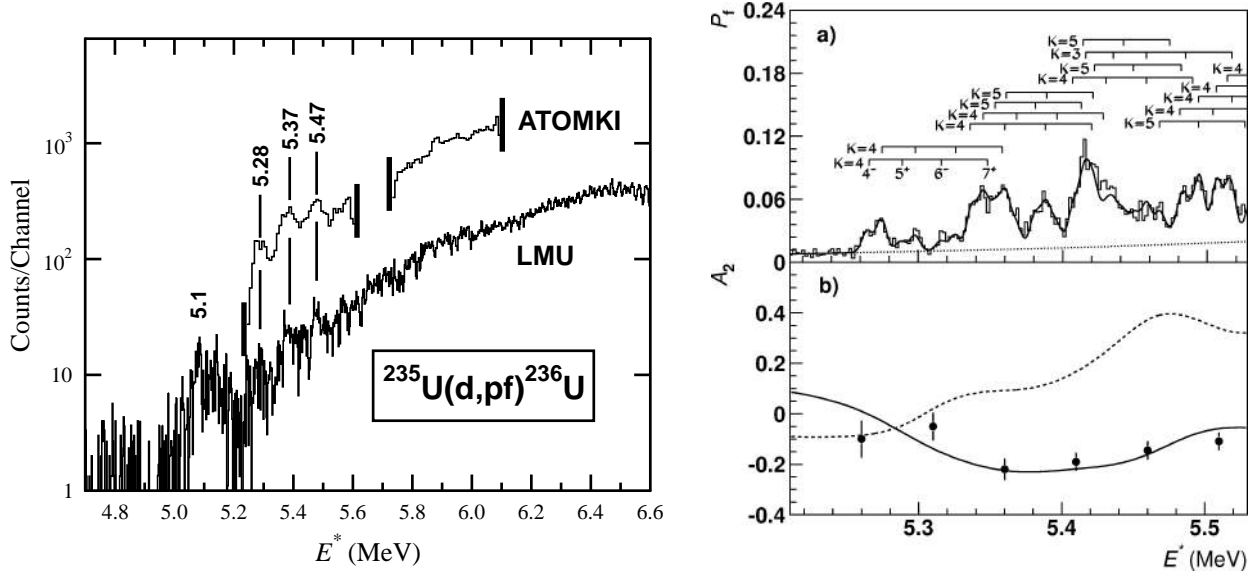


Figure 6. The first proton spectra measured in coincidence with the fission fragments in Debrecen (ATOMKI) and in Munich (LMU). a) Fission probability compared with fitted rotational bands as a function of the excitation energy; b) measured and calculated angular distribution coefficient (A_2) as a function of the excitation energy

In 1996 we started a very successful collaboration with the Physics Department of the Ludwig Maximilians University, where we could do high resolution measurements with a Q3D magnetic spectrograph, and could use highly radioactive actinoid targets for the investigations as well (see in Fig. 7).



Figure 7. Repairation of our position sensitive fission detectors after radiation damage and their installation into the scattering chamber of the Q3D spectrograph.

A great number of super- and hyperdeformed bands were found in ^{240}Pu [27, 28, 32] ^{234}U [30, 31, 33], ^{236}U [21, 22, 23, 24, 26] and ^{232}U [34] as well as in ^{232}Pa [37]. They are built on high-lying, possibly two-particle, excitations. The observed level density and the excitation energy of the "ground state" in the third minimum, deduced for the first time, are consistent with the theoretical predictions.

Nuclear fission is quite a complicated large-scale collective motion. In spite of several decades of intense work, the experimental information on nuclear fission is still rather limited. The fission of nuclei of this region presents a very rich variety of nuclear shapes. The fissioning nucleus undergoes a continuous sequence of nuclear surface shapes from more or less spherical to elongated, followed by super- and/or hyperdeformed shapes, then neck and split into two fission fragments. The fission potential, which holds the two fragments together, is very complicated and has a lot of structure (minima, maxima, and saddle points) as a function of its parameters. If the energy of the system is lower than the fission barrier, the system can spend more time in the different potential minima and one can study the cold nuclear system under such extreme conditions.

We have pioneered in the survey of the fission potentials of heavy nuclei by studying hyperdeformed fissioning states systematically. This potential plays a key role in the performance of nuclear power stations, especially in the generation IV reactors, whose operation involves a variety of processes [25].

An outstanding result connected also this line, which is obtained recently [35] is that a long-standing contradiction between the experimental and theoretical decay heat values of ^{239}Pu in nuclear reactors has been resolved by a measurement which combines the total γ -absorption detection method, the ion guide isotope separation (IGISOL) technique and a Penning trap.

We have also published experimental results also on the genuine ternary fission of ^{234}Pa [36]. The mass of the light product has been found to be 20-40 amu.

We are planning to continue these studies also in the future. The vacuum system, the high current power supply as well as the focal-plane detector (see in Fig. 8) of the Debrecen spectrograph was upgraded recently.

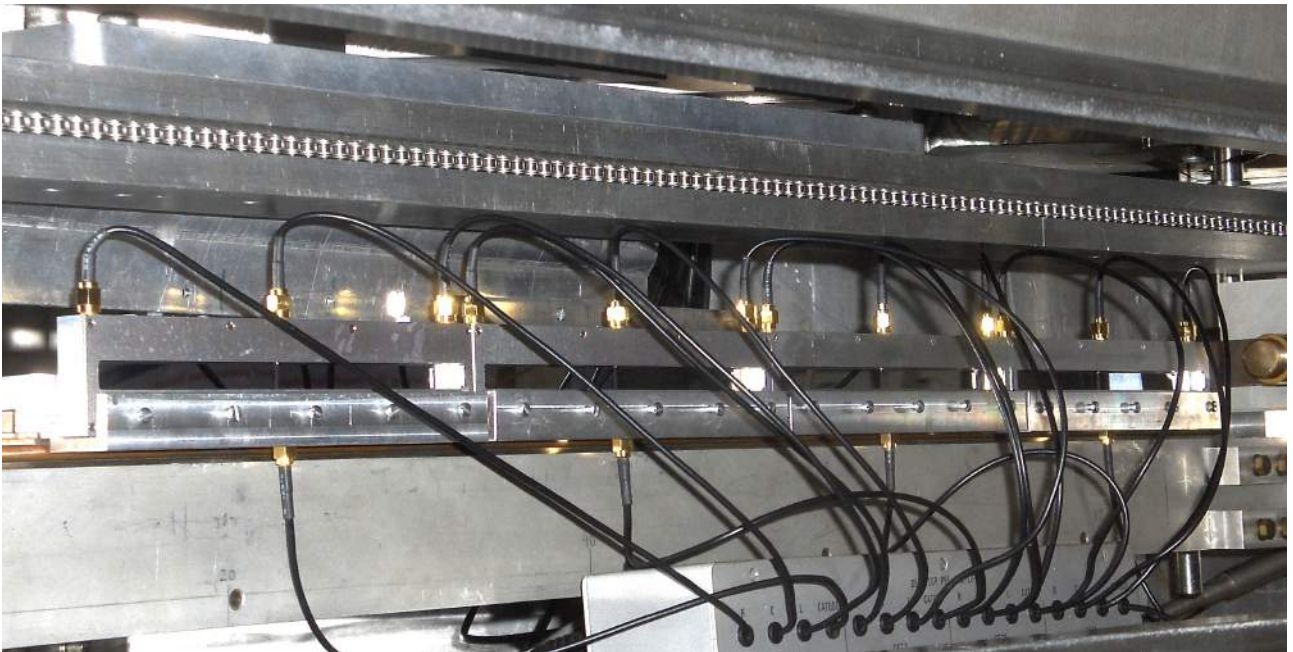


Figure 8. A new $4 \times 18 = 72$ cm long position sensitive Si detector at the focal plane of the spectrograph.

We have just received more than hundred of high quality radioactive actinoid targets from Munich, which will open up new avenues for the fission research in Debrecen soon. We are planning to study systematically the fission probability as a function of the excitation energy not only for even nuclei, but for odd and odd-odd nuclei as well to get a systematic behaviour of the fission potential, the level densities in the second and third minimum of the fission potential, and the possible clusterization effects connected to the highly deformed states.

We are planning to study the fission process also in abroad, in the largest accelerator labs. Since the discovery of nuclear fission, experimental studies on low-energy fission have been restricted to about 80 fissionable nuclei. They represent only about 15 % of all known nuclei with $Z \leq 82$. However, recently a novel experimental technique has been introduced at GSI. The fission of relativistic secondary projectiles has now been studied in flight. The benefit of the radioactive beams for studying the fission process is clear and we are planning to use the advantages of this method for studying the process in a wider mass range.

The fission of neutron-rich exotic nuclei will be studied at the laser centre for nuclear physics in Bucharest (ELI-NP). Fission resonances as well as pygmy dipole resonances may be studied by exciting them by high-energy γ -rays. Before the ELI-NP becomes available such investigations are started up at the high-energy γ -ray source HI γ S at Duke University.

4 Study of the neutron-rich nuclear matter with giant resonances

Neutron-rich nuclei present a challenge to our understanding of the systematic behaviour of nuclei. Contrary to the proton drip-line region, our knowledge on the neutron drip-line is limited to the lightest systems. That is where neutron halos have been discovered, which are very extensive and dilute one or two-neutron orbits around compact cores, occupied by the least bound one or two neutrons. For heavier neutron-rich nuclei it is expected that there is a bulk of neutron matter overflowing the volume of the self-conjugate core. The primary empirical information that can be obtained on these phenomena is the neutron skin thickness.

At the beginning of the 90's A. Krasznahorkay was a postdoc at KVI Groningen (the Netherlands) and started to study high-energy collective excitations of nuclei, the giant resonances. They have developed a new method for determining the neutron skin thicknesses i.e., the difference between the radii of the neutron and proton densities.

The inelastic excitation of the giant dipole resonance (GDR) via the isoscalar α projectile was introduced to measure the neutron-skin thickness [38]. The cross section of this process depends strongly on $\Delta R_{pn}/R_0$, the relative neutron-skin thickness. Unfortunately, the cross section of the IVGDR excitation is very small relative to those of other overlapping resonances. Thus, $\alpha - \gamma$ coincidence measurements are needed to extract the small IVGDR cross sections [39, 40].

After his return to ATOMKI the experiments were continued in an ATOMKI-KVI collaboration using the new superconducting accelerator AGOR and the new Big Bite Spectrometer (BBS) (shown in Fig. 9) at KVI [41, 42, 43, 44].

M. Hunyadi (A. Krasznahorkay's former PhD student) became also a postdoctoral fellow at KVI and continued to study giant resonances there. They have published many common articles on giant resonances and their decay properties.

Gamow-Teller as well as spin dipole giant resonances of several nuclei were studied [45]. The proton and neutron emission from an isoscalar dipole giant resonance was observed for the first time [46, 47, 48]. A broad resonance was found at higher energies; based on angular distribution measurements it was inferred to have quadrupole structure. The estimates show that this may be identified with the first upper harmonic mode of the well-known giant quadrupole resonance. In their measurements and analyses new methods have been introduced.

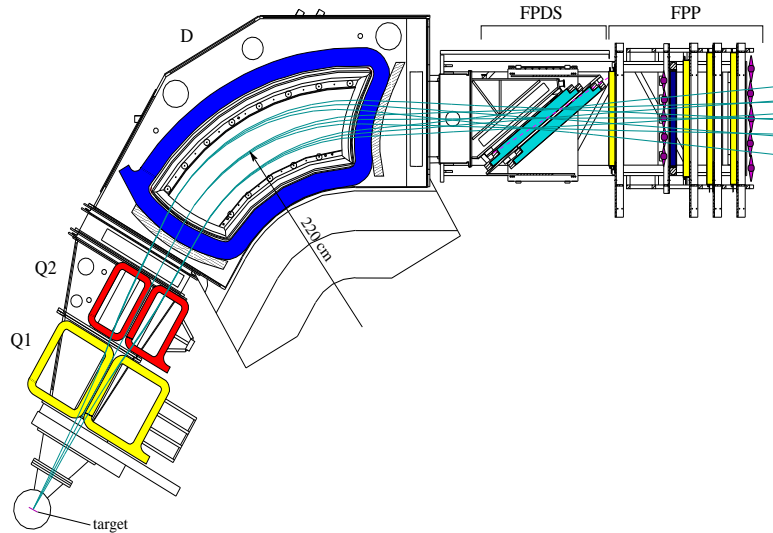


Figure 9. Schematic drawing of the large BBS and the members of the Hungarian group.

A. Krasznahorkay continued to study the neutron-skin thicknesses also at RCNP, Osaka. He introduced another method there to measure this very small difference between neutron and proton distributions [49]. They have demonstrated experimentally that the correlation between the cross section of the spin-flip giant dipole resonance and the neutron-skin thickness of nuclei is predictable, as it is based on a model independent sum-rule [49].

Using the Grand Raiden (GR) spectrometer at RCNP high resolution experimental data has been obtained recently for the $^{40,42,44,48}\text{Ca}(^3\text{He},t)\text{Sc}$ charge exchange reaction at 420 MeV beam energy. The measured angular distributions were analyzed for each state separately, and the relative spin dipole strength has been extracted for the first time. The low-lying spin-dipole strength distribution in ^{40}Sc shows some interesting periodic gross feature. It resembles to a soft, damped multiphonon vibrational band with $\hbar\omega = 1.8$ MeV, which might be associated to pairing vibrations [50].

Giant resonances can provide information not only on the structure of individual nuclei but on the equation of state of nuclear matter as well [51]. Especially, the nuclear symmetry energy ($S(\rho)$) plays a central role in a variety of nuclear phenomena. It determines to a large extent the equation of state (EoS) and the proton fraction of neutron stars, the neutron skin in heavy nuclei, it enters as an input

in the analysis of heavy ion reactions, etc. Its value at nuclear saturation density seems reasonably well established, both empirically as well as theoretically; still different parameterizations of relativistic mean-field (RMF) models (which fit observables for isospin symmetric nuclei well) lead to a relatively wide range of predictions for the symmetry energy, 24 - 40 MeV.

However, predictions for its density dependence show a substantially larger variation. Recently, it has been pointed out by several authors that there exists a strong correlation between the neutron skin, $\Delta R_{pn} = R_n - R_p$, and the density derivative of the EoS of neutron matter near saturation density. Subsequently, in a more detailed analysis in the framework of a mean-field approach, Furnstahl [52] demonstrated that in heavy nuclei there exists an almost linear empirical correlation between theoretical predictions in terms of various mean-field approaches to $S(\rho)$ (i.e. a bulk property) and the neutron skin, ΔR (a property of finite nuclei).

This observation has contributed to a renewed interest in an accurate determination of the neutron skin in neutron-rich nuclei for several reasons. First, precise experimental information on the neutron skin could help to further constrain interaction parameters that play a role in the calculation of the symmetry energy [53]. Furthermore, a precise value of the neutron skin is required as an input in several processes of physical interest, e.g., the analysis of energy shifts in deeply bound pionic atoms, and in the analysis of atomic parity-violation experiments (weak charge).

In a very recent experiment we performed at GSI (S408, Spokesperson: A. Krasznahorkay) another method was used. The aim of the experiment was to study the energy of the antianalog of the giant dipole resonance (AGDR) excited in the $^{124}\text{Sn}(p,n)$ reaction performed in inverse kinematics. The energy of the AGDR was estimated by RPA calculations, and realized its strong ΔR_{pn} dependence, which we used to constrain the ΔR_{pn} of ^{124}Sn .

The experiments were performed at GSI using 600 MeV/nucleon ^{124}Sn relativistic heavy-ion beams on 2 and 5 mm thick CH_2 targets. The ejected neutrons were detected by a low energy neutron array (LENA) [54] ToF spectrometer, which was developed in Debrecen and which was placed at 1 m from the target and covered a laboratory scattering angle region of $65^\circ \leq \Theta_{LAB} \leq 75^\circ$. Such type of neutron spectrometer has been built recently also by Beyer et al. and by Perdikakis et al. and has been used recently as an effective tool for studying Gamow-Teller giant resonances in radioactive nuclear beams. The energy of the de-exciting γ -transitions were measured by six large ($3.5'' \times 8''$) (at this moment the largest in the world) state-of-the-art LaBr_3 γ -detectors placed at $\Theta_{LAB} = 24^\circ$ in order to use the advantage of the large Lorentz-boost. The large Doppler shift ($E_\gamma/E_0 = 2.2$) was taken into account in the analysis. The precise energy and efficiency calibration of the detectors were performed after the experiments by using different radioactive sources and (p, γ) reactions on different targets [55].

Part of the experimental setup together with the Hungarian participants is shown in Fig. 10.

The beam is coming from the right of the figure and hits the target in the spherical target chamber. The large LaBr_3 are seen at forward angle, while the LENA detectors stand at about 70° at forward angle at both sides and also at the top of the beam pipe. In the background the Large ALADIN (a large dipole magnet) is seen.

The γ -ray energy spectrum measured in coincidence with the low-energy neutrons is shown in Fig. 11. The energy distribution of the γ -rays was fitted by a Gaussian curve and a linear background, and the obtained parameters are shown in the figure.

The energy of this transition ($E_0=10.6$ MeV) differs significantly from the energy of the GDR ($E_{GDR}=15.19$ MeV) and turned out to be very sensitive to the neutron-skin thickness (ΔR_{pn}). Our calculations performed with state-of-the-art self-consistent random-phase approximation (RPA), based on the framework of relativistic energy density functionals support also such strong ΔR_{pn} sensitivity of the energy of the AGDR.

By comparing the theoretical results calculated as a function of ΔR_{pn} and the measured energy of the AGDR, the ΔR_{pn} value was deduced to be 0.26 ± 0.02 fm, which agrees nicely with the previous results. The energy of the AGDR measured previously for ^{208}Pb was also used to determine the ΔR_{pn}

for ^{208}Pb . In this way a very precise $\Delta R_{pn} = 0.22 \pm 0.02$ neutron-skin thickness has been obtained for ^{208}Pb . The present method offers new possibilities for measuring the neutron-skin thicknesses also in rare-isotope beams [56].

We are planning to continue the above studies later on with radioactive beams produced at FAIR (Facility for Antiproton and Ion Research), which will become soon one of the largest nuclear physics facilities worldwide. FAIR will provide antiproton and ion beams with unprecedented intensity and quality with which a large variety of new experiments will be possible.



Figure 10. Part of the experimental setup together with the Hungarian participants

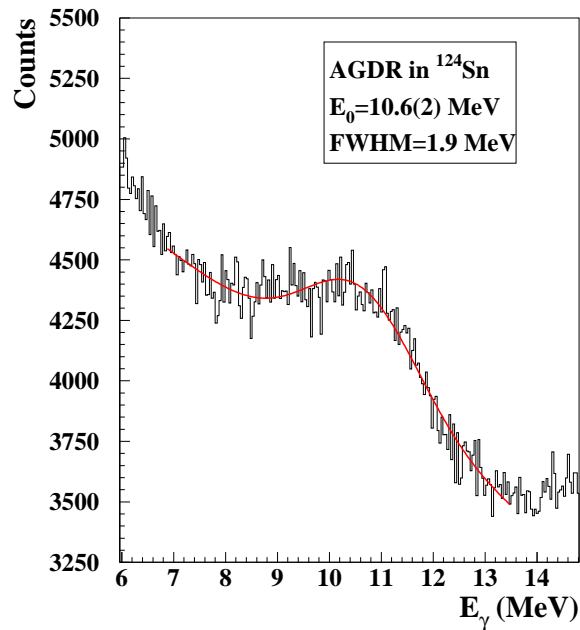


Figure 11. γ -ray energy spectrum measured in coincidence with the low-energy neutrons. The calibrated energy scale was corrected already for the Doppler effect.

5 Gamma-ray spectroscopy of high-spin states

A new research field, the study of high-spin nuclear states commenced worldwide around the late 1970's thanks to the advent of high-energy heavy-ion accelerators and, from the early 1980's, systems of high-purity Ge-detectors equipped with escape-suppression shields. Barna Nyakó, from the Section of Nuclear Reactions of ATOMKI, had the opportunity to participate in the installation and utilization of the first such type of detector systems, the TESSA-s (Total Energy Suppression Shield Array), in the SERC Daresbury Laboratory (DL), UK, while having postdoctoral and research fellowships in the University of Liverpool and DL (1982–1987). He actively contributed to the discovery of the long-sought *high-spin superdeformation* in the otherwise oblate nucleus ^{152}Dy . The observation of a collective superdeformed ridge structure in the energy correlation spectrum of the quasi-continuum γ -rays [57], the identification of the first *discrete-line* superdeformed band [58] upto $\text{spin} \approx 60\hbar$, at a level of $\leq 1\%$ population intensity of the reaction channel, and a triple shape coexistence in this nucleus (the observation of a normal-deformed collective band [59] upto $\text{spin} \approx 40\hbar$) not only indicated the power of using such detector systems, but further motivated the development of more complex, ball-like spectrometers. High-spin superdeformation soon became one of the most studied phenomena worldwide [60], and triggered a renaissance of γ -ray spectroscopy, the nascency of "ball spectroscopy".

The study of superdeformation and other high-spin phenomena has been continued as a new ball-spectroscopy research program in the ATOMKI, as well, and it soon became one of its main research fields. We have been utilizing, within multinational collaborations, the most advanced detector systems operational at large-scale facilities of different European and overseas laboratories. Fruitful partnerships were built with research groups of the University of Liverpool, ISN (Grenoble), CENBG (Bordeaux), MSI (today KTH, Stockholm), GANIL (Caen), the iThemba LABS (South Africa) and SUNY (Stony Brook, USA). We have also been contributing to the success of these collaborations by joining the large European detector development projects, the EXOGAM [62], and, recently, the AGATA [63] collaborations, and by providing one of the ancillary detectors. From 1995 the high-spin spectroscopy programs have been continued in the Section of Experimental Nuclear Physics.

5.1 The DIAMANT light-charged-particle detector system

To support the high-spin research programs, a new R+D project (led by B. Nyakó) was started within an ATOMKI–MSI collaboration around 1990. We planned to develop a high granularity light-charged-particle detector system capable for the determination of the type and the number of the charged particles, i.e., for reaction channel selection when using it as an ancillary detector inside large γ -ray spectrometers, like EUROBALL. An ad hoc research team had been formed in the ATOMKI, including specialists in electronics and detection technique. The CsI(Tl) scintillator was chosen as detector material, as it has an intrinsic particle discrimination capability, the decay time of its scintillation light being particle-type dependent. Based on this property, a novel particle discriminator had been developed [65] and used to build the electronics in the EUROBALL-compatible VXI standard.

Parallel with our work, a team in CENBG (Bordeaux) had developed the DIAMANT [64] detector array. It utilized the same kind of CsI(Tl) detectors, arranged as a forward wall of 8, and a central part of 76 detectors in rhombicuboctahedron geometry. Within a CENBG–ATOMKI–University of Napoli collaboration we decided to upgrade DIAMANT by replacing its traditional electronics with the VXI-based ATOMKI version. The original geometry is kept, but the central part is now based on a flexible PCB holding the detectors and (new type of) preamplifiers (see Fig. 14). For signal processing DIAMANT is equipped with octal particle discriminator modules of VXI standard [66]. Each channel provides the *Energy*, the particle type (*PID*) and the detection *Time* signals. In *particle*–

γ -type coincidence experiments one can create 1D and/or 2D spectra from these signals (see, e.g., the *PID-vs-Energy* spectrum Fig. 12). Putting 1D or 2D ("banana") gates on the particular type of detected particles (proton and alpha-s) in these spectra, one can *select* or *reject* γ -rays in coincidence with particular charged particles "evaporated" in the nuclear reaction used. The 1-proton(1-alpha) detection efficiency of DIAMANT is typically 70%(55%). Due to its high granularity, multi-fold particle evaporation channels can also be selected with high efficiency (for more details see Ref. [67]). DIAMANT was successfully used in our EUROBALL experiments to search for high-spin hyperdeformation and chirality (see later), and in experiments with the EXOGAM and the AFRODITE spectrometers. At present it is maintained by the ATOMKI group. DIAMANT is meant to be one of the standard ancillary detectors of the future EXOGAM2 and AGATA spectrometers.

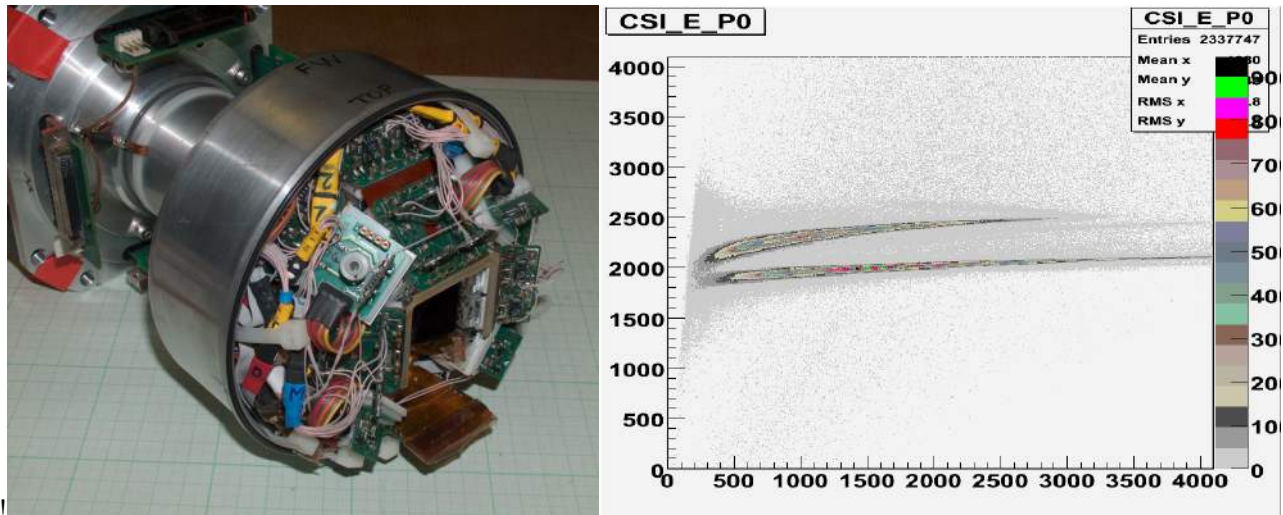


Figure 12. (Left) The central part of DIAMANT prepared for an experiment. (right) a PID-vs-Energy spectrum showing the proton (top) and alpha (bottom) distributions.

5.2 High-spin spectroscopy of super- and hyperdeformed states

The concept of *superdeformed* (SD) nuclear shapes was introduced in connection with the fission isomers, observed in some heavy ($A \approx 240$) nuclei. In analogy with the so-called Jacobi shape transition of classical rotating liquid drops, above certain spins, nuclei can undergo a sudden change from oblate into a highly elongated prolate shape, which can be further stabilized by microscopic effects, as suggested by the Nilsson-Strutinsky shell-correction method. The formation of such a secondary minimum in the nuclear potential energy surface at large prolate deformation, at which the nucleus was called to have a "superdeformed" shape, can explain the existence of fission isomers.

Cranked Nilsson-Strutinsky calculations predicted the existence of secondary minima in other nuclear mass regions as well. In the single-particle energy spectra they are associated with large shell gaps, appearing at special "magic" neutron or proton numbers. In lighter nuclei this second minimum is stabilized by the fast rotation of the nucleus, i.e., they can sustain upto very high spins. The shell gaps are usually crossed by down-sloping deformation-driving high-J intruder orbitals. The most peculiar shell gaps correspond, in the simple harmonic oscillator model, to nuclear axis ratios of 3:2, 2:1 and 3:1 called highly-deformed, superdeformed and hyperdeformed shapes, respectively.

Superdeformation at high spins is manifested in the γ -ray spectra as a long cascade of closely (and almost equally) spaced transitions, reflecting the fast rotation of a very elongated nucleus the moment of inertia of which is much larger than that of normal-deformed nuclei. The relevant nuclei with highly-deformed and SD shapes can have quadrupole deformations of $\beta_2 \approx 0.4$ and 0.65 , respectively, compared to the typical values of $\beta_2 \approx 0.1-0.2$ of normal-deformed prolate nuclei.

The detailed study of superdeformation in ^{152}Dy revealed several unusual features of the discrete-line SD band [71]. Its measured quadrupole moment corresponded to a rigid-like rotation of a nucleus having $\beta_2 \approx 0.65$ prolate deformation, reflected in an almost constant moment of inertia upto spins $\approx 60\hbar$, where an enhanced feeding is observed in a narrow spin range; it has then a nearly constant intensity down to the bottom of the band, where it has a sudden intensity drop, suggesting a decay-out mechanism of statistical nature (see inset of Fig. 15).

The use of the new generation advanced γ -ray spectrometer arrays enabled, e.g., the observation of further SD bands including excited SD bands in different mass regions, the discovery of identical SD bands having transition energies which are identical within a few keV along two bands, and the observation of a $\Delta I = 4$ bifurcation in the transition energies of certain SD bands, all awaiting proper theoretical descriptions and further experimental data.

The existence of stable hyperdeformed (HD) nuclear shapes, or a third minimum in the potential energy surface at a quadrupole deformation of $\beta_2 \approx 0.9$ was predicted by Dudek et al. [82] soon after the discovery of high-spin superdeformation in ^{152}Dy , however, around the highest spins a nucleus can accommodate. This was followed by several experimental attempts trying to identify HD structures in those nuclei predicted to have HD minima.

Members of our group have been involved in experiments utilizing mainly the European spectrometers, the TESSA-s, the EUROGAM, the EUROBALL-s (with which the DIAMANT ancillary detector was also used), and the GAMMASPHERE in the US. We had essential contributions to and new observations in the spectroscopy of SD states in the $A \approx 130, 150$ and 190 mass regions, as follows. We have also been involved in studies aiming at the search for HD structures in different nuclei, using the largest spectrometer arrays, the EUROBALL-s and GAMMASPHERE.

Superdeformation in $A \approx 130$ nuclei: We have identified two excited superdeformed bands in ^{132}Ce [68], and another one in ^{131}Ce [69]. In $A \approx 130$ nuclei these were the first excited SD bands identified. These bands together with the yrast (yr) SD bands form the $^{131}\text{Ce}(\text{yr})$ – $^{132}\text{Ce}(2)$, the $^{132}\text{Ce}(3)$ – $^{131}\text{Ce}(\text{yr})$ and the $^{132}\text{Ce}(\text{yr})$ – $^{131}\text{Ce}(2)$ pairs of identical bands, which gave also a first evidence for the existence of identical SD bands in this mass region. Later on all these SD bands have been further extended to extremely large spins [70], using data from our EUROBALL experiment.

Superdeformation in the $A \approx 150$ region: We have studied the decay-out mechanism of the SD bands in ^{152}Dy [72] and ^{151}Tb [73] using the TESSA3 and the EUROGAM spectrometers, respectively. Although no discrete-line decay-out paths could be found, by comparing the decay-out patterns of the known SD bands in neighboring $A \approx 150$ nuclei we have concluded that in this mass region neutron pairing correlations and the occupancy of high- N intruder orbitals strongly affect the statistical tunneling mechanism in the decay-out. We made also an accurate measurement of the intensity distributions and the γ -ray energies of the SD bands in ^{151}Tb . We have observed identical SD bands in ^{151}Tb [73] and ^{142}Sm [76]. We have shown that in the ^{151}Tb case the identical bands decay out at the same spin, contrary to the yrast SD bands (see right panel of Fig. 13).

In ^{147}Gd we have identified four new superdeformed bands in a EUROGAM II experiment [74]. Three of the new SD bands were interpreted as a neutron excitation with the proton configuration remaining unchanged. These bands are part of a data set of 14 SD bands which was used to identify Nilsson orbitals below the magic $N = 86$ neutron shell gap and to investigate the effect of the crossing of the $[642]5/2$ and $[651]1/2$ neutron orbitals.

In ^{154}Er a new prolate deformed SD band has been identified [75] using the EUROBALL spectrometer at LNL, Legnaro. As the previously observed SD band in ^{154}Er was proposed to be based on a triaxial shape, these two bands represent the first observation of coexisting structures at prolate superdeformed and triaxial highly-deformed shapes.

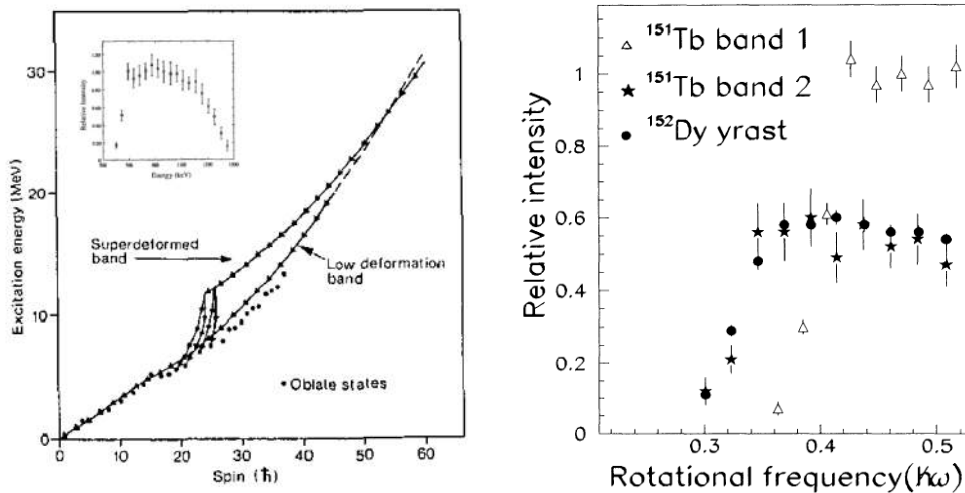


Figure 13. (Left) Schematic illustration of the decay-out of SD band as statistical-like cascades; inset: Intensity distribution of SD transitions in ^{152}Dy . (right) Relative intensities for the SD bands in ^{151}Tb and ^{152}Dy

Evidence for octupole vibrations in a superdeformed $A \approx 190$ nucleus: In the beginning of the 1990's no rotational band was known to be built on a collective vibration of the nucleus in its superdeformed shape. Calculations, however predicted that $A \approx 150$ and 190 nuclei could have octupole softness in their SD minima, manifested experimentally in the existence of excited SD band(s) connected to the yrast SD band by strong E1 transitions.

Our group has been involved in solving this problem by the identification of an octupole vibrational SD band in ^{190}Hg , performing a series of experiments in wide international collaboration. First, using EUROGAM II array, we identified an excited SD band in ^{190}Hg which decays through several linking transitions to the SD yrast band [77, 78]. Later, performing a lifetime experiment with the GAMMASPHERE, we proved, that if the linking transitions have E1 multipolarities, then their $B(E1)$ reduced transition probabilities are so large that can only be expected for an octupole vibrational band [79]. Finally, using EUROBALL IV, we have determined the multipolarities of the strongest linking transitions, which proved to be E1 [80].

We also successfully identified direct linking transitions between the SD and ND minima in ^{190}Hg [81]. Based on this, the excitation energy and the spin of the SD states could be proposed making it possible to compare SD two-proton separation energies in this mass region.

Search for high-spin hyperdeformation: First we studied ^{152}Dy , in which the first HD ridge structure with $\Delta E_\gamma \approx 30$ keV and a tentative discrete-line HD sequences were seen earlier [83]. In the experiment performed, we populated ^{152}Dy using a reaction enabling proton-tagging and the EUROBALL III array [85]. The "HD" ridge was found to be in coincidence with transitions in the yrast SD band, but discrete-line rotational bands could not be identified. We also initiated a research program at EUROBALL to search for HD structures in some Hf isotopes, using the DIAMANT in order to investigate the role of charged particle emission in the population and decay of HD states. Later on we became co-proposers of the so-called Hyper-Long-Hyper-Deformed (HLHD) experiment, performed in a large collaboration, using the EUROBALL-IV array, equipped with an Inner Ball γ -calorimeter, and the DIAMANT ancillary detector. The aim was to search for HD structures in nuclei around ^{126}Ba [86], which were populated in the symmetric $^{64}\text{Ni} + ^{64}\text{Ni} \Rightarrow ^{128}\text{Ba}^*$ fusion reaction. Two bombarding energies, $E_{beam} = 255$ and 261 MeV, were used to reach the highest angular momentum that the compound nuclei can accommodate. To get proper statistics for the expectedly very weak discrete-line HD transitions, two weeks of beamtime was allocated for both energies.

The purpose of using DIAMANT was to tag γ -rays in coincidence with the emitted light charged particles. They were then used to *clean* the xn-type data by vetoing on "particle- γ " coincidences, and to *select* particle-xn-type data by gating on the particular charged-particle combinations [87]. Both type of data have been analysed using two-dimensional γ -energy correlation and 3-dimensional rotational plane mapping methods to search for hyperdeformed and other rotational ridges.

No discrete-line HD rotational bands have yet been identified, some very interesting results emerged from the analysis. In the case of xn-type data the population of the observed ridge structure (for ^{126}Ba) depends very sensitively on the bombarding energy, i.e., it is much stronger in the 261 MeV data, which indicate the importance of entrance channel effects in populating the relevant (SD) structure [86].

The most interesting results of the data analysis was the observation of rotational ridges in the quasi-continuum spectra with two kinds of dynamical moments of inertia. Ridges were observed in seven nuclei with moments of inertia $J^{(2)} \sim 71\text{-}83 \hbar^2/\text{MeV}$, which most likely corresponds to superdeformed structures [88]. In addition, in the same reaction, a higher value of $J^{(2)} \geq 100 \hbar^2/\text{MeV}$ was obtained for the moments of inertia in four other nuclei, namely in ^{118}Te , ^{124}Cs , ^{125}Cs and ^{124}Xe , which are most probably *hyperdeformed*. All of them are produced after charged particle emission, i.e. in the $(2\alpha 2n)$, $(p3n)$, $(p2n)$ and $(2p2n)$ reaction channels, indicating the possible importance of charged particle emission in the population of HD states [89].

We carried out another experiment with the GAMMASPHERE (in 2007) the aim of which was to search for hyperdeformation in ^{124}Xe and neighboring nuclei. Particularly, it was expected that discrete-line HD bands could be observed in this nucleus, as its HD ridge structure was found to be very intense from the analysis of the charged-particle gated data in our HLHD experiment. Although in the applied cold fusion reaction of ^{48}Ca on ^{80}Se excited states at the highest spins were populated, until recently no such HD bands have been identified in the ongoing analysis. The data provided, however, new information on the high-spin structure of several nuclei.

5.3 Chirality in nuclei

Chirality appears in molecules composed of more than four different atoms and is typical for the biomolecules. In molecules it is of static nature because it characterizes the geometrical arrangement of the atoms. Chirality is also encountered in particle physics where it has a dynamical character, since it distinguishes between the parallel and anti parallel orientation of the spin with respect to the momentum of massless fermions. Nuclear chirality is resulting from an orthogonal coupling of three angular momentum vectors in triaxial nuclei. Hence the chirality of nuclear rotation results from a combination of dynamics (the angular momentum) and geometry (the triaxial shape). In the simplest case three perpendicular angular momenta can be generated in triaxially deformed odd-odd nuclei having the unpaired nucleons in particle-type and hole type quasiparticle states. The quasiparticle contribution to the total energy of the nucleus is minimized when the angular momentum of the particle and hole align along the short and the long axis of the core, respectively. The third angular momentum component is provided by the collective core rotation and aligns along the axis of the largest moment of inertia which is the intermediate axis for a triaxial nucleus. Three perpendicular angular momentum components can, however, also be formed in more complex systems. For example, in three-quasiparticle configurations of odd-A nuclei, the two like valence nucleons can have a significant angular momentum component perpendicular to the angular momentum of the odd valence nucleon and to the rotational angular momentum of the triaxial core. Such a case is illustrated in the top left panel of Fig. 16. The experimental signature of nuclear chirality is the observation of two almost degenerate $\Delta I=1$ rotational bands (called chiral bands) having the same parity and similar electromagnetic properties. It is illustrated in the left panel of Fig. 14.

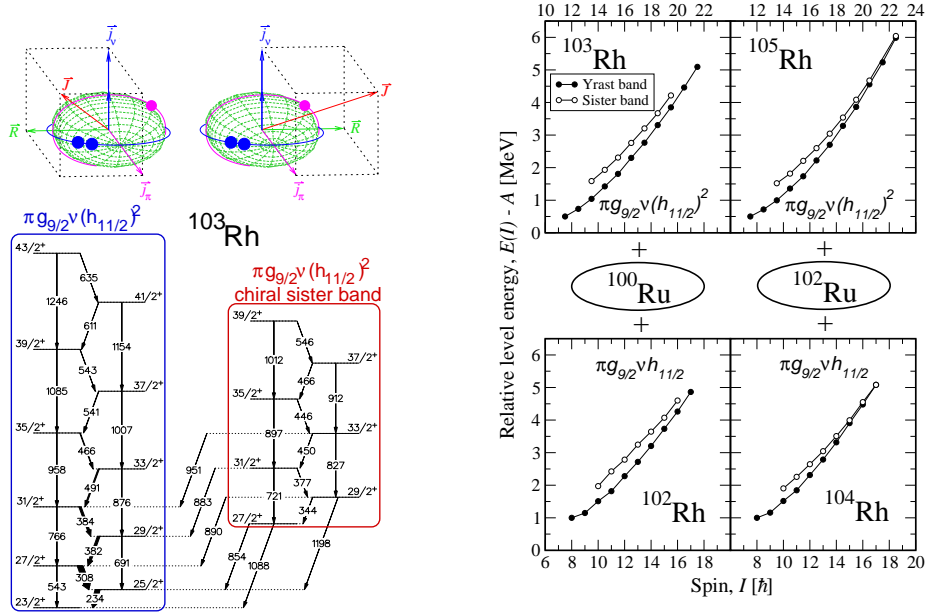


Figure 14. Orientations of the angular momenta in three-quasiparticle chiral case and an example band structure (left). Energy displacement of chiral partner bands in a special quartet of nuclei (right).

Our group studies the possibility of nuclear chirality in several nuclei belonging to three different mass regions where it is expected according to the theoretical predictions. We have built fruitful collaborations with several laboratories (University of York, SUNY, Stony Brook, University of Liverpool, University of Notre Dame, iThemba Labs, Tohoku University) and carried out experiments at large-scale facilities in wide international collaboration using state-of-the-art γ - and particle-detector systems.

In the $A \approx 100$ mass region we have identified chiral-candidate band structures in the $^{102-106}\text{Rh}$ nuclei [90, 91, 92]. To excite the high-spin states of these nuclei we have used fusion-evaporation reactions. The experiments were performed using the GAMMASPHERE, EUROBALL and DIAMANT γ -ray and particle detector systems. Our results proved that in this mass region chiral-candidate band structures also appear in odd-mass $^{103,105}\text{Rh}$ nuclei besides the odd-odd Rh nuclei, confirming the chiral interpretation of the observed doublet bands. We have shown that Rh nuclei around ^{104}Rh form a chiral island with stable chirality in the center and chiral vibration at the border. Observation of chiral-candidate doublet band structures in the $^{102-105}\text{Rh}$ quartet of nuclei enabled us to conclude in a model independent way that the properties of these doublet bands depend strongly on the properties of the nuclear core and only to a lesser extent on the quasiparticle configuration of the chiral bands. The right panel of Fig. 16 compares the energy displacement of the chiral partner bands belonging to the same core but different quasiparticle configurations, as well as to the same configurations but different cores. To investigate the core nuclei in this chiral region, we have studied the high-spin states of ^{102}Ru [93] and ^{104}Pd [94]. We have also studied Ag nuclei in this region, and found that ^{105}Ag is out of the chiral island [95]. In order to confirm the chiral nature of the observed doublet bands in the $^{103,104}\text{Rh}$ isotopes, we have performed lifetime experiments [96], however no conclusive results could be derived for the lifetimes in the yrare partner bands. We plan further lifetime studies to confirm or reject the chiral interpretation in this region.

In the $A \approx 130$ mass region the ^{134}Pr and ^{132}La nuclei were the first chiral-candidate nuclei. Recent lifetime experiments revealed that the deformations of the doublet bands are different, thus they cannot be chiral partner bands. We also have studied these nuclei in wide international collaboration using

the GAMMASPHERE and EUROBALL spectrometers to gain more information on the nature of the doublet bands, and in general of the structure of these nuclei. In ^{134}Pr we have identified several new rotational bands and placed all the new and previously known bands relative to the newly determined ground state [97]. Among the new rotational band, a band was found to have the same configuration as the previous chiral-candidate structure. This band is linked with many transitions to the other two same-configuration bands. This finding provided a new challenge for theory which now needs to account for nearly degenerate band multiplet instead of band doublet of the same configuration. We plan to search for such band multiplets also in other chiral-candidate nuclei. In ^{132}La we proposed new spin values for the chiral-candidate bands [98]. In this nucleus three high-spin bands have been observed previously that are linked to each other by several transitions. It was suggested that all the three have the same configuration and they are magnetic rotational bands with different planar symmetries and remarkable contribution of collectivity. We have shown that one of them has different configuration, thus the previously suggested description cannot be hold [99].

We have also been involved in searching for chiral-candidate bands in the $A \approx 80$ mass region. We have found doublet band structure in ^{80}Br which probably has a chiral vibrational nature [100] using the AFRODITE spectrometer together with the DIAMANT detector system at iThemba Labs, and also found similar band structure in ^{79}Kr [101] using the HYPERBALL spectrometer at Tohoku University.

5.4 Band termination

Nuclear rotation, in contrast with rotation of molecules and macroscopic objects, cannot survive above a certain rotational frequency, where the rotational band stops at a state called terminating state. This phenomenon is called band termination, and is caused by the inertia forces which change the intrinsic structure of the nucleus at high rotational frequencies. These forces tend to align the angular momenta of the valence nucleons to the direction of the rotational axis. In the terminating state all the angular momenta are aligned as much as it is enabled by the Pauli principle, thus forming a slightly oblate nuclear shape which is symmetrical around the rotational axis. Since quantum mechanical rotation around the symmetry axis is not allowed, the terminating state is a non-collective state with a maximal spin value that can be built from the individual spins of the valence particles in the actual configuration. This terminating state is fed by irregular energy γ -rays from higher-energy states belonging to other configurations. Such terminating bands are shown in Fig. 15.

Band terminations can be classified according to the energy gain of the levels close to the terminating state relative to the rigid rotor prediction. Band terminations where the level energies are lower/higher than the rigid rotor energies are called favored/unfavored band terminations. These two types were known before our investigations. Favored band terminations were known around ^{158}Er and ^{122}Xe , while unfavored terminations were observed around ^{109}Sb .

We started to study the phenomenon of band termination in a new mass region, at $A \approx 100$ around the ^{102}Pd nucleus using the EUROGAM2 spectrometer in collaboration with the ISN Grenoble, the University of Liverpool, the University of York and the University of Lund. We have found a new type of band termination in this mass region [102]. The characteristics of this rigid-rotor like band termination is that the energy gain approximately follows the rigid-rotor predictions, and the rotational band corresponding to a certain configuration can be observed from the base state to the terminating state. This was not true for the first two types. Also in ^{102}Pd we have identified terminating states corresponding to core-excited configurations for the first time. We have systematically studied the terminating bands in this region, and identified terminating states in ^{101}Ag [103], ^{103}Pd [104], ^{101}Rh [105], ^{102}Rh [106], $^{98,99,100}\text{Ru}$ [107]. Using the systematic data on the terminating states we proposed new value for the single-particle energy difference of the neutron $d_{5/2}$ and $g_{7/2}$ orbitals [107].

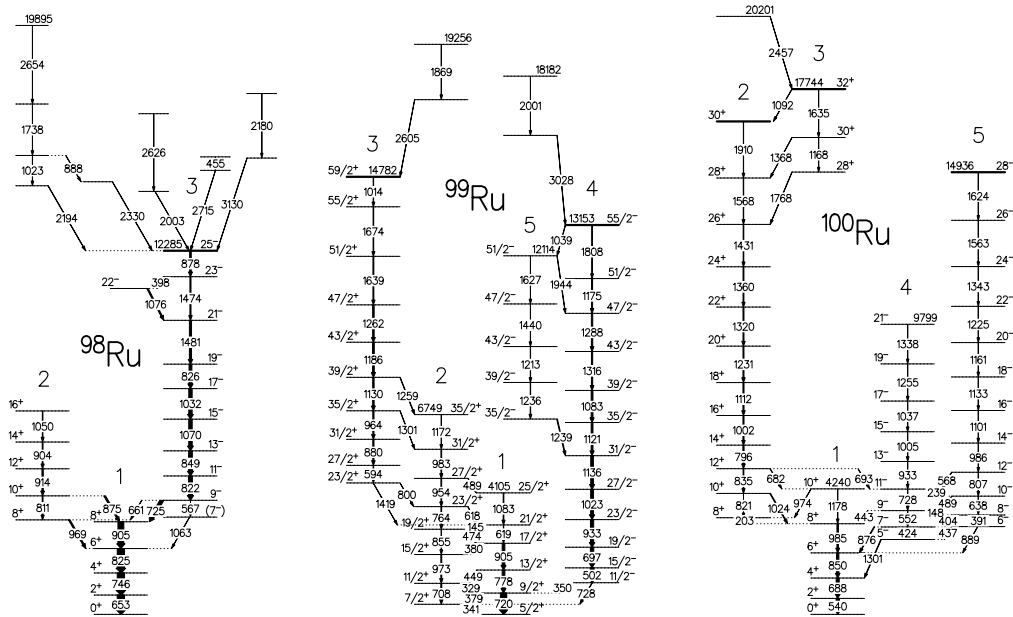


Figure 15. Terminating bands in Ru nuclei. Terminating states are indicated with thick lines.

We have also identified maximally aligned states in ^{99}Ag [108] and in ^{100}Pd [109], which are the analogues of terminating states in case of shell-model type excitations of less deformed nuclei.

We have studied band termination in the $A \approx 125$ mass region in different collaborations using the Euroball and the Gammasphere spectrometers. In this region we observed favored band terminations and terminating states in the ^{121}Xe [110], ^{123}Cs [111] and ^{124}Ba [112] nuclei, while in the $^{127,129,131}\text{La}$ nuclei we found unfavored band termination [113].

All the terminating states that have been found until now belong to normal-deformed rotational bands. It is of a great interest to find out if band termination can occur in superdeformed bands. To answer this question, we have studied the superdeformed bands of $^{131,132}\text{Ce}$ [114] in collaboration with the University of Liverpool using the Euroball spectrometer array. It has been found that the observed energies of the highest-spin states of these bands followed that of being predicted by the configuration-dependent cranked Nilsson-Strutinsky calculations, however the terminating states could not be reached experimentally.

5.5 Evidence for isoscalar spin-aligned neutron-proton coupling in ^{92}Pd

Our group has been contributing to the study of another exotic phenomena arising in nuclei along the $N = Z$ line. There are long-standing predictions, that isovector pairing (isospin $T=1$) which is dominant at low excitation energies, in all nuclei up to around mass 80, will change in the heavier $N=Z$ nuclei, and isoscalar ($T=0$) neutron-proton (np) pairing is expected to have major influence when the mass number increases towards the exotic doubly magic nucleus ^{100}Sn .

This is so, as in nuclei with equal neutron and proton numbers ($N=Z$) enhanced correlations are expected between neutrons and protons occupying orbitals with the same quantum numbers, favouring

this isoscalar neutron-proton pairing, in addition to the normal isovector pairing.

To study the excited states of these nuclei, one has to overcome the problem of extremely low reaction cross-section and the huge background caused by open charged-particle channels. We carried out a high-statistics experiment at GANIL, using the state-of-the-art detector system, the joint assembly of EXOGAM, DIAMANT and the NeutronWall, in order to identify excited states in the $N = Z = 46$ nucleus ^{92}Pd . The use of DIAMANT as veto device enabled the rejection of the gammas from the charged particle channels, while the NeutronWall was used to select gammas from the relevant neutron-evaporation channel. The careful analysis of the data resulted in the identification of four excited states in the nucleus ^{92}Pd by assigning new gamma-transitions to it.

The comparison of the experimental data with Shell Model predictions shows that the anticipated new type of $T=0$ isoscalar neutron-proton pairing exists in ^{92}Pd , and plays an important role in forming the properties of the excited states [115]. For more details see also the *Highlights* section of this Annual Report.

To further prove the existence of this new type of (np)-pairing, a new experiment is to be done soon at GANIL in the next even-even $N=Z$ nucleus, on the way to the doubly magic ^{100}Sn .

6 Structure of light neutron rich nuclei

Study of nuclei far from stability has a long tradition in ATOMKI. It was already started by Tibor Fényes in the '70-s in Dubna, where his group investigated the β -decay of heavy nuclei produced by spallation. A renewal of the topic took place in the late '80-s as part of the ball spectroscopy initiated in ATOMKI by Barna Nyakó. Construction of radioactive beam facilities opened a new opportunity in the field allowing to reach nuclei up to the drip lines. The fruitful scientific relation to RIKEN served as a basis for the collaboration with Japanese scientists, while the high reputation of the researchers of ATOMKI at the EUROBALL established the French connection. Thus, a RIKEN - Rikkyo - CNS - TITech - ATOMKI collaboration was formed to perform mainly γ -ray spectroscopic research using a hydrogen target at the Japanese radioactive beam facility under the supervision of RIKEN chief scientist, Tohru Motobayashi. Similarly, an Orsay - GANIL - Bucharest - Dubna - Debrecen cooperation was organized by Prof. Faical Azaiez aimed at in-beam γ -ray spectroscopy of fragmentation reactions at the French National Laboratory, GANIL. In these collaborations we studied a series of neutron rich nuclei shown in Fig.16.

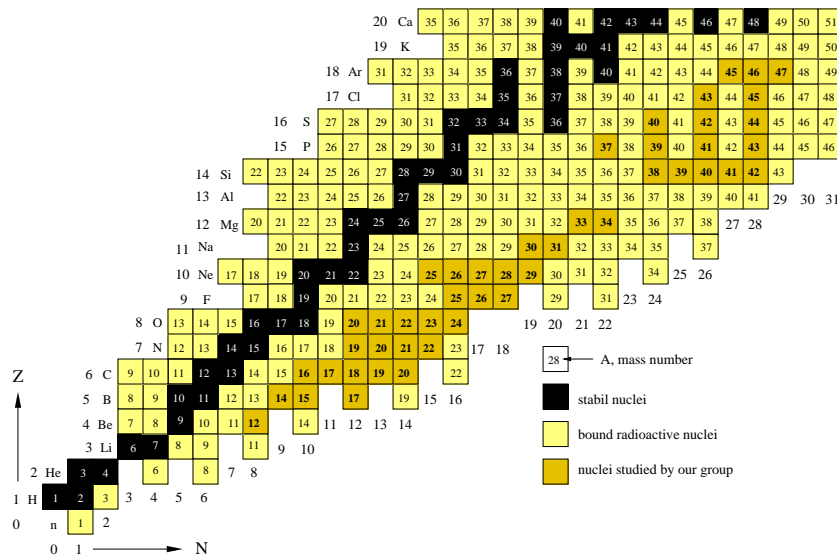


Figure 16. Light neutron-rich nuclei studied by our group

In the present review, we report on the results obtained at GANIL on the $N = 14, 16$ (sub)shell closures and on the disappearance of the signs of the $N = 28$ shell closure in neutron rich nuclei, as well as on the outcomes achieved in RIKEN on the disappearance of the $N = 20$ shell closure approaching the Oxygen isotopic chain and the decoupling of the weakly bound neutrons in heavy C and B nuclei.

6.1 The $N = 14, 16$ subshell closures in neutron rich O and C nuclei

From the study of the excited states in $^{20-24}\text{O}$ through their gamma decay, an estimate of the size of the $N = 14$ and $N = 16$ neutron gaps could be made. In both cases the gaps are found to be large, and both ^{22}O and ^{24}O are doubly magic nuclei. The presence of the rather well bound doubly-magic nucleus ^{24}O on the neutron drip line is a very unique situation. These results as well all other properties observed for $^{20,21,22,23,24}\text{O}$ are in excellent agreement with predictions made nearly 20 years ago with the USD effective Hamiltonian. It appears that while the $N = 16$ shell gap turns out to be larger than 3 MeV in the heaviest Oxygen isotopes, it is only of the order of 1 MeV in the Silicon and Magnesium isotopes. This can be accounted for by considering the role of the strong proton-neutron monopole interaction acting between the two spin-orbit partners $\pi d_{5/2}$ and $\nu d_{3/2}$. As the $d_{5/2}$ proton orbital is emptied this interaction is released and the $d_{3/2}$ neutron orbital is shifted towards the fp shell making at the same time the decrease of the $N = 20$ shell gap and the increase of the $N = 16$ gap. This evolution of neutron $d_{3/2}$ is complete in the Oxygen isotopes where the $\pi d_{5/2}$ is empty making the $N = 16$ shell relatively larger. This large $N = 16$ gap in O nuclei is most probably the reason why heavier isotopes with $N = 18$ and 20 are neutron unbound as the $\nu d_{3/2}$ lies at higher energy than in Mg and Si nuclei [124].

The spectroscopy of C isotopes up to ^{20}C has been carried out for the first time. From the systematics of the 2_1^+ energies, we found that the $N = 14$ subshell gap is no longer present in the C isotopic chain. This sudden breakdown is ascribed to the early crossing of the $s_{1/2}$ and $d_{5/2}$ levels at $N = 9$ due to reduced proton-neutron tensor forces and to the reduced neutron-neutron interaction when going from O to C nuclei [125].

6.2 Disappearance of the $N = 20$ shell gap

We have studied the ^{28}Ne nucleus by $(p,p\gamma)$ inelastic scattering in inverse kinematics. Using the recently measured $B(E2; 0_1^+ \rightarrow 2_1^+)$ value, the neutron transition matrix element M_n was determined. While the transition probabilities can be interpreted by both the calculations within the sd and $sdpf$ shell models shows that some of the neutrons are pushed across the $N = 20$ shell. Although, the observed small neutron transition probability in ^{28}Ne can be explained in the pure sd and the Monte Carlo shell model, the detection of two low-lying excited states in ^{27}Ne together with the anomalies previously observed in the energies of the excited states along the $N = 18$ line, namely the appearance of excited states around 1.5 MeV in ^{29}Na , the low energy of the 2^+ state in ^{28}Ne and the presence of a low-energy state in ^{27}F can be considered as a clear and consistent set of data indicating a quickly decreasing $N = 20$ shell gap [126].

We have searched for bound excited states in ^{27}F by use of the (p,p') process in inverse kinematics. We observed two γ -ray lines in all the $^{25,26,27}\text{F}$ isotopes. The existence of the first excited states in $^{25,26}\text{F}$ can be explained by the traditional shell model. A bound excited state in ^{27}F and the second excited state in ^{26}F can only be interpreted by breaking up the $N = 20$ shell. The presence of an additional bound state in ^{27}F cannot be explained by the available theories. This fact suggests that some additional effects are not considered in the models, *e.g.*, a faster decrease of the single particle energies of the intruder states due to drip line effects [127].

We have applied the method of the invariant mass spectroscopy in combination with the (d,p) reaction which enabled us to study of single particle properties of nuclei next to the neutron drip

line. We investigated the excited states of ^{23}O observing two unbound nuclear states at 4.0 MeV and 5.3 MeV energies. From a comparison with shell model calculations, the first one is the neutron $d_{3/2}$ state, the energy of which gives the $N = 16$ shell closure to be 4 MeV. This is large enough to explain why ^{24}O is the last bound oxygen isotope. The second excited state observed in the present experiment does not have any counterpart in the sd model space, and corresponds to a state from the fp shell. Its energy relative to the $d_{3/2}$ state determines the strength of the $N = 20$ shell closure to be 1.3 MeV and provides a direct evidence for the disappearance of the $N = 20$ shell closure at $Z = 8$ [128].

6.3 Disappearing signs of the $N = 28$ shell closure approaching ^{42}Si

In-beam γ -spectroscopy with fragmentation reactions at intermediate energies made possible the extension of the level schemes in neutron-rich sulfur isotopes to higher-lying excited states. Collective model and shell model calculations are in very good agreement with the experimental level schemes. It is found that ^{40}S and ^{42}S are deformed, γ -soft nuclei, while ^{44}S exhibits a shape mixing in the low-energy states, which suggests the erosion of the $N = 28$ spherical closed-shell. The microscopic model calculations performed show that although the $N = 28$ shell gap has decreased with decreasing Z , it has not disappeared at $Z = 16$. On the other hand, according to the shell model, the $Z = 16$ subshell effect present at $N = 20$ is completely lost when adding neutrons up to $N = 28$. As a result of the near-degeneracy between the $\pi s_{1/2}$ and $\pi d_{3/2}$ orbitals, the quadrupole field of the pseudo- $SU(3)$ configuration could polarize the neutron core to such an extent that a permanent quadrupole deformation evolved at $N = 24 - 28$ [129].

The neutron single-particle energies $p_{3/2}$, $p_{1/2}$, and $f_{5/2}$ have been determined in ^{47}Ar and compared to those in the ^{49}Ca isotone. A reduction of the $N = 28$ shell gap by 330(90) keV was found if two protons are removed, confirming that the $N = 28$ shell gap only slightly decreases with decreasing proton number [130].

The level scheme of ^{46}Ar has been extended to higher excitation energy and higher spin by a new technique based on in-beam γ -ray spectroscopy and fragmentation reactions at intermediate energy. A level scheme of ^{45}Ar was suggested for the first time. These results provided a missing link between the $N = 27, 28$ Ca and S nuclei and facilitate a systematic study of changes of their structure. The sudden lowering of the energy of the first $3/2^-$ state in ^{45}Ar gives further evidence to the suggestion that this $3/2^-$ state becomes the ground state in ^{43}S in agreement with the shell model prediction. The evolution of the ground state deformation in the $N = 28$ isotones could be related to the position of the 0_2^+ states in the even-even nuclei. In ^{46}Ar , the suggested 0_2^+ state at 2710 keV is expected to have a $2p2h$ configuration [131].

According to theoretical models and experimental findings, the size of the $N = 28$ shell gap seems to be reduced south of ^{48}Ca . This may give rise to a new island of inversion at low- Z , $N = 28$ nuclei. Whether this is the case depends on the correlation energy, too. Its magnitude would be reduced if a strong $Z = 14$ sub-shell closure exists. The structure of neutron-rich ^{14}Si isotopes around $N = 28$ was decided to be explored in order to clarify the situation about the $N = 28$ reduction and the emergence of a new island of inversion.

We observed the $2_1^+ \rightarrow 0_1^+$ transition in ^{42}Si from in-beam γ -ray spectroscopy at GANIL. The very low γ -ray energy - 770 ± 15 keV - is a strong evidence for a disappearance of the $N = 28$ shell closure in this isotope. The energy of the 2^+ state in ^{42}Si is well reproduced by both shell model and mean field approaches which predict a strong oblate deformation ($\beta_2 \sim -0.4$) [132].

Excited states in ^{39}Si and ^{41}Si have been identified for the first time from γ -ray spectroscopy of fragmentation of a cocktail beam of radioactive isotopes. A comparison of the level structure of $^{39,41}\text{Si}$ with that of the $^{45,47}\text{Ca}$ isotones, as well as with the results of large-scale shell-model calculations, was used to infer the lowering of the intruder states in $^{39,41}\text{Si}$. A low-lying intruder state in ^{39}Si and a deformed ^{41}Si ground state are proposed. Based on the shell-model calculations, it is suggested

that the border of the $N = 28$ island of inversion falls between $N = 25$ and 27 in the Si isotopes, confirming that ^{42}Si lies in a region of deformation. It was shown that to account for the low-lying level structure of $^{39,41}\text{Si}$, both neutron *and* proton excitations across the $N = 28$ and $Z = 14$ shell closures are required [133].

6.4 Decoupling of weakly bound neutrons from the core in $^{16,20}\text{C}$ and ^{17}B

We have extracted the charge to mass deformation ratio in ^{16}C by use of the Coulomb–nuclear interference method. As a result, a low $B(E2)$ value of 0.28 W.u. has been deduced and the high $M_n/M_p=7.6 \pm 1.7$ ratio caused by the small charge transition matrix element. These results show that the 2_1^+ state in ^{16}C practically consists of pure valence neutron excitations. The polarization of the closed ^{14}C core by the valence nucleons is extremely weak, which suggests that the two valence neutrons are basically decoupled from the core. This unusual nature may provide a new aspect of decoupling of neutron and proton distributions in unstable nuclei [134].

We have measured the cross section of the $^1\text{H}(^{20}\text{C}, ^{20}\text{C}'\gamma)$ and $^{208}\text{Pb}(^{20}\text{C}, ^{20}\text{C}'\gamma)$ processes and deduced the neutron and charge transition probabilities at $M_n^2=292\pm 52$ (stat) fm^4 and $B(E2) < 18.4$ (stat) e^2fm^4 . The transition strengths have also been calculated in the *psd* shell model, and it was found that a suppression factor of ~ 0.4 of both the proton and neutron polarization charges is needed to interpret the experimental results in Carbon isotopes heavier than ^{14}C [135].

We have measured the excitation cross section of the $^{17}\text{B}(p,p')$ reaction. From a comparison with the previously determined electric quadrupole moment, we deduced the deformation parameter of the neutron and proton distributions to be $\beta_n \sim 0.6$ and $\beta_p = 0.36$. Exploiting the information on deformations in the ground state of ^{17}B an upper limit on the neutron effective charge of $e_n < 0.12$ has been deduced. This value is 4 times smaller than the one characteristic for nuclei close to stability in this mass region. The decoupling phenomenon was shown in $^{16,20}\text{C}$, now we proved its existences in ^{17}B , too, and there are suggestions - from a comparison with shell model calculations - that it takes place also in ^{15}B . Although, these nuclei are in a close group, it seems that this kind of neutron decoupling is a more general feature, and may be a typical characteristics of nuclei with an extended neutron distribution [136].

A possible reason for these decreased polarization charges might be the extended valence neutron distribution. In weakly bound nuclei, a neutron skin may develop, the thickness of which is expected to be roughly proportional to the difference of the proton and neutron separation energies, suggesting that the neutron distribution in the less-bound C isotopes is wider in agreement with the measurement of nuclear radii. Assigning the increase of the nuclear size relative to a ^{14}C core to the valence neutrons using the prescription of Hansen and Jonson, the radius of the valence neutron distribution of Carbon isotopes becomes much larger than that of their core, and larger than that of the Oxygen isotopes, too. This implies that for C nuclei, the valence neutrons spend more time outside of the core resulting in a weaker polarization.

Qualitatively, the polarization charges are inversely proportional to the radial matrix element of the orbit involved in the transition. Comparing the reduction factors calculated with harmonic oscillator and Skyrme wave functions (that takes the relatively loose binding of the Carbon isotopes into account), a ratio of ≈ 0.6 can be derived, which shows that the effects of weak binding qualitatively give the major part of of the reduction. However, to fully understand this phenomenon, more detailed microscopic calculations giving a reliable radial distribution for weakly bound nuclei are necessary.

7 Nuclear structure data evaluation

Besides carrying out original research, we have also joined to the nuclear structure and decay data compilation and evaluation work being done by experts in data centers belonging to the international

network of Nuclear Structure and Decay Data evaluators (NSDD). This activity is coordinated by the International Atomic Energy Agency with the main responsibility lying with the United States Nuclear Data Program (USNDP) and National Nuclear Data Center, Brookhaven National Laboratory. Atomki became one of the NSDD data centers in 2011.

Reliable nuclear structure and decay data are of a vital importance for the fundamental nuclear physics and astrophysics research and also for the different applied nuclear fields. NSDD evaluators perform two main types of evaluation: the so called mass-chain evaluation where all the nuclear structure and decay data of nuclei belonging to a certain mass number are compiled and evaluated, and the different horizontal evaluations where one type of nuclear data are compiled and evaluated for the all the nuclei. Results of mass-chain evaluations are stored in standard format in the Evaluated Nuclear Structure Data File (ENSDF) which is maintained by the US National Nuclear Data Center at Brookhaven National Laboratory, and which is available for the nuclear physics community through the internet. The ENSDF data file is a basis of several internet-based applications (Isotope Explorer, NuDat) and regular publications (Nuclear Data Sheets, Nuclear Wallet Cards) which are popular among the users.

We take part in the mass-chain evaluation and we are responsible for the $A=101-105$ mass chains. In the past few years we have been working on temporary mass chains. We have evaluated the $A=50$ [137], 129, and 128 mass chains and a part of the $A=84$ mass chain [138]. In the future we plan to continue this work by evaluating approximately one mass chain per year.

References

- [1] Fényes T. et al., *Fizika* **22** (1990) 273.
- [2] Árvay Z. et al., *Nucl. Instr. Meth.* **178** (1980) 85.
- [3] Demin A. G. et al., *Nucl. Phys. A* **106** (1968) 337.
- [4] Fényes T. et al., *Proc. Int. Conf. On the properties of nuclei far from the region of beta-stability*, Leysin, Switzerland, 1970, CERN 70-30.
- [5] Fényes T. et al., *Nucl. Phys. A* **247** (1975) 103.
- [6] Fényes T. et al., *Acta Phys. Hung.* **71** (1992) 239.
- [7] Fényes T. et al., *Particles and Nuclei (Dubna)* **26** (1995) 831.
- [8] Krasznahorkay A. et al., *Nucl. Phys. A* 473 (1987) 471.
- [9] Kibédi T. et al., *Phys. Rev. C* **37** (1988) 2391.
- [10] Krasznahorkay A. et al., *Nucl. Phys. A* **499** (1989) 453.
- [11] Gácsi Z. et al., *Phys. Rev. C* **44** (1991) 642 .
- [12] Gulyás J. et al., *Phys. Rev. C* **46** (1992) 1218.
- [13] Timár J. et al., *Nucl. Phys. A* **552** (1993) 149.
- [14] Algora A. et al *Nucl. Phys. A* **588** (1995) 399.
- [15] Sohler D. et al., *Nucl. Phys. A* **604** (1996) 25.
- [16] Podolyák Zs., Fényes T., Tdžmár J., *Nucl. Phys. A* **584** (1995) 60.
- [17] Fényes T.: Basic properties of the atomic nucleus, in *Handbook of Nuclear Chemistry*, eds. A. Vértes et al. 2nd ed., vol. I, p. 39, 2011. Springer Verlag.
- [18] Fényes T.: *Structure of atomic nuclei (Akad. Kiadó, Budapest)* 2002.
- [19] Fényes T. et al.: *Atommagfizika I (Debreceni Egyetemi Kiadó, Debrecen)* 2009.
- [20] Fényes T.: *Atommagfizika II, Részecskék és kölcsönhatásaik (Kossuth Egyetemi Kiadó, Debrecen)* 2007.
- [21] Krasznahorkay A. et al., *Acta Physica Polonica B* **27** (1996) 139.
- [22] Csatlós M. et al., *Acta Physica Polonica B* **28** (1997) 37.
- [23] Krasznahorkay A. et al., *Acta Physica Hungarica New Series - Heavy Ion Physics* **7** (1998) 35.
- [24] Krasznahorkay A. et al., *Physical Review Letters* 80 (1998) 2073.
- [25] Krasznahorkay A.: Tunneling through triple-humped fission barriers. *Handbook of Nuclear Chemistry*. 2nd edition. Eds: Vértesi A., Nagy S., Klencsár Z., Lovas R.G., Rösch F., Hamburg, Springer Verlag **1** (2011) 281.
- [26] Csatlós M. et al., *Physics Letters B* **615** (2005) 175.
- [27] Hunyadi M. et al., *Acta Physica Polonica B* **32** (2001) 699.
- [28] Hunyadi M. et al., *Physics Letters B* **505** (2001) 27.
- [29] Hunyadi M. et al., *Acta Physica Polonica B* **30** (1999) 1263.
- [30] Krasznahorkay A. et al., *Acta Physica Polonica B* 30 (1999) 1467.

- [31] Krasznahorkay A. et al., Physics Letters B **461** (1999) 15.
- [32] Gassmann D. et al., Physics Letters B **497** (2001) 181.
- [33] Krasznahorkay A. et al., Acta Physica Polonica B **32** (2001) 657.
- [34] Csige L. et al., Physical Review C **80** (2009)1:R1301(5)
- [35] Algora A. et al., Physical Review Letters **105** (2010) 202501.
- [36] Kamanin D. V. et al., Pis'ma v Fizika Elementarnykh Chastits i Atomnogo Yadra **7** (2010)2(158):209.
- [37] Csige L. et al., Journal of Physics: Conference Series **212** (2011) 2022.
- [38] Krasznahorkay A. et al., Physical Review Letters **66** (1991) 1287.
- [39] Krasznahorkay A. et al., Nuclear Instruments and Methods in Physics Research A **316** (1992) 306.
- [40] Ponomarev V. Yu., Krasznahorkay A., Nuclear Physics A **550** (1992) 150.
- [41] Krasznahorkay A. et al., Nuclear Physics A **567** (1994) 521.
- [42] Csatlós M. et al., Nuclear Instruments and Methods in Physics Research A **421** (1999) 272.
- [43] Csatlós M. et al., Nuclear Physics A **719** (2003) 304c.
- [44] Krasznahorkay A. et al., Nuclear Physics A **731** (2004)224.
- [45] Krasznahorkay A. et al., Physical Review C Nuclear Physics **64** (2001)7302.
- [46] Hunyadi M. et al., Physics Letters B **576** (2003)253.
- [47] Hunyadi M. et al., Nuclear Physics A **731** (2004) 49.
- [48] Hunyadi M. et al., Physical Review C **75** (2007) 014606(12).
- [49] Krasznahorkay A. et al., Physical Review Letters **82** (1999) 3216.
- [50] Stuhl L. et al., Acta Physica Polonica B **42** (2011) 667.
- [51] Krasznahorkay A., Spin-isospin giant resonances: Review and future perspectives. Acta Physica Polonica B **36** (2005) 1095.
- [52] Furnstahl R. J., Nucl. Phys. A **706** (2002) 85.
- [53] Horowitz C. J. and Piekarewicz J., Phys. Rev. Lett. **86** (2001) 5647 .
- [54] Langer C. et al., Nuclear Instruments and Methods in Physics Research A **659** (2011) 411.
- [55] Ciemala M. et al., Nucl. Instr. Meth. Phys. Res. A **608** (2009) 76.
- [56] Krasznahorkay A. et al., submitted to Phys. Rev. Lett.
- [57] Nyakó B. M. et al., Phys. Rev. Lett. **52** (1984) 507.
- [58] Twin P.J. et al., Phys. Rev. Lett. **57** (1986) 811.
- [59] Nyakó B. M. et al., Phys. Rev. Lett. **56** (1986) 2680.
- [60] Singh B., Zywna R. and Firestone R. B., Nuclear Data Sheets **97** (2002) 241.
- [61] Simpson J., Z. Phys. A **358** (1997) 139.
- [62] Simpson J. et al., Acta Physica Hungarica New Series - Heavy Ion Physics **11** (2000) 159.
- [63] Akkoyun S. et al., Nuclear Instruments and Methods in Physics Research A **668** (2012) 26.
- [64] Scheurer J. N. et al., Nuclear Instruments and Methods in Physics Research A **385** (1997) 501.
- [65] Gál J. et al., Nuclear Instruments and Methods in Physics Research A **366** (1995) 120.
- [66] Gál J. et al., Nuclear Instruments and Methods in Physics Research A **516** (2004) 502.
- [67] Korten W. and Lunardi S. (Eds.) on behalf of the EUROBALL Coordination Committee
Achievements with the EUROBALL spectrometer; Scientific and Technical Activity Report 1997–2003
<http://euroball.inl.infn.it> <http://npg.dl.ac.uk/euroball-home/> <http://eballwww.in2p3.fr/EB/>
 Printed in Padova, Italy, Poligrafica Antenore, March 2004
- [68] Santos D. et al., Physical Review Letters **74** (1995) 1708.
- [69] Semple A. T. et al., Physical Review C **54** (1996) 425
- [70] Paul E. S. et al., Physical Review C **71** (2005) 054309.
- [71] Bentley M. A. et al., J. Phys. G: Nucl. Part. Phys. **17** (1991) 481.
- [72] Bentley M. A. et al., J. Phys. G: Nucl. Part. Phys. **21** (1995) L21.
- [73] Curien D. et al., Physical Review Letters **71** (1993) 2559.
- [74] Theisen Ch. et al., Physical Review C **54** (1996) 2910.
- [75] Lagergren K. et al., Physical Review Letters **87** (2001) 022502.
- [76] Hackman G. et al., Physical Review C **52** (1995) 2293.
- [77] Crowell B. et al., Physical Review C **51** (1995) 1599.
- [78] Wilson A. N. et al., Physical Review C **54** (1996) 559.
- [79] Amro H. et al., Physics Letters **B413** (1997) 15.
- [80] Korichi A. et al., Physical Review Letters **86** (2001) 132746.
- [81] Wilson A. N. et al., Physical Review Letters **104** (2010) 162501.
- [82] Dudek J. et al., **211** (1988) 252
- [83] Galindo-Uribari A. et al., Phys. Rev. Lett. **71**(1993) 231.
- [84] Pomorski K., Dudek J., Phys. Rev. C **67** (2003) 044316
- [85] Rizzi V. et al., Eur. Phys. J. A **7** (2000) 299.
- [86] Herskind B. et al., AIP Conference Proceedings **701** (2004) 303.
- [87] Nyakó B. M. et al., Acta Physica Polonica B **36** (2005) 1033
- [88] Herskind B. et al., Physica Scripta T **125** (2006) 108

- [89] Herskind B. et al., Acta Physica Polonica B **38** (2007) 1421.
- [90] Timár J. et al., Phys. Lett. B **598** (2004) 178.
- [91] Joshi P. et al., Phys. Lett. B **595** (2004) 135.
- [92] Timár J. et al., Phys. Rev. C **73** (2006) 011301(R).
- [93] Sohler D. et al., et al., Phys. Rev. C **71** (2005) 064302.
- [94] Sohler D. Zs. Dombrádi, et al., Submitted to Phys. Rev. C
- [95] Timár J. et al., Phys. Rev. C **76** (2007) 024307.
- [96] Suzuki T. et al., Phys. Rev. C **78** (2008) 031302(R).
- [97] Timár J. et al., Phys. Rev. C **84** (2011) 044302.
- [98] Timár J. et al., Eur. Phys. J. A **16** (2003) 1.
- [99] Kuti I. et al., Submitted to Phys. Rev. C
- [100] Wang S. Y. et al., Phys. Lett. **B703** (2011) 40.
- [101] Suzuki T. et al., Submitted to Phys. Rev. C
- [102] Gizon J. et al., Phys. Lett. B **410** (1997) 95.
- [103] Sohler D. et al., Nucl. Phys. A **733** (2004) 37.
- [104] Nyakó B.M. et al., Phys. Rev. C **60** (1999) 024307.
- [105] Timár J. et al., Eur. Phys. J. A **4** (1999) 11.
- [106] Gizon J. et al., Phys. Rev. C **59** (1999) R570.
- [107] Timár J. et al., Phys. Rev. C **62** (2000) 044317.
- [108] Sohler D. et al., Eur. Phys. J. A **16** (2003) 171.
- [109] Perez G.E. et al., Nucl. Phys. A **686** (2001) 41.
- [110] Timár J. et al., J. Phys. G **21** (1995) 783.
- [111] Singh A. K. et al., Phys. Rev. C **70** (2004) 034315.
- [112] Al-Khatib A. et al., Phys. Rev. C **74** (2006) 014305.
- [113] Wadsworth R. et al., Phys. Rev. C **62** (2000) 034315.
- [114] Paul E. S. et al., Phys. Rev. C **71** (2005) 054309.
- [115] Cederwall B. et al., Nature **469** (2011) 68.
- [116] Paul E. S. et al., Nucl. Phys. A **727** (2003) 207.
- [117] Wilson A. N. et al., Physics Letters **B505** (2001) 6.
- [118] Mason P. et al., Physical Review C **72** (2005) 064315.
- [119] Timár J. et al., Nuclear Physics A **696** (2001) 241.
- [120] Timár J. et al., European Physical Journal A **7** (2000) 7.
- [121] Ntshangase S. S. et al., Physical Review C **82** (2010) 041305.
- [122] Petri M. et al., Nuclear Instruments and Methods in Physics Research Section A **607** (2009) 412.
- [123] Sharpey-Schafer J. F. et al., European Physical Journal A **47** (2011) 6.
- [124] Stanoiu M. et al., Phys. Rev. C **69** (2004) 034312.
- [125] Stanoiu M. et al., Phys. Rev. C **78** (2008) 034315.
- [126] Dombrádi Zs. et al., Phys. Rev. Lett. **96** (2006) 182501.
- [127] Elekes Z. et al., Phys. Lett. B **599** (2004) 17-22.
- [128] Elekes Z. et al., Phys. Rev. Lett. **98** (2007) 102502.
- [129] Sohler D. Phys. Rev. C **66**, 054302 (2002).
- [130] Gaudefroy L. et al., Phys. Rev. Lett. **97** (2006) 092501.
- [131] Dombrádi Zs. et al., Nucl. Phys. A **727** (2003) 195.
- [132] Bastin B. et al., Phys. Rev. Lett. **99** (2007) 022503.
- [133] Sohler D. et al., Phys. Lett. B **703** (2011) 417.
- [134] Elekes Z. et al., Phys. Lett. B **586**(2004) 34.
- [135] Elekes Z. et al., Phys. Rev. C **79** (2009) 011302(R).
- [136] Dombrádi Zs. et al., Phys. Lett. B **621** (2005) 81.
- [137] Elekes Z., Timár J., Singh B., Nuclear Data Sheets **112** (2011) 1.
- [138] Abriola D. et al., Nuclear Data Sheets **110** (2009) 2815

1.1 Systematic survey of a four-parameter subclass of Natanzon potentials

G. Lévai

Exact solutions of the one-dimensional Schrödinger equation

$$\frac{d^2\psi}{dx^2} + (E - V(x))\psi(x) = 0$$

are generally searched for in the form $\psi(x) = f(x)F(z)$, where $F(z)$ is some special function of mathematical physics that satisfies a second-order differential equation

$$\frac{d^2F}{dz^2} + Q(z)\frac{dF}{dz} + R(z)F(z) = 0 .$$

A rather general potential family solvable in this sense is the six-parameter Natanzon class, in which case $F(z)$ is the (confluent) hypergeometric function. Three of the six parameters originate directly from F , while the other three are contained in the function $z(x)$ describing the variable transformation. In general both the $z(x)$ function and the E_n bound-state energy eigenvalues are determined in an implicit form. Despite this compact formulation, the derivation of exact solutions of the Schrödinger equation is prohibitively complicated for general Natanzon-class potentials. Closed solutions are thus obtained only for some subclasses, e.g. shape-invariant potentials that contain up to three parameters and include the most well-known textbook examples (harmonic oscillator, Coulomb, Pöschl–Teller, etc. potentials). A handful of further Natanzon-class potentials have been discussed, but no systematic exploration has been done in this field so far.

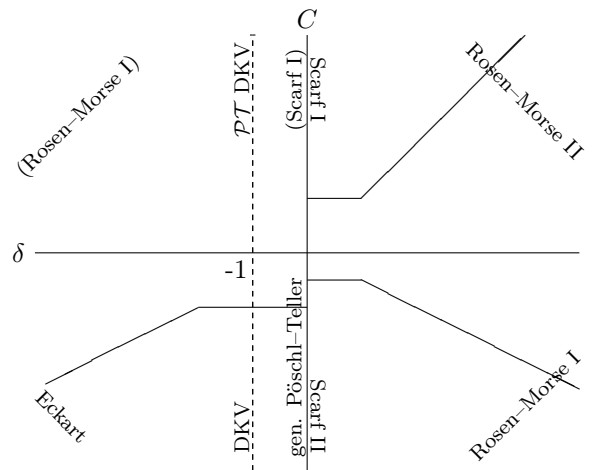
In an effort to fill this gap we considered a subset of the Natanzon class by choosing the Jacobi polynomials as $F(z) = P_n^{(\alpha,\beta)}(z)$ and defining the variable transformation by

$$\frac{(z')^2}{(1-z^2)^2}(\delta + 1 - z^2) = C .$$

This potential family is characterized by 2+2 parameters, i.e. C and δ above and two more setting the coupling parameters of an even and an odd potential component. A notable feature of this potential is that only $x(z)$ can be

determined in closed form, i.e. it is an implicit potential, furthermore, the energy eigenvalues are also determined implicitly and can be obtained by solving a quartic algebraic equation.

This potential contains as special limit all the shape-invariant potentials that are solved by the Jacobi polynomials. To reach these potentials either the $\delta \rightarrow 0$ limit has to be taken, or the $\delta \rightarrow \pm\infty$ limit with the condition $C/\delta = \tilde{C} = const.$ Pairs of these shape-invariant potentials can be transformed into each other continuously, as illustrated on the figure below by randomly chosen broken lines. It is remarkable that the axes are impenetrable, so the parameter space is divided into disjoint regions. Besides the shape-invariant limits, this potential also contains two previously known Natanzon-class potentials: the symmetric Ginocchio potential is obtained if the coupling coefficient of the odd potential term is set to zero, and the Dutt-Khare-Varshni (DKV) potential that is obtained for $\delta = -1$.



The rather flexible spectral structure of this potential might be especially useful when its \mathcal{PT} -symmetric version will be constructed, as it introduces new mechanisms of the spontaneous breaking of \mathcal{PT} symmetry. It is interesting that the \mathcal{PT} -symmetric version of the DKV potential is already included in the present scheme for $C > 0$ and $\delta = -1$.

[1] G. Lévai, in preparation.

2.1 Bosonization and functional renormalization group approach in the framework of QED₂

I. Nándori

In particle physics, theories and models are defined at high energies, where symmetry considerations are valid, but the measurements are performed at relatively low energies. One has to determine the low-energy behavior of every model which requires renormalization. In usual cases the perturbative renormalization is sufficient however, there are special situations like for example the confinement of quarks into hadrons where non-perturbative treatments are needed.

Since the invention of exact renormalization group (RG) method its main goal has been to describe systems where the usual approximations (e.g. perturbation theory) are failed. Unfortunately, exact RG equations are functional equations hence one has to use truncations in order to handle them. The truncated RG equations depend on the choice of the, so called regulator function, i.e. on the RG scheme implying that the predicting power of the RG method is weakened and a dependence of physical results on the choice of the regulator function can be observed. Since the functional RG has been developed in order to be able to perform renormalization non-perturbatively, it is of great importance to clarify how far the results obtained are independent or at least weakly dependent on the particular choice of the RG scheme. Consequently, optimization is required.

In order to optimize the scheme-dependence of RG equations a commonly accepted strategy is to consider such models, where other non-perturbative results are available. For example, lattice calculations can provide us physical properties (e.g. fixed points, critical exponents) of certain models which can be considered as exact values and the RG scheme should be chosen to get the closest value to the exact one. Then the RG equation optimized in this way can be applied to

other models and theories. However, it is an open question whether the RG approach optimized for a particular model can produce the best result for the others, or more generally, if the RG equation is optimized for scalar type models (which is the usual case) then it is rather questionable whether it remains optimized for the more complicated (but more physical) fermionic and gauge theories.

The method proposed in [1] based on bosonization opens a new platform to consider the RG scheme-dependence. In low dimensions, exact bosonization rules do exist which enables us to reformulate the gauge and fermionic models in terms of elementary scalar fields. The advantage of this new approach is the usage of bosonization because both the bosonized and the original models can be treated simultaneously by RG methods. Consequently, it is possible to perform optimization for the scalar theory and for its fermionic or gauge counterpart as well. On the one hand, optimizations of the bosonic and fermionic models can be related to each other via bosonization providing us a tool to consider the validity of the conventional optimization. On the other hand, it has impact on bosonization.

As an example, we investigated the two-dimensional Quantum Electrodynamics (QED₂) with massive fermions which exhibits confinement. Since the phase structure of the QED₂ has already been mapped out by the density matrix RG approach, it was used in [1] in order to optimize the scheme-dependence for its bosonized version. The drawback of the RG study on the bosonization transformations was also discussed, namely it was indicated that renormalization of QED₂ requires interaction terms corresponding to higher frequency modes of its bosonized version.

[1] I. Nándori, Phys. Rev. D **84**, 065024 (2011).

3.1 On high precision astrophysical factor measurement for the ${}^3\text{He}+{}^4\text{He}$ reaction

C. Bordeanu^{a)}, Z. Elekes, J. Farkas, Zs. Fülöp, G. Gyürky, Z. Halász, G.G. Kiss, E. Somorjai, T. Szücs

In order to construct a gas cell target and perform experiments for E_{CM} from 1.2 to 3.0 MeV on the ${}^3\text{He}({}^4\text{He},\gamma){}^7\text{Be}$ reaction we continued our feasibility tests for the contaminants at the ATOMKI cyclotron at $E_\alpha=8.0$ MeV. The decision was to use Cu OFHC as a stopper. $1\ \mu\text{m}$ thick nickel windows from LeBow for the gas cell were checked for their surface cleanliness and the sealing capability. A special system was manufactured and most of the foils were tested for pressure difference of over 300 mbar in long measurements. No pinholes or loss through the glue were detected. The thickness and the uniformity along the Ni foils surface were measured using the ORTEC Soloist system. A moveable 2 mm diameter collimator was put between a ${}^{241}\text{Am}$ source and the foil at different positions of the foil. From α -spectra taken by a particle detector it was found that the nominal thicknesses agree with SRIM calculations within 4% and their uniformity all over the surface changes less than 5%. One foil was checked at the cyclotron with ${}^4\text{He}^{++}$ beam at $E_\alpha=6.3$ MeV with maximum beam intensity of 520 nA. No any damage of the window was detected. For the activation part, the HPGe efficiency was measured using standard gamma sources ${}^{133}\text{Ba}$, ${}^{152}\text{Eu}$, ${}^{22}\text{Na}$, ${}^{60}\text{Co}$ and ${}^{137}\text{Cs}$ at 27 cm. An extended (diameter of 5 mm) ${}^7\text{Be}$ test source was prepared at the Van de Graaff accelerator through ${}^7\text{Li}(p,n){}^7\text{Be}$ reaction at $E_p=2.3$ MeV. This source, placed at 1 cm from the detector, was moved in steps of 5 mm parallel to the detector surface with up to 15 mm from the center. The position change affects the detection counting by less than 1%, also confirmed by GEANT4.

Three measurements for the ${}^3\text{He}+{}^4\text{He}$ reaction at $E_\alpha=4.0$ MeV, 5.4 MeV and 6.32 MeV were performed at the cyclotron. The beam impinged on the ${}^3\text{He}$ (99.99%) gas target, at

around 300 mbar pressure, collecting each time about 20 mC. The current and pressure were monitored during the irradiations. The stopper was cooled using water. LN_2 in the cooling trap was used to minimize the Carbon build-up. After the irradiation, Cu OFHC stopper was put in front of the 100% HPGe detector at 1 cm distance and the activity was measured for about 7 days (see Figure 1.). The activity was determined using a home made fitting program and GEANT4. The results agreed within the error.

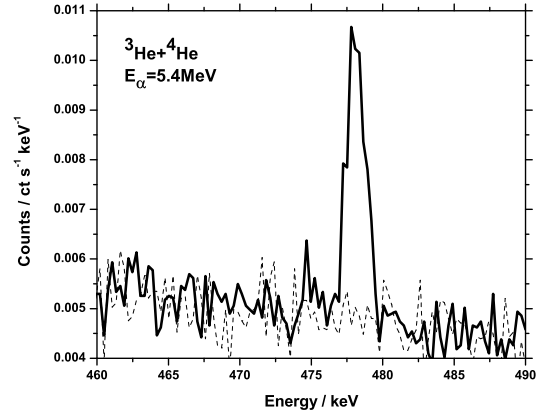


Figure 1. The spectrum of the irradiated target (full line) and the background spectrum (dashed). The peak at 478 keV is from ${}^7\text{Be}$.

The work was presented at the Nordic Conference for Nuclear Physics in Stockholm 2011 [1].

Acknowledgements

This project is financially supported by OTKA and NKTH through the HUMAN-MB-08-B mobility project NKTH-OTKA-EU FP7 (Marie Curie).

a) on leave from NIPNE-HH, Magurele, Romania

[1] C. Bordeanu *Phys.Scr.* T145 (2011) in press

3.2 Cross section measurements of astrophysically important proton capture reactions on Nitrogen isotopes

Gy. Gyürky, Z. Elekes, Zs. Fülöp, E. Somorjai for the LUNA collaboration

Proton capture reactions on both stable Nitrogen isotopes play an important role in Hydrogen burning processes of different stellar environments. The $^{14}\text{N}(p,\gamma)^{15}\text{O}$ reaction is the key reaction of the CNO cycle of Hydrogen burning since its cross section determines the rate of the cycle. On the other hand, the competition of the $^{15}\text{N}(p,\gamma)^{16}\text{O}$ reaction with the $^{15}\text{N}(p,\alpha)^{12}\text{C}$ process determines the branching between the first and second CNO cycles, the second cycle being responsible e.g. for the O depletion observed in some globular cluster giant stars. These two capture reactions have been studied recently by the LUNA collaboration [1].

The experiments have been carried out at the LUNA-II 400 kV accelerator located in the LNGS underground laboratory [2] whose low background provides unique conditions for low cross section measurements.

The $^{14}\text{N}(p,\gamma)^{15}\text{O}$ cross section has been measured at three proton energies of 359, 380, and 399 keV. These energies have been chosen because the R-matrix fits used to extrapolate the cross sections to low, astrophysical energies can be sensitively tested at these energies. Owing to the decay scheme of the ^{15}O reaction product, the cross section measurement is highly influenced by the true coincidence summing effect of the emitted γ -rays. In order to reduce this effect, the segmented Clover HPGe detector of ATOMKI equipped with a BGO anti-Compton shield has been used and the sys-

tematic uncertainty has been therefore drastically reduced.

The obtained cross sections have been compared with R-matrix fits. The precise data helped resolve the discrepancy between the previous, conflicting extrapolations for ground-state capture and a new zero energy extrapolated S-factor value of $S_{\text{GS}}(0) = 0.20 \pm 0.05$ keV b is recommended. New branching ratios for the decay of the 259 keV resonance have also been determined with improved precision [3].

The $^{15}\text{N}(p,\gamma)^{16}\text{O}$ reaction has been studied for the first time in a wide energy range between 70 and 370 keV which is directly relevant to some Hydrogen burning environments like novae or massive AGB stars. The cross section has been measured by using solid state TiN targets enriched in ^{15}N and a 4π BGO summing crystal.

With the present data we have been able to confirm the result of a previous R-matrix extrapolation. In particular, in the temperature range of astrophysical interest the new rate is about a factor of 2 smaller than reported in the widely adopted compilation of reaction rates and the uncertainty is now reduced down to the 10 % level [4].

[1] <http://luna.lngs.infn.it>

[2] <http://www.lngs.infn.it>

[3] M. Marta *et al.*, Phys. Rev. C **83**, (2011) 045804.

[4] A. Cacioli *et al.*, Astronomy and Astrophysics **533**, (2011) A66.

3.3 The ^{106}Cd family problem

A. Ornelas^{a)}, D. Galaviz^{a)}, Zs. Fülöp, G. Gyürky, G. G. Kiss, Z. Máté, E. Somorjai, P. Mohr^{b)}, T. Rauscher^{c)}, K. Sonnabend^{d)}, A. Zilges^{e)}

The 35 stable nuclei located on the proton rich side of the valley of stability whose production cannot be explained in the framework of the slow and rapid neutron capture process are called the *p-nuclei*. These are thought to be produced by photodisintegration reactions on the neutron rich stable isotopes under high temperatures ($T_9 \approx 2-3$, billion Kelvin) and short time intervals to avoid complete photodisintegration to the nickel and iron isotopes. A possible site for these reactions are the C,N,O layers of a Type II Supernovae [1]. A full understanding of the explosion mechanisms of Type II Supernovae is required to more precisely determine where the necessary conditions for the process can be found. The ^{106}Cd isotope is an important piece of the puzzle and the study of the ^{106}Cd alpha-nuclear potential is a necessary requirement to better describe the full reaction network.

The aim of this work is to extend the knowledge of the alpha nucleus potentials for *p-nuclei* at energies close to the astrophysically relevant window for the photodisintegration reaction (γ, α). The elastic scattering of α particles has been observed at different energies above and below the Coulomb barrier of the *p-nucleus* ^{106}Cd at the ATOMKI cyclotron laboratory [2]. The main problem in the study of ^{106}Cd α -nucleus potential is the ‘‘Family Problem’’ which implies there are several different potentials that describe the experimental data

with similar precision. The problem was presented in previous articles [3,4] and was treated with more detail in [5].

The current results from the Family Problem can be seen in Fig. 1. The families obtained provide a better description of the capture data than the McFadden global α -nuclear potential. Further analysis of the families will allow for the determination of the most suited family to describe the experimental data. The ^{106}Cd family problem is currently being treated in a full length article, soon to be published, where the obtained families are compared with further global α -nucleus potentials and χ^2/F table will also be presented to further strengthen the results.

- a) Centro de Física Nuclear da Universidade de Lisboa, Av Prof. Gama Pinto 2, 1649-003 Lisboa, Portugal
- b) Strahlentherapie, Diakoniekrankehaus Schwäbisch Hall, D-74523 Schwäbisch Hall, Germany
- c) Departement für Physik und Astronomie, Universität Basel, Klingelbergstrasse 82, CH-4056 Basel, Switzerland
- d) Institut für Angewandte Physik, Goethe-University Frankfurt, D-60438 Frankfurt, Germany
- e) Institut für Kernphysik, Universität zu Köln, Zülpicher Straße 77, D-50937 Köln, Germany

- [1] M. Arnould and S. Goriely, Phys. Rep. 384, 1 (2003)
- [2] G. Gyürky, et al., Phys. Rev. C 74, 025805 (2006)
- [3] P. Mohr, et al., Phys. Rev. C 55, 1523 (1997)
- [4] Zs. Fülöp, et al., Phys. Rev. C 64, 065805 (2001)
- [5] A. Ornelas, et al., PoS (NIC XI), 241 (2010)
- [6] L. McFadden, et al., Nucl. Phys. 84, 177 (1966)

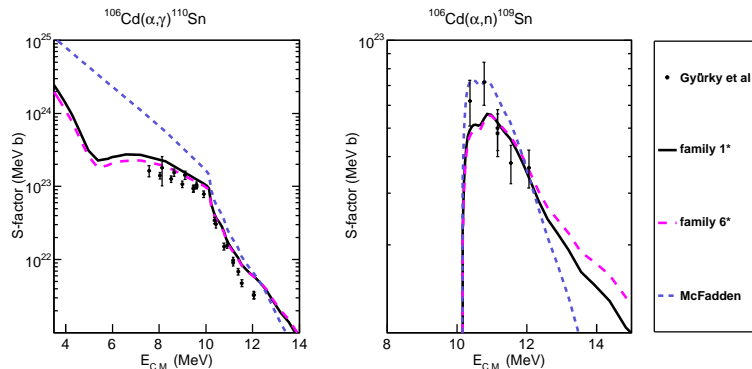


Figure 1. α -nucleus potential best families comparing to the McFadden potential [6].

3.4 Cross section measurements of the $^{121}\text{Sb}(\alpha, \gamma)^{125}\text{I}$ reaction at astrophysical energies

Z. Korkulu^{a)}, G. G. Kiss, T. Szücs, Zs. Fülöp, Gy. Gyürky, E. Somorjai, Z. Halász, N. Özkan^{a)}, R. T. Güray^{a)}, C. Yalcin^{a)}

The nucleosynthesis of elements beyond iron is dominated by neutron captures in the so-called *s*- and *r*-processes. However, there are 35 proton-rich isotopes — the so-called *p* nuclei — which cannot be formed in this way because they are shielded from the *s* process flow and from *r*-process β -decay chains. These nuclei are thought to be produced in the so-called γ -process, where sequences of photodisintegrations on preexisting *r*- and *s*-seed nuclei are taking place.

A γ -process simulation requires a large nuclear reaction network, involving about 1800 isotopes and more than ten thousand reaction rates. Since the largest fraction of such a network contains proton-rich, unstable isotopes, which are not accessible for cross section measurements with present experimental techniques, almost all of these rates have to be determined using the statistical Hauser-Feshbach (HF) formalism [1]. Recently, the measurement of alpha-induced reaction cross sections on ^{121}Sb isotope has been started in order to provide a test for the Hauser-Feshbach predictions and to optimize the input parameters of the aforementioned theoretical model.

The cross section of the $^{121}\text{Sb}(\alpha, \gamma)^{125}\text{I}$ and $^{121}\text{Sb}(\alpha, n)^{124}\text{I}$ reactions are under study, using the activation method. The targets were produced by vacuum evaporation of natural and highly enriched 99.59 % ^{121}Sb onto thin, high purity aluminum foils. The target thicknesses were measured by weighing. As a first step the maximum tolerable beam currents were determined and the alpha-induced cross sections at 13 MeV and 14 MeV were measured.

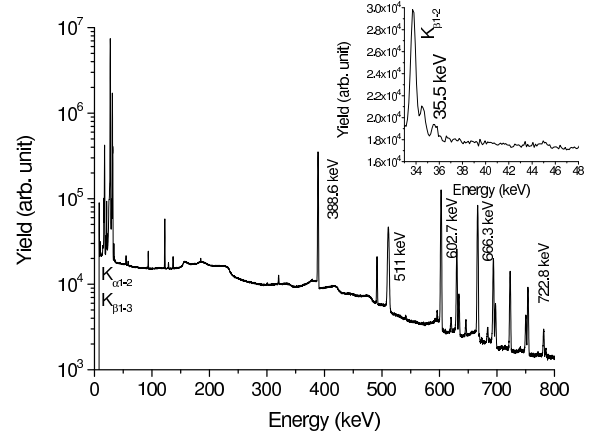


Figure 1. γ spectrum taken using the LEPS detector after the irradiation of a natural Sb target with $E_\alpha = 14$ MeV alpha-beam. The investigated transitions are indicated.

The γ -activity of the irradiated samples has been measured first with a 100 % relative efficiency HPGe detector in ULB (Ultra Low Background) shielding to determine the $^{121}\text{Sb}(\alpha, n)^{124}\text{I}$ reaction cross section by measuring the yield of 602.73 keV, 722.78 keV and 1690.96 keV γ -lines. To measure the $^{121}\text{Sb}(\alpha, \gamma)^{125}\text{I}$ reaction cross section, the yield of the 35.49 keV γ -line was counted in close geometry using a Low Energy Photon Spectrometer (LEPS).

The $^{121}\text{Sb}(\alpha, \gamma)^{125}\text{I}$ and $^{121}\text{Sb}(\alpha, n)^{124}\text{I}$ reactions are planned to be studied at energies close to the astrophysically relevant energy region, between 10 MeV - 16 MeV, covered by 0.5-1 MeV steps.

a) Department of Physics, University of Kocaeli, Umuttepe 41380, Kocaeli, Turkey

[1] W. Rapp, Phys. Rev. C **78**, 025804 (2008)

3.5 In-beam γ -spectroscopic study of rotational bands in ^{132}La

I. Kuti, J. Timár, D. Sohler, E. S. Paul^{a)}, K. Starosta^{b)}, A. Astier^{c)}, D. Bazacco^{d)}, P. Bednarczyk^{e)}, A. J. Boston^{a)}, N. Buform^{c)}, H. C. Chantler^{a)}, C. J. Chiara^{f)}, R. M. Clark^{g)}, M. Cromaz^{g)}, M. Descovich^{a)}, Zs. Dombrádi, P. Fallon^{g)}, D. B. Fossan^{h)}, C. Fox^{a)}, A. Gizonⁱ⁾, J. Gizonⁱ⁾, A. A. Hecht^{j)}, N. Kintz^{e)}, T. Koike^{k)}, I. Y. Lee^{g)}, S. Lunardi^{d)}, A. O. Macchiavelli^{g)}, P. J. Nolan^{a)}, B. M. Nyakó, C. M. Petrache^{d,l)}, J. A. Sampson^{a)}, H. C. Scraggs^{a)}, R. Wadsworth^{m)}, A. Walker^{a)}, L. Zolnai

Rotational bands in odd-odd $A \approx 130$ nuclei have attracted a great interest since it was suggested that the near degeneracy of two bands in ^{134}Pr could be caused by chiral symmetry breaking. The first two nuclei where such chiral-candidate doublet band structure was observed, were the ^{134}Pr and the ^{132}La . However, the chiral interpretation has recently been questioned by lifetime experiments in both nuclei.

In ^{132}La three strongly linked band structures are known involving the yrast $\pi h_{11/2}\nu h_{11/2}$ band, the band previously assigned as its chiral partner band, and a third band. The spins and parities of the levels in the third band could not be deduced unambiguously, thus the quasiparticle configuration of this band were not known. It has been tentatively suggested that this band also has $\pi h_{11/2}\nu h_{11/2}$ configuration, and the three bands have been described recently with the SPAC model [1] as magnetic rotational bands with different planar symmetries and remarkable contribution of collectivity. Our main aim was to determine the configuration of the third band of ^{132}La and decide if it can be $\pi h_{11/2}\nu h_{11/2}$ as it has been assumed. In order to determine the quasiparticle configuration of the rotational bands in ^{132}La , we have studied the medium- and high-spin structure of this nucleus based on two heavy-ion fusion-evaporation reaction experiments measured by the EUROBALL and GAMMASPHERE detector arrays. New excited states has been found in five of the formerly known six bands. Unambiguous multipolarity assignment was made for $\sim 35\%$ of the observed transitions using DCO and linear polarisation analysis and determination of conversion coefficients. The derived multipolarities enabled us to determine

unambiguous spins and parities of most excited states of ^{132}La . On the basis of the exhaustive analysis of the experimental data, it has been found that the negative-parity band structure of the studied nucleus is similar to that of the ^{134}Pr . This feature could also be used to assist in the determination of the band configurations in ^{132}La .

Negative-parity has been derived for the studied third band from the present experiment which contradicts with the previous $\pi h_{11/2}\nu h_{11/2}$ configuration assumption. In addition, the observed alignment of this band is $\sim 6 \hbar$ larger than that of the yrast band, which shows that it has a four-quasiparticle configuration. On the basis of its experimental properties we assigned $\pi g_{7/2}(h_{11/2})^2\nu h_{11/2}$ configuration to this band. Taking similar considerations into account the other medium-spin negative parity bands might be built on $\pi d_{5/2}\nu h_{11/2}$, $\pi g_{7/2}\nu h_{11/2}$ or $\pi h_{11/2}\nu g_{7/2}$ structures.

[1] A.A. Pasternak *et al.*, Acta Phys. Pol. B40(2009)647

- a) OLL, University of Liverpool, Liverpool, UK
- b) NSCL/Cyclotron Laboratory, MSU, East Lansing, MI, USA
- c) Institut de Physique Nucléaire de Lyon, IN2P3-CNRS, Villeurbanne, France
- d) Dipartimento di Fisica and INFN Sezione di Padova, Padova, Italy
- e) IReS, Strasbourg, France
- f) Washington University, St. Louis, MO, USA
- g) LBNL, Berkeley, CA, USA
- h) SUNY, Stony Brook, NY, USA
- i) ISN, IN2P3-CNRS, Grenoble, France
- j) Wright Nuclear Structure Laboratory, Yale University, New Haven, CT, USA
- k) Graduate School of Science, Tohoku University, Sendai, Japan
- l) Università di Camerino, Camerino, Italy
- m) University of York, Heslington, United Kingdom

3.6 High precision determination of the half-life of $^{133\text{m}}\text{Ce}$ for nuclear astrophysical application

J. Farkas, Gy. Gyürky, Z. Halász, T. Szücs, Zs. Fülöp and E. Somorjai

Supernova simulations aim to explain the nucleosynthesis of heavy elements. These simulations rely heavily on nuclear physics input. This input comes either directly from nuclear measurements or from theoretical calculations, where the theories are constrained by the results of nuclear experiments.

In order to support the theoretical work on the astrophysical γ process, we planned to measure the cross section of α induced reactions on ^{130}Ba , as experimental data on these reactions are absent in the literature. The (α, γ) reaction cross section can directly be used to enhance γ process models, while the (α, n) reaction is used to constrain the Hauser – Feshbach model calculations used in such models.

We used the activation technique in our measurement: we activated the ^{130}Ba target with an α beam and detected the γ photons emitted by the decaying reaction products. In order to perform the cross section measurement one needs the precise half-lives of the created nuclei. We discovered that the half-life of one of the products of the $^{130}\text{Ba} + \alpha$ reaction, $^{133\text{m}}\text{Ce}$ is known with high uncertainty ($t_{1/2}^{\text{lit}} = 4.9 \text{ h} \pm 0.4 \text{ h}$ [1]). We also found evidence that this half-life value is underestimated. As the compilations are based on a single measurement published back in 1967 [2], we decided to perform a recent half-life measurement of $^{133\text{m}}\text{Ce}$ the precision of which is suitable for our needs.

The irradiations were performed at the cy-

clotron of Atomki and the decay of $^{133\text{m}}\text{Ce}$ was followed with a γ detector. By analysing the 58.4 keV, 130.8 keV and 477.2 keV peaks we found the half-life to be $t_{1/2} = 5.326 \text{ h} \pm 0.011 \text{ h}$ [3]. As this value is consistent with the literature value and its uncertainty is lower by a factor of 30, we have suggested its use in the nuclear data compilations to-come. This new half-life value was successfully used in the cross section measurement of the $^{130}\text{Ba}(\alpha, n)^{133\text{m}}\text{Ce}$ reaction [4].

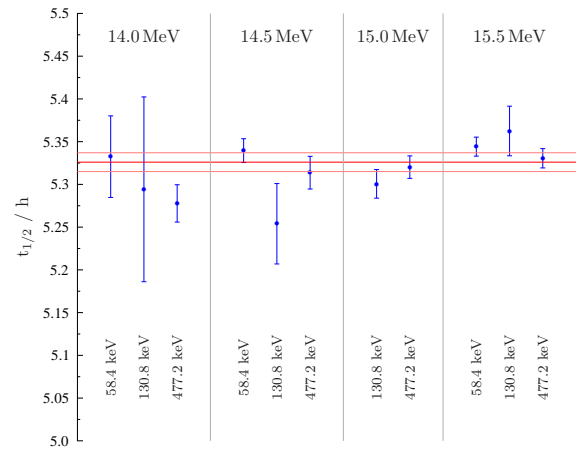


Figure 1. The half-lives obtained from the analysis of the different peaks of $^{133\text{m}}\text{Ce}$. The horizontal lines show the final result and its uncertainty.

- [1] S. Rab, Nuclear Data Sheets **75**, 491 (1995)
- [2] C. Gerschel, G. Albouy, Compt. Rend. **264B**, 183 (1967)
- [3] J. Farkas *et al.*, Eur. Phys. J. A **47**:7 (2011)
- [4] Z. Halász *et al.*, Phys. Rev. C **85**, 025804 (2012).

3.7 Medium- and high-spin band structure of the chiral-candidate nucleus ^{134}Pr

J. Timár, K. Starosta^{a)}, I. Kuti, D. Sohler, D. B. Fossan^{b)}, T. Koike^{c)}, E. S. Paul^{d)}, A. J. Boston^{d)}, H. C. Chantler^{d)}, M. Descovich^{d)}, R. M. Clark^{e)}, M. Cromaz^{e)}, P. Fallon^{e)}, I. Y. Lee^{e)}, A. O. Macchiavelli^{e)}, C. J. Chiara^{f)}, R. Wadsworth^{g)}, A. A. Hecht^{h)}, D. Almededⁱ⁾, S. Frauendorfⁱ⁾

Medium- and high-spin structure of the ^{134}Pr nucleus has been studied using the $^{116}\text{Cd}(^{23}\text{Na},5n)$ reaction in order to search for new rotational bands and obtain a more complete picture of the structure and special features of this nucleus. The level scheme of ^{134}Pr has been extended. Nine new rotational bands have been found, among which one positive-parity band might be the chiral-partner candidate of the rare $\pi h_{11/2}\nu h_{11/2}$ band, while five of them are the expected two-quasiparticle negative-parity bands. The relative placement of the two previously known isomeric states has been established, and thus the ground state of the nucleus has been unambiguously determined. The tentatively assigned spin and parity values of the previously known states have been unambiguously determined.

Experimental Routhians and aligned angular momenta, as well as $B(\text{M}1)/B(\text{E}2)$ ratios have been derived from the data and compared

with predictions of Total Routhian Surface calculations, and results of the geometrical model of Dönau and Frauendorf, respectively. On the basis of these comparisons, and on the basis of comparison with neighboring nuclei, tentative configurations have been assigned to the new bands.

- a) Department of Chemistry, Simon Fraser University, Burnaby, Canada
- b) State University of New York, Stony Brook, USA
- c) Graduate School of Science, Tohoku University, Sendai, 980-8578, Japan
- d) Oliver Lodge Laboratory, University of Liverpool, Liverpool, United Kingdom
- e) Nuclear Science Division, LBNL, Berkeley, California 94720, USA
- f) Physics Division, Argonne National Laboratory, Argonne, Illinois 60439, USA
- g) University of York, Heslington, United Kingdom
- h) Wright Nuclear Structure Laboratory, Yale University, New Haven, USA
- i) Physics Department, University of Notre Dame, Notre Dame, Indiana 46556, USA

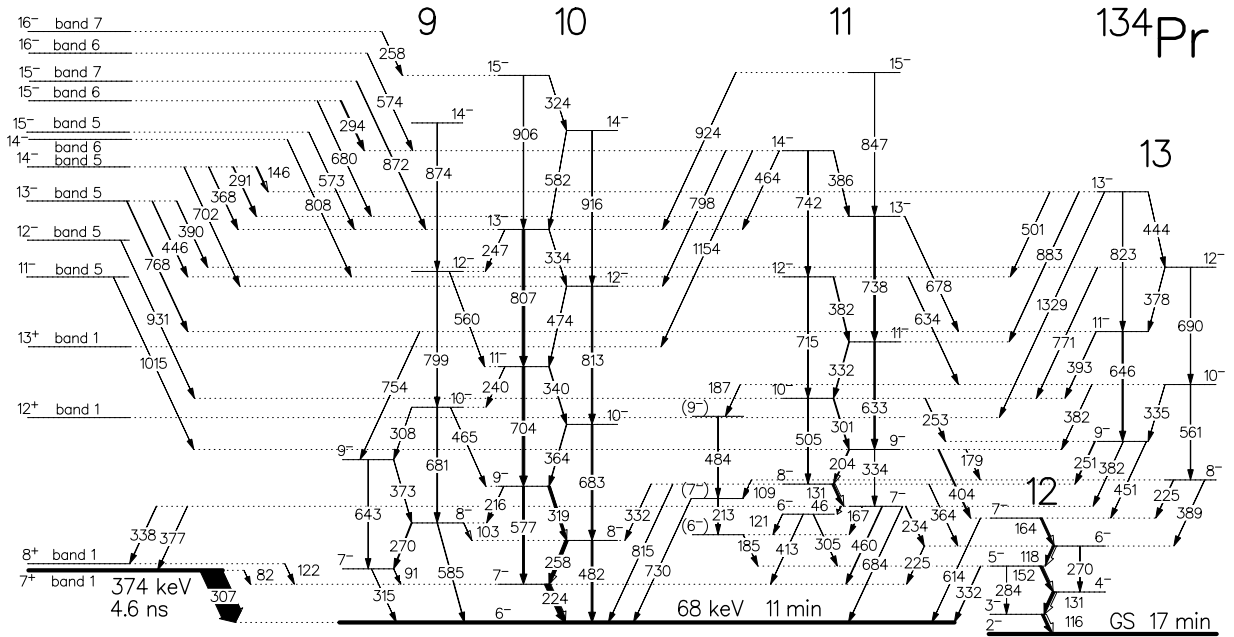


Figure 1. Low- and medium-spin negative-parity bands of ^{134}Pr .

3.8 Total reaction cross sections from $^{141}\text{Pr}(\alpha,\alpha)^{141}\text{Pr}$ elastic scattering and α -induced reaction cross sections at low energies

P. Mohr^{a)}

Very recently, new experimental data for the $^{141}\text{Pr}(\alpha,n)^{144}\text{Pm}$ cross section have been presented by Sauerwein *et al.* [1]. It has been shown in [1] that the experimental data cannot be reproduced using the statistical model and the global α -nucleus potentials of McFadden and Satchler [2], Avrigeanu *et al.* [3], and Fröhlich/Rauscher [4]. However, a good fit to the data could be achieved using a modification of the McFadden/Satchler potential with an additional energy dependence of the imaginary part (labelled “Sauerwein/Rauscher” in Fig. 1).

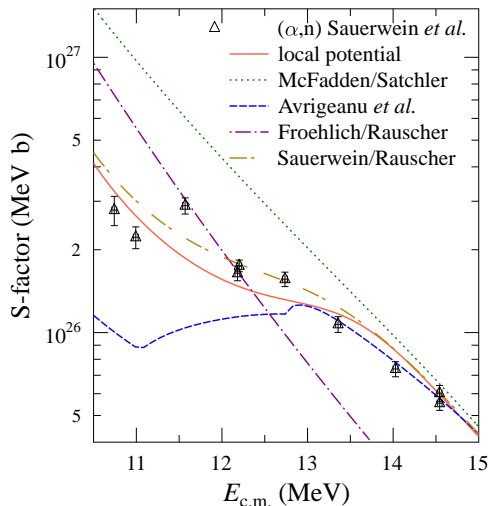


Figure 1. Total reaction cross section (converted to S-factor) for $\alpha + ^{141}\text{Pr}$, compared to experimental $^{141}\text{Pr}(\alpha,n)^{144}\text{Pm}$ data [1]. Further discussion see text.

The aim of the present work [5] is a consistent description of $^{141}\text{Pr}(\alpha,\alpha)^{141}\text{Pr}$ elastic scattering and α -induced reaction cross sections on ^{141}Pr . In a first step the available experimental scattering data [6,7] have been analyzed, and a local potential could be derived. The real part was calculated from the folding procedure, and the imaginary part was taken in the Woods-Saxon parametrization. The energy dependence of the real part turns out to

be negligible at low energies. Contrary, the strength of the imaginary part shows a strong energy dependence which is parametrized using a Fermi-type function. The geometry of the imaginary potential is well constrained from the analysis of the scattering data. From this energy-dependent potential the total reaction cross section σ_{reac} can be calculated in the energy range of the recent experiment [1] without further adjustments.

Because of the dominating neutron decay channel of the compound nucleus ^{145}Pm in the energy range of [1], the cross section of the $^{141}\text{Pr}(\alpha,n)^{144}\text{Pm}$ reaction is almost identical to the total reaction cross section σ_{reac} . The prediction of σ_{reac} from the new local potential agrees well with the experimental $^{141}\text{Pr}(\alpha,n)^{144}\text{Pm}$ data [1] and is independent of other ingredients of the statistical model (see Fig. 1).

In summary, a local potential has been derived from elastic scattering angular distributions. Contrary to various global α -nucleus potentials [2,3,4], this new potential is able to predict the $^{141}\text{Pr}(\alpha,n)^{144}\text{Pm}$ cross section [1] without any further adjustment to experimental reaction data.

Acknowledgements

This work was supported by OTKA (NN83261).

a) Diakonie-Klinikum, Schwäbisch Hall, Germany

- [1] A. Sauerwein *et al.*, Phys. Rev. C **84**, 045808 (2011).
- [2] L. McFadden and G. R. Satchler, Nucl. Phys. **84**, 177 (1966).
- [3] M. Avrigeanu and V. Avrigeanu, Phys. Rev. C **82**, 014606 (2010).
- [4] T. Rauscher, Nucl. Phys. **A719c**, 73 (2003).
- [5] P. Mohr, Phys. Rev. C **84**, 055803 (2011).
- [6] H. W. Baer *et al.*, Phys. Rev. C **3**, 1398 (1971).
- [7] P. Guazzoni and L. Zetta, *priv. comm.* (1994).

3.9 Phase transitions in algebraic cluster models

H. Yépez-Martínez^{a)}, P. R. Fraser^{b)}, P. O. Hess^{b)}, G. Lévai

There has been much interest recently in phase transitions in various nuclear systems. The phases are defined as (local) minima of the potential energy surface (PES) defined in terms of parameters characterizing the nuclear system. Phase transitions occur when some relevant parameter is changed gradually and the system moves from one phase to another one. In the analysis of such systems the key questions are the number of phases and the order of phase transition between them.

Algebraic nuclear structure models are especially interesting from the phase transition point of view, because the different phases may be characterized by different symmetries of the system. Much work has been done recently on models based on the interacting boson approximation (IBA). In these studies the potential energy surface is constructed from the algebraic Hamiltonian by its geometric mapping using the coherent state formalism.

Inspired by these studies we performed a similar analysis of a family of algebraic cluster models based on the semimicroscopic algebraic cluster model (SACM). This model has two dynamical symmetries: the SU(3) and SO(4) limits are believed to correspond to vibration around a spherical equilibrium shape and static dipole deformation, respectively. The semimicroscopic nature of this model is reflected by the fact that a fully antisymmetrized microscopic model space is combined with a phenomenologic Hamiltonian that describes excitations of the (typically) two-cluster system. The microscopic model space is necessary to take into account the Pauli exclusion principle acting between the nucleons of the closely interacting clusters. In practice this means that the number of excitation quanta in the relative motion of the clusters has to exceed a certain number n_0 characterizing the system. This is clearly a novelty with respect to other algebraic models, and it complicates the formalism considerably. We thus introduced as a special limit the *phenomenologic algebraic cluster model* (PACM), in which the $n_0 = 0$ choice was

made. With this choice we ignore a fundamental principle, but in exchange the formalism becomes similar to that of other algebraic models. Our aim was also to explore the consequences of this approximation.

In the first step we constructed the PES of the SACM using coherent states. For this we also modified the formalism of the SACM to the present analysis. This included incorporating a third-order term in the Hamiltonian that stabilizes the spectrum for large values of intercluster excitation quanta (π bosons). The parametrization of the Hamiltonian was also changed to allow for a transition between the SU(3) to the SO(4) limits. The results indicated that the effects of the Pauli principle can be simulated in the PACM by incorporating higher-order terms on the Hamiltonian [1].

In the second step we turned to the analysis of phase transitions both in the SACM and the PACM. The potential energy surface typically contained up to two minima, one spherical and one deformed. The analysis identified both first- and second-order phase transitions for the PACM and the SACM, while in the latter case a critical line was also found [2].

The results were illustrated with numerical studies on the $^{16}\text{O}+\alpha$ and $^{20}\text{Ne}+\alpha$ systems, which correspond to two spherical clusters and to one spherical and one deformed cluster, respectively. The SU(3) limit was found to be the most appropriate one in reproducing the data of the cluster systems. Clear phase transitions were identified in the parameter controlling the transition between the SU(3) and SO(4) limits. It was found that the PACM led to energy spectra that are rather different from the observed physical ones.

^{a)} Universidad Autónoma de la Ciudad de México, Mexico City, Mexico

^{b)} UNAM, Mexico City, Mexico

[1] H. Yépez-Martínez, P. R. Fraser, P. O. Hess, G. Lévai, Phys. Rev. C **85** (2012) 014316.

[2] P. R. Fraser, H. Yépez-Martínez, P. O. Hess, G. Lévai, Phys. Rev. C **85** (2012) 014317.

4.1 Ionization of noble gas atoms by H^0 impact

Á. Kövér, L. Sarkadi, P. Herczku, S.T.S. Kovács

The simplest structured light projectile is the positronium (Ps), the bound state of an electron and positron. Recently the total cross section was measured with Ps projectiles for different atoms and molecules at University College London, UK. It was found that the Ps total cross section is unexpectedly close to that of an electron moving at the same velocity, despite Ps being neutral and having twice the mass [1].

H^0 is the simplest heavy projectile that consists of an electron and a proton. Comparing with Ps the difference is only in their masses. In both cases the projectile and/or the target may be ionized. The comparison of the measured cross section data for the two projectiles gives valuable information on the dynamics of the collision process. For H^0 impact only few studies can be found in the literature where total and ionization cross sections were

determined [2].

We developed a recoil ion detector similar to that was used in [3]. The existing scattered ion detector [4] was used to determine the charge state of the scattered projectiles. The cross sections for the different processes (direct ionization σ^{00} , electron loss σ^{01} , electron capture σ^{0-1}) were determined by measuring the coincidence events between the scattered and recoil particles of different charge states.

The measurements were carried out at the 1.5 MV VdG in ATOMKI. For testing and calibrating the measuring system we compared the published ionization data on He target [2] with our measured data. The normalization of our data to the existing one was done at 300 keV impact energy. The results are shown in Fig 1. In the near future we intend to extend our investigation to use other noble gas atoms as target.

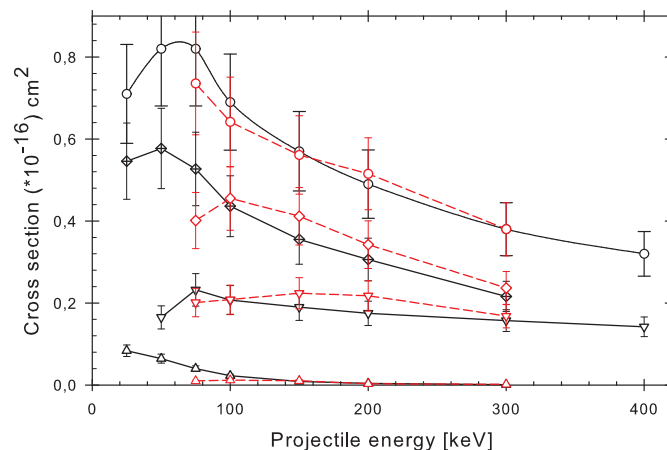


Figure 1. Cross section for ionization occurring in $H^0 - He$ collision. The data connected by the black solid lines are from [2]. The data connected by the red dashed lines are from present measurement. \circ : σ_{-} total ionization; \diamond : σ^{00} direct ionization; ∇ : σ^{01} electron loss; \triangle : σ^{0-1} electron capture.

Acknowledgements

The authors thank for the valuable discussions to G. Laricchia and R. D. DuBois. This work was supported by the National Scientific Research Foundation and the National Office for Research and Technology of Hungary (NKTH-OTKA, Grant No. K67719).

[1] S.J. Brawley *et al*, Science **330** (2010) 789.

[2] R.D. DuBois, Á. Kövér, Phys. Rev. A **59**(1999)1391

[3] Á. Kövér, *et al*, J. Phys. B: At. Mol. Opt. Phys. **26**(1993)L575

[4] A. Báder, *et al*, Meas. Sci. & Techn. **6**(1995)959

4.2 Investigation of MeV proton microbeam transmission between two flat plates – the cases of metallic and insulator plates

K. Tókési, I. Rajta, R.J. Berezky, and Vad

During the last decade there has been a growing interest in the study of charged particle interactions with cylindrical surfaces based on various capillary targets from nano- to macrometer size. In our research these experiments are simplified further, using flat plates instead of a cylindrical shaped target and proton microbeam as projectile.

In this work, we examine only the case in which the axis of the plates was aligned in the same direction as the proton microbeam. We investigate the possible similarities and deviations in the particle transport with metallic and insulator plates. We performed the measurements with 1 and 2 MeV proton microbeams where the beam spot size was $1\ \mu\text{m}$, with a beam current of about 1000 proton/s, and with an extremely small beam divergence [1]. Without the target the beam divergence on the screen was visible. It was found that the focused spot was enlarged to about $130\ \mu\text{m}$. When a sample was inserted into the measurement position and aligned perfectly to the center plane, we did not observe any difference in the image on the screen between this and the sample free case. This was a good test of our measurements and also indicated that the divergent beam really was far from the plates and that the beam passed through without appreciable interaction with the sample. The beam spot thus remained about $130\ \mu\text{m}$ wide both for metallic and insulating samples and for both 1 and 2 MeV energies.

Fig. 1 shows typical proton trajectories. A fraction of particles pass between the two metallic plates without close collision with the inner surface, though are influenced by the image acceleration (see Fig. 1a). The others will suffer close collision with the surface similar to the conventional grazing surface collisions (see Fig. 1b). For the case of insulating plates we

expect the trajectory type, plotted in Fig. 1c.

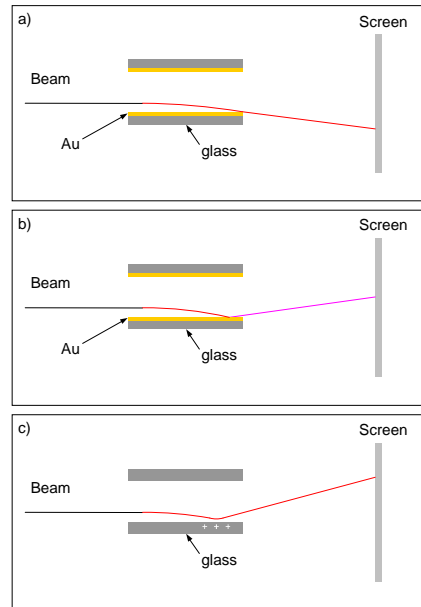


Figure 1. Schematic diagram of our samples with the expected proton trajectory (solid line): a) metallic plates - grazing trajectory, b) metallic plates - specular reflection trajectory, c) insulator plates.

We found a large difference in proton transmission between metallic and insulator plates and also obtained the energy dependent features of the transmission [1]. We observed that the beam deflection is larger for insulator plates than for metallic ones. We have shown that a proton microbeam with lower energy suffers larger deflection for both metallic and insulator plates. Further investigations are in progress to clarify more details of the phenomena.

Acknowledgements

The work was supported in part by the Hungarian Scientific Research Fund OTKA Nos. K67873, K72172, K73703 and by cost action No. MP1002.

[1] K. Tókési, I. Rajta, R.J. Berezky, K. Vad Nucl. Instr. and Meth. Phys. (2011) in press.

4.3 Time-resolved photoemission by attosecond streaking: extraction of time information

S. Nagele^{a)}, R. Pazourek^{a)}, J. Feist^{b)}, K. Doblhoff-Dier^{a)}, C. Lemell^{a)}, K. Tókési and J. Burgdörfer^{a)}

Attosecond streaking is one of the most spectacular applications within the emerging field of attoscience. Streaking is based on a variant of a pump-probe setting with an extreme ultraviolet (XUV) pulse of a few hundred attoseconds serving as a pump and a phase-controlled few-cycle infrared (IR) pulse as a probe. Electrons emitted in the presence of an IR field are accelerated to different final momenta and energies depending on the value of the vector potential at the release time. Thus, time information is mapped onto the energy axis in analogy to conventional streaking.

Attosecond streaking of atomic photoemission holds the promise to provide unprecedented information on the release time of the photoelectron. We have shown that attosecond streaking phase shifts indeed contain timing (or spectral phase) information associated with the Eisenbud - Wigner - Smith (EWS) time delay matrix of quantum scattering [1]. We have identified on the one-electron (or independent particle) level considerable state-dependent time shifts that can be observed in attosecond streaking and which are of quantum mechanical origin [1]. We found a time delay between the hydrogenic 2s and 2p initial states in He^+ exceeding 20 as for a wide range of IR intensities and XUV energies (see Fig. 1).

In addition, we have identified large time shifts which result from the coupling between the IR streaking field and the Coulomb field which depend on the final energy of the free electron and can be accounted for classically. The EWS time shift (or energy variation of the scattering phase) is found to be accessible by streaking only if both initial-state-dependent entrance channel and final-state exit channel distortions are properly accounted for. For such a scenario we have shown that time delays on the single-digit attosecond scale due to short-ranged potentials are in reach.

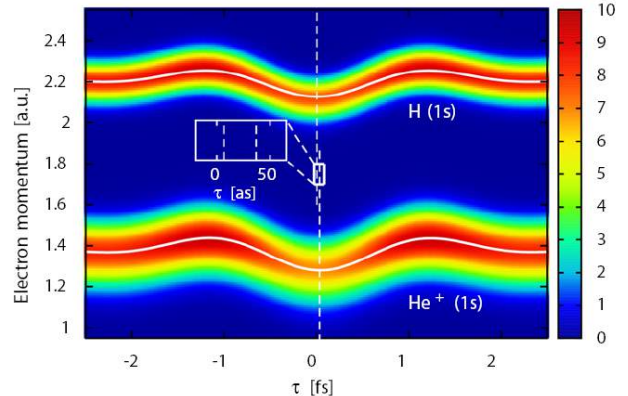


Figure 1. Streaking spectrograms for an 800 nm IR laser field with a duration of 3 fs and an intensity of $10^{12} \text{ W cm}^{-2}$. The graphs show the final momentum distribution in “forward” direction of the laser polarization axis for H(1s) and $\text{He}^+(1s)$ initial states and an XUV photon energy of 80 eV. The solid white lines are the first moments of the electron spectra. The dashed white vertical lines indicate the shift of the central minimum relative to the vector potential. The colour scale is in arbitrary units.

Acknowledgements

This work was supported by the FWF-Austria, grant nos SFB016 and P21141-N16, the TeT under grant no AT-2/2009, the European COST Action CM0702, and in part by the National Science Foundation through TeraGrid resources provided by NICS and TACC under grant TGPHY090031. The computational results presented have also been achieved in part using the Vienna Scientific Cluster (VSC). JF acknowledges support by the NSF through a grant to ITAMP. The authors thank K Schafer for introducing them to the restricted ionization model and acknowledge valuable discussions with U. Thumm and C.H. Zhang.

- a) Institute for Theoretical Physics, Vienna University of Technology, 1040 Vienna, Austria, EU
 - b) ITAMP, Harvard-Smithsonian Center for Astrophysics, Cambridge, MA 02138, USA
- [1] S. Nagele, R. Pazourek, J. Feist, K. Doblhoff-Dier, C. Lemell, K. Tókési and J. Burgdörfer, *J. Phys. B: At. Mol. Opt. Phys.* **44** (2011) 081001.

4.4 K-shell ionization of Cu by positron impact

T. Mukoyama, Y. Nagashima^{a)} and K. Tókési

Ionization by positron impact has been extensively studied both theoretically and experimentally in recent decades. In most cases noble gas atoms were used as the target. For designing new experiments, such as production of antimatter, ionization cross sections for many other atoms are also necessary.

Recently, improvements in experimental techniques have enabled the determination of inner shell ionization cross sections by positron impact [1]. The target was a Cu film deposited on a carbon thin film. Since the total thickness of the target was thin enough to neglect the positron energy loss, the positrons were treated as individual particles interacting with individual Cu atoms.

The classical treatment of various collision problems has been quite successful for the calculation of these ionization cross sections. In particular the classical trajectory Monte Carlo (CTMC) method is widely used. It is a non-perturbative method and hence all the interactions between colliding particles can be taken into account exactly within the framework of the classical dynamics. It has been shown that the CTMC method can be also applied for light projectile impacts.

In this work, Cu K-shell ionization cross sections have been studied theoretically and compared with the experimental results [2]. We also applied the binary encounter approximation (BEA). In both cases we used the frozen charge state model and the Slater-rule for the determination of the static nuclear charge of 1s electron bound to the Cu nucleus. The present calculations were performed solving the non-relativistic equations.

Fig.1 shows the K-shell ionization cross sections of Cu as a function of the positron impact from the threshold energy up to 30 keV. While the CTMC data is close to the experimental data, the BEA data underestimates it. This fact suggests that the Gryzinski-Kowalski

model used in our BEA calculations, is not suitable to calculate K-shell ionization cross sections of incident positrons in the energy region near to the ionization threshold. We hope that the modification of the simple BEA model for positron impact ionization, in order to take into account the Coulomb-deflection effect and to use more realistic electron velocity distributions, will improve our recent results. Work of this kind is in progress and will be published soon.

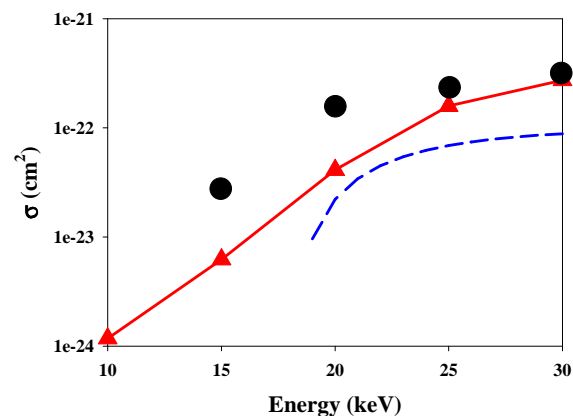


Figure 1. K-shell ionization cross sections of Cu by positron impact. Solid circle: Experimental data from ref. [1], solid line with triangle: present CTMC data, dashed line: binary encounter approach.

Acknowledgements

This work was supported by the Hungarian Scientific Research Fund OTKA No. K72172 and by the Bilateral Japan-Hungary Cooperative Research Program. We would like to express our personal thanks to Andrew Bergman for the critical reading of the manuscript.

a) Department of Physics, Tokyo University of Science, 1-3 Kagurazaka, Shinjuku-ku, Tokyo 162-8601, Japan

[1] Y. Nagashima, F. Saito, Y. Itoh, A. Goto, and T. Hyodo, Phys. Rev. Lett. **92** (2004) 223201.

[2] T. Mukoyama, Y. Nagashima, and K. Tókési, Nucl. Instr. and Meth. B279 (2011) 41

4.5 K-shell ionization of copper by proton and antiproton impact

T. Mukoyama and K. Tókési

In this work K-shell ionization cross sections of copper are studied theoretically. We applied various quantum mechanical approximations (ECPSSR [1] - based on the plane-wave Born approximation using hydrogenic wave functions, corrected for the energy loss of the projectile during the collision (E), for the deceleration and deflection of the projectile in the Coulomb field (C), for the perturbation of the stationary target electron states by the passing projectile (PSS), and for relativistic electron motion (R), PWBA-BC [2] - relativistic plane wave Born approximation including binding, polarization and Coulomb-deflection corrections) and a classical trajectory Monte Carlo (CTMC) method. For the classical case we used the frozen charge state model and we used the Slater-rule for the determination of the static nuclear charge of 1s electron bound to the copper nucleus. The present calculations were performed solving the non-relativistic classical equations. Table. 1 shows our calculated K-shell ionization cross sections

of Cu as a function of the proton and antiproton impact. Our present data are in good agreement with the fitted reference cross sections of Paul and Sacher [3].

Moreover, we found that at the present impact energies the classical and quantum results are very close to each other [4].

Acknowledgements

This work was supported by the Hungarian Scientific Research Fund OTKA No. K72172.

- [1] W. Brandt and G. Lapicki, Phys. Rev. A **23** (1981) 1717, W. Brandt and G. Basbas, Phys. Rev. A **27** (1983) 578.
- [2] M. H. Chen and B. Crasemann, At. Data Nucl. Data Tables **33** (1985) 217.
- [3] H. Paul and J. Sacher, At. Data Nucl. Data Tables **42** (1989) 105.
- [4] T. Mukoyama and K. Tókési, K-shell ionization of copper by proton and antiproton impact, 22nd International Symposium on Ion-Atom Collisions. ISAC 2011. Caen, France, 22nd-25th, June 2011, Book of Abstracts, Eds. L. Adoui, A. Cassimi, F. Front, (2011), p. 44.

Table 1. K-shell ionization cross sections of copper by proton and anti-proton impact.

Energy (keV)	Proton ECPSSR (cm ²)	Proton RPWBA-BC (cm ²)	Proton CTMC (cm ²)	Proton ref.[3] (cm ²)	Antiproton ECPSSR (cm ²)	Antiproton CTMC (cm ²)
900	1.21e-23	1.14e-23	1.44e-23	1.2e-23	2.81e-23	3.06e-23
1000	1.66e-23	1.56e-23	1.66e-23	1.6e-23	3.65e-23	3.69e-23
2000	9.934e-23	9.43e-23	7.37e-23	9.7e-23	1.41e-22	1.36e-22

4.6 Can positrons be guided by insulating capillaries?

R.D. DuBois^{a)} and K. Tőkési

Investigations of guiding of few hundred eV antiparticles by macroscopic insulating capillaries have been described. Using sub-femtoamp positron and electron beams, we demonstrated that a portion of the entering beams were transmitted and emerged in the direction of the capillary. We also demonstrated that the transmitted intensities decreased as the capillary tilt angle was increased (see Fig. 1). Both of these are indications of guiding. However, a comparison with transmitted photon data implies that the positron transmission may result from geometric factors associated with our diffuse beams and tapered capillary used in these studies. For electrons, the comparison indicates differences which could imply that even very low intensity beams can be guided. Measurements of the transmitted intensity as a function of charge entering the capillary were inconclusive as no major increases in the transmitted intensity were observed. 2D static simulations imply that our beam intensities, although extremely small with respect to previous guiding experiments, were capable of supplying sufficient charge for guiding to occur. Although not definitive, our study implies that sub-femtoamp beam intensities are sufficient to form charge patches and produce guiding. This may have been observed for electrons with the question remaining open for positrons. That guiding was not clearly seen may have been due to the capillary geometry used or it may indicate that although sufficient charge is being supplied, the surface and bulk resistivities of glass permit this charge to dissipate faster than it is formed. This aspect was not taken into consideration in our simulations but a crude estimate of the discharge rate implies that beam intensities on the order of pA, rather than fA as

used here, may be required for guiding to occur in the capillaries used here. Additional studies are required to definitively answer the question as to whether antiparticles can be guided by insulating capillaries.

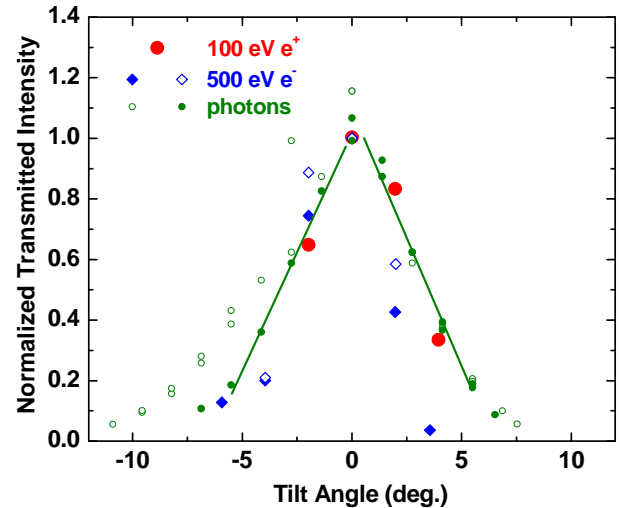


Figure 1. Normalized transmitted beam intensity as function of capillary tilt angle for 100 eV positrons (stars), 500 eV electrons (filled and open diamonds), and photons (open and filled circles). The filled and open diamonds are for two different horizontal positions of the capillary. The open and filled circles are for an uncoated and a coated capillary inner surface. The lines are to guide the eye through the coated capillary photon data.

Acknowledgements

This work supported by the National Science Foundation. We also thank Mr. Ferenc Turi for the technical support.

a) Missouri University of Science and Technology, Rolla, MO USA

[1] R.D. DuBois, and K. Tőkési, Nucl. Instr. and Meth. Phys. (2011) in press.

4.7 Ionization by intense and short electric pulses - classical picture

K. Tórkési and D.G. Arbó^{a,b)}

In the last decades there has been a great revival of the classical trajectory Monte Carlo (CTMC) calculations applied to atomic collisions involving three or more particles. This approximation seems to be useful in treating atomic collisions where the quantum mechanical calculations become very complicated or intractable, which is the case usually when higher order perturbations should be applied or many particles take part in the processes. The CTMC method has been quite successful also in dealing with the ionization process in laser-atom collisions when, instead of charged particles, electromagnetic fields are used for excitation of the target.

In the present work we studied the efficiency of the CTMC method. At first the electron emission spectra of a hydrogen atom when it is excited by ultra-short pulses are studied. The effect of a short pulse on one atom can be treated within the framework of a sudden momentum transfer, (or kick) i.e. in strong field approximation (SFA) where the pulse duration is much less than the classical orbital period of the electron in the initial state. We applied the Coulomb-Volkov approximation (CVA) for the determination of the energy differential electron distributions. Moreover, we extended these studies for short half-cycle pulses (HCP) of finite (non-zero) duration, where the pulse can be longer than the classical orbital period of the electron in the initial state and, therefore, the sudden approximation - when the effect of a short pulse on one atom can be treated within the framework of a sudden momentum transfer - is no longer valid. We analyzed the efficiency also of the various quantum approaches like the singly-distorted Coulomb-Volkov (SDCV) and the doubly-distorted Coulomb-Volkov (DDCV)

approximations. Quantum and classical results are compared to the numerical solution of the time-dependent Schrödinger equation (TDSE).

We conclude that the region of validity of the different quantum and classical approximations studied in this paper depends on the kick strength Δp and the pulse duration. The CTMC-T method is able to reproduce the quantum ionization probabilities for large Δp values, even for long pulse durations. For small Δp values quantum approaches are preferable compared to the quasiclassical one, as we depart from the sudden limit. It is in the intermediate limit, i.e., $\Delta p \approx 1$, where known quantum and classical approximations fail. Precisely in this region, DDCV becomes a better alternative than the SDCV, although a deficiency arises at small electron ejection energy for high values of Δp . Summarizing, our DDCV presents a reliable approximation where the CTMC and CTMC-T fails.

Acknowledgements

This work was carried out with financial support of CONICET, UBACyT X147, and ANPCyT PICT 2006-00772 of Argentina, the Argentine-Hungarian collaboration HU/08/02, the CNCSIS-UEFISCSU proj.No.PNII-IDEI 539/2007, the Hungarian National Office for Research and Technology and the Hungarian Scientific Research Found OTKA (K72172). KT were also partially supported by the European COST Action CM0702.

- a) Institute for Astronomy and Space Physics, IAFE, CC 67, Suc. 28 (1428) Buenos Aires, Argentina
 - b) Department of Physics, FCEN, University of Buenos Aires, Argentina
- [1] K. Tórkési, and D.G. Arbó, Proceedings book of MicroCAD 2011 International Scientific Conference. Miskolc, Hungary, Miskolci Egyetem 31 March 1 April 2011 (2011) 81-86.

4.8 State selective electron capture in low energy positron and argon collisions

K. Tőkési

Understanding the capture process during atomic collisions is fundamental both the experimental and theoretical point of view. Theoretically, one of the main difficulties in the accurate determination of the charge exchange cross sections is that the many-body interactions among collision partners have to be taken into account. This behavior is significant for positron impact where the projectile trajectory is spread in three-dimensional space and cannot be approximated by a straight-line trajectory, as is done for heavy projectile impact. Therefore, the success of different approaches strongly depends on their ability to describe the many-body character of the collision.

In this work the collisions between positrons and argon atoms are studied theoretically at impact energies between 10 and 60 eV. We treat the collision problem in the framework of a classical trajectory Monte Carlo (CTMC) model. It was shown that the CTMC method can be applied to light projectile impact. It is a non-perturbative method. All interactions between the colliding partners can be taken into account exactly during the collision.

10^6 of classical trajectories were computed to calculate total and state selective capture cross sections. Large numbers of trials were required because the total cross sections are composed of the cross sections for the many partial levels. The statistical error of the calculated total cross section data were below 2%.

In the recent studies the maximum impact energy is 60 eV therefore electrons from $n=3$, i.e. from 3p and 3s shells of Ar atom contribute to the total positronium formation cross sections. The major contribution originates from 3p shell of the argon atom. The contribution of the 3s shell of the Ar to the total positronium

formation cross section is about 1-5 %.

We found that, in most of the cases, ground state positronium is formed [1]. We found excellent agreement with the experimental data above 40 eV incident energies [2]. We also presented an accurate prediction for excited positronium formation cross sections (see Fig. 1.). We hope that our present results will encourage experimentalists to measure these cross sections in the near future.

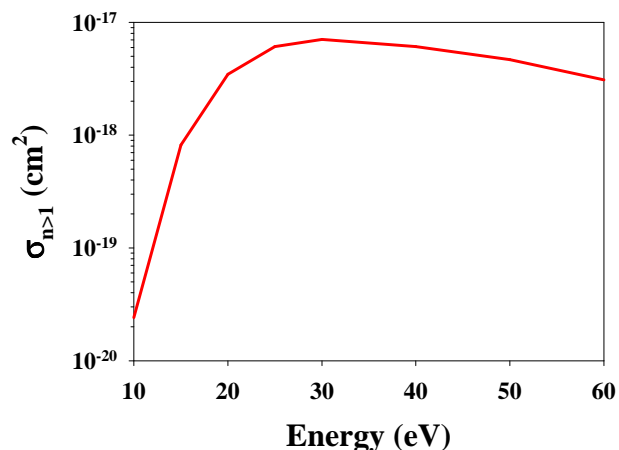


Figure 1. Prediction for excited positronium formation cross sections in collisions between positrons and argon atoms.

Acknowledgements

This work was supported by the Hungarian Scientific Research Fund OTKA No. K72172. The author would like to express his personal thanks to Andrew Bergman for the critical reading of the manuscript.

- [1] K. Tőkési, Nucl. Instr. and Meth. Phys. (2011) in press.
- [2] A.C.L. Jones, C. Makochekanwa, P. Caradonna, D.S. Slaughter, J.R. Machacek, R.P. McEachran, J. P. Sullivan, and S. J. Buckman, A. D. Stauffer, I. Bray and D. V. Fursa, Phys. Rev. A **83** (2011) 032701.

4.9 Iterative solution of the time dependent Schrödinger equation

Zs.G. Kiss^{a)}, L. Nagy^{a)}, K. Tókeşi and S. Borbély^{a)}

The most accurate theoretical method used to investigate the interaction between atoms and ultrashort (few-cycle) UV / XUV laser pulses is the direct numerical solution of the time dependent Schrödinger equation (TDSE). The aim of the present work is to test various methods used for the solution of the TDSE, and to find the less resource consuming one.

The recently developed iterative solution of TDSE (iTDSSE model) is an extension of the momentum-space strongfield approximation (MSSFA) [1], in which the Coulomb potential was considered only as a first order perturbation. In the iTDSSE model the higher order terms were gradually introduced, until convergence was achieved. The converged iTDSSE results were compared with the "exact" results, obtained from the direct solution of the TDSE (see [2-3]).

The MSSFA method provides accurate results only in the half-cycle pulse limit [1], and its shortcomings are revealed only in the long pulse limit. As any perturbative approach, the MSSFA time propagation is not unitary (norm of the wave function is not conserved). Beside this due to the weak Coulomb potential (i.e. first order perturbation) the ionization probability amplitude is overestimated and the $\Delta l = \pm 1$ selection rule is not fulfilled, which leads to erroneous wave function dynamics. The direct solution of the TDSE does not have the above presented shortcomings, but during production runs it requires a large amount of CPU power and memory even in the framework of the single active electron approach.

The newly implemented extension of the MSSFA model (the iTDSSE model) eliminates all the MSSFA model's shortcomings providing accurate results. The main advantage of the iTDSSE model is that it requires considerably less computer resources (CPU time and memory) than the direct solution, while it provides results as accurate as the direct solution.

The most critical part of the iTDSSE approach is the temporal propagation, which involves the calculation of a rapidly oscillating function's integral several times. These integrals can be performed efficiently by using the method of Levin [4], which significantly reduces the runtime of the iTDSSE model compared to the direct solution.

To illustrate the fast convergence and accuracy of the iTDSSE method on Figure 1 we have plotted iterative solutions up to the 10th order along with the direct solution. It can be observed that converged results were obtained after 5 iterations, and that the converged results are in excellent agreement with the direct solutions of the TDSE.

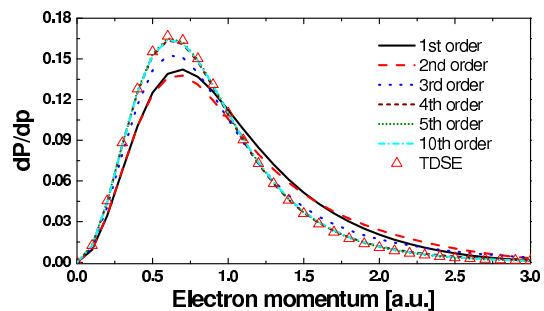


Figure 1. Ionization probability densities of hydrogen atom as a function of electron ejection momentum. The duration of the used half-cycle pulse is 1 a.u., and its amplitude is 0.75 a.u.

Acknowledgements

This work was supported by a grant of the Romanian National Authority for Scientific Research, CNCS – UEFISCDI, project number PN-II-ID-PCE-2011-3-0192, the European COST Action CM0702, by the Sectoral Operational Programme for Human Resources 2007-2013, co-financed by the European Social Fund under the project number POSTDRU 89/1.5/S/60189.

a) Faculty of Physics, Babes-Bolyai University, Cluj-Napoca, Romania

- [1] S. Borbély et al, PRA **77** (2008) 033412.
- [2] S. Borbély et al, Cent. Eur. J. Phys. **8** (2010) 249.
- [3] S. Borbély et al, Eur. Phys. J. D **59** (2010) 193.
- [4] D. Levin, J. Comp. and Appl. Math **67** (1996) 95.

4.10 Energy and angular differential recoil ion spectra in collisions between positron and helium atom

K. Tókési

The study of the energy and angular distributions of the ejected particles following atomic collisions mirror all details of the collision dynamics. In the ideal case all particles can be detected experimentally as functions of the scattering angle and energy. This experimental technique is known as reaction microscopy.

In this work we studied the collision between a 50 eV positron and helium atom [1]. We focused on the recoil ion spectra instead of the analysis of the electron and positron spectra. We treat the collision problem in the framework of a classical trajectory Monte Carlo (CTMC) model. The CTMC method is a nonperturbative method, where the classical equations of motion are solved numerically. In the present work the CTMC simulations were made in the three-body approximation. The detail of the calculation procedure can be found in ref [2]. We followed 5×10^7 primary trajectories and the double differential correlation pattern between the recoil energy and the scattering angle of the recoil ion was calculated. Fig. 1 shows the doubly differential spectra of recoil ion as a function of the scattering angle and the recoil energy. The small angles and small recoil energies belong to elastic and excitation channels. Larger angles with corresponding recoil energies can be attributed to the ionization channel. The solid black line shows the border between the channels of the ionization and electron capture to the bound state of the projectile. This border line can be attributed to the so called electron capture to the continuum (ECC) process. This treatment of the ECC process demonstrates reasonably well the original picture of the process where the ECC

was explained as a result of a special case of ionization, where the ionized target electron is strongly influenced by the outgoing projectile, or in other words, when the atomic electron is dragged by the projectile continuum state and moves with it. In the electron spectrum the ECC peak appears at the energy where the electron velocity is almost the same as the projectile velocity.

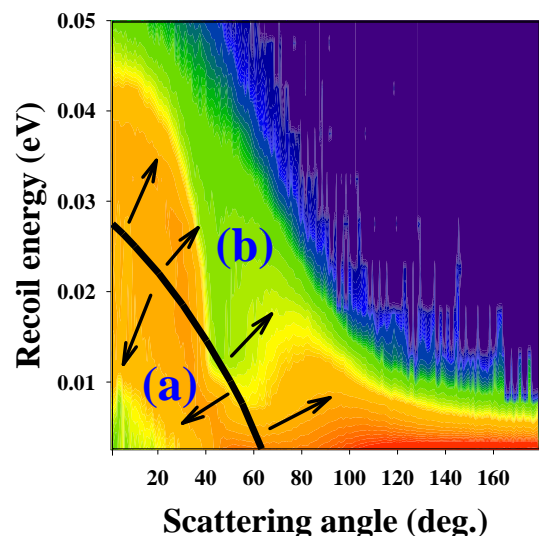


Figure 1. Prediction for excited positronium formation cross sections in collisions between positrons and argon atoms.

Acknowledgements

This work was supported by the Hungarian Scientific Research Fund OTKA No. K72172.

- [1] K. Tókési, Conference program and abstracts of the 27th International Conference on Photonic, Electronic and Atomic Collisions (XXVII ICPEAC), 27 July - 2 August 2011 Queen's University Belfast, UK, Edited by Ian Williams, Gleb Gribakin and Hugo van der Hart, CD, Fr108
- [2] K. Tókési, Á. Kövér, J. Phys. B 2000 **33** 3067.

4.11 Experimental (e,2e) study of resonant Auger states of Ar

B. Paripás^{a)}, B. Palásthy^{a)}, M. Žitnik^{b)}, K. Tókési

Electron spectra emitted after 2p inner-shell excitation of argon were studied by (e,2e) coincidence technique based on cylindrical mirror analyzers. The transmitted energy to the atom – i.e. the energy difference of the primary and scattered electrons – corresponded to the energy positions of Ar L³ inner-shell excited atomic states. Particularly the 2p→4s (244,4 eV) and the dipole forbidden 2p→4p (245,7 eV) excitations were studied extensively. The resonant Auger spectra were obtained by the removal of the background caused by the outer-shell electrons. The latter was measured at about 240 eV transmitted energy, where the inner-shell processes are not possible. The spectra reported by our group represent the first experimental data concerning resonant Auger spectra emitted upon electron impact excitation [1,2]. In particular, the resonant Ar[2p_{3/2}]4p Auger spectrum is reported

for the first time. The 4s spectrum displays a substantially larger shake-up contribution than the one observed in photoexcitation experiments, which may be explained by the interference of the resonant decay path with the direct ionization-excitation of the Ar 3p subshell.

Acknowledgements

This work was carried out as part of the TÁMOP-4.2.1.B-10/2/KONV-2010-0001 project in the framework of the New Hungarian Development Plan.

- a) Department of Physics, University of Miskolc, 3515 Miskolc-Egyetemváros, Hungary
- b) J. Stefan Institute, Jamova 39, P.O.B. 3000, SI 1000, Ljubljana, Slovenia
- [1] B. Paripás, B. Palásthy, M. Stuhec and M. Žitnik, *Physical Review A*, **82** (2010) 032508-1-10.
- [2] B. Paripás, B. Palásthy, M. Žitnik and K. Tókési, *Nucl. Instr. and Meth. B* (2011), doi:10.1016/j.nimb.2011.10.039

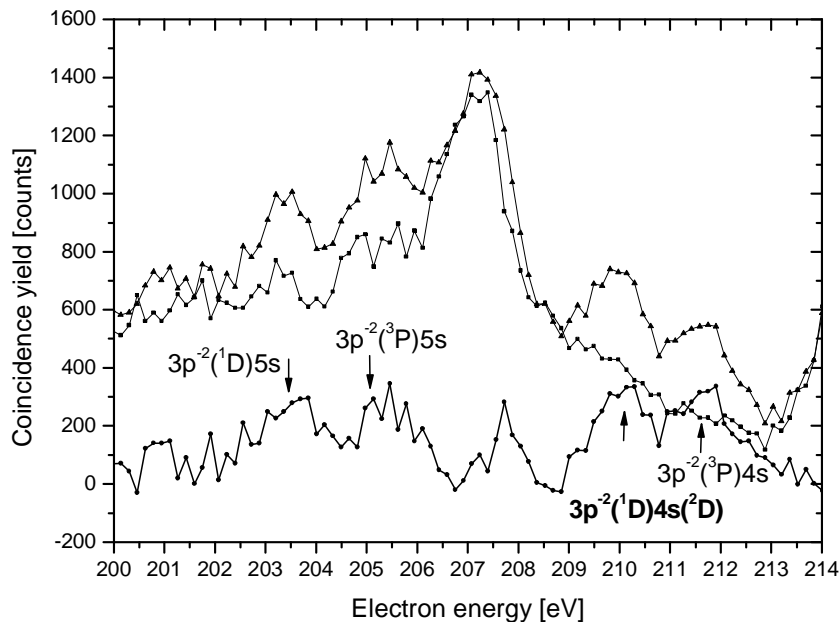


Figure 1. The resonant Auger spectrum emitted by Ar[2p_{3/2}]4s state (thick line with circles), obtained as a difference of (e,2e) spectrum measured at $E_0 = 343.6$ eV (thin lines with triangles) and the direct ionization background (thin lines with squares).

4.12 Broadening of electron beams through a single glass macrocapillary

R.J. Berezky, B.S. Dassanayake^{a)}, K. Tókési, J.A. Tanis^{a)}

The interaction of charged particles with insulating capillaries has motivated the development of nanotechnology. The interaction of slow (few keV) highly charged ions (HCI) with several kinds of insulating capillaries has been studied recently, experimentally and theoretically.

These studies have shown that a considerable fraction of the ions are transmitted through the nanocapillary without close collisions with the inner wall. Moreover, the transmission of slow negative ions through insulating nanocapillary foils shows that these ions can also be guided through nanocapillaries. Studies also include faster electrons transmitting through Al_2O_3 nanocapillaries, polyethylene terephthalate (PET) nanocapillaries, and a single glass macrocapillary. Results for electrons (200 to 350 eV) through highly ordered insulating Al_2O_3 nanocapillaries with a large aspect ratio of 100 show evidence of guiding. Even faster electrons (500 and 1000 eV) show guiding through PET capillaries with considerable energy loss increasing with tilt angle due to inelastic scattering with the inner surface of the capillary. For the single glass macrocapillary, the transmitted electrons are found to lose energy for the same reason. Guiding is also achieved with the single glass macrocapillary for slow highly-charged ions, but no energy loss is seen. Single glass capillaries have been applied with the intention of producing sub-micrometer sized beams that can be used for surface modification or to selectively damage the structure of biological cells.

We investigated the broadening of electron beams when traveling through an insulating single cylindrically-shaped glass capillary of macroscopic dimensions [1]. Glass capillary samples (diameters $d = 0.18$ and 0.23 mm and lengths $l = 14.4$ and 16.8 mm) made of Borosilicate glass were subjected to bombardment by ~ 500 eV electrons. Defocusing effects have also been observed in most

of the electron transmission experiments conducted using both nanocapillary foils, as well as straight glass capillaries suggesting the existence of a charge distribution at the exit. But compared to broader transmission profiles for HCIs electron transmission profiles obtained in this experiment show almost a two times lower FWHM value (1.1°) at the sample tilt angle $\Psi = 0^\circ$. We found that the electron charge-up distribution at the capillary exit is weaker than that of ions under similar conditions. When the centroid energies (weighted mean values of the transmitted energy spectra) were plotted against observation angle Θ (measured with respect to incident beam direction as well) at different Ψ (Fig. 1), the outer edges of the transmitted broadened beam showed considerably lower energy values than for the center of each Ψ . This is a result of electron interaction with capillary walls at the point of exit due to the weak exit charge distribution.

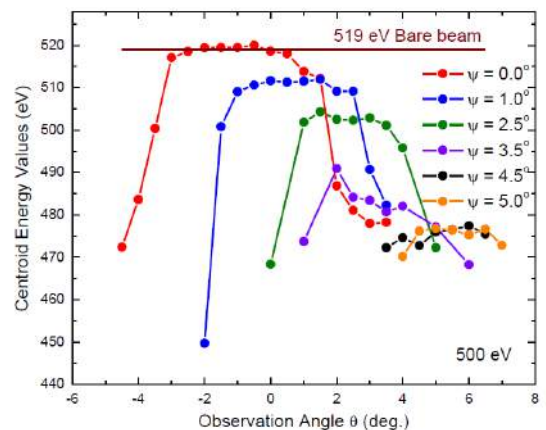


Figure 1. Centroid energy as the function of observation angle Θ at 520.7 eV for different tilt angles. Solid line shows the primary beam (without the sample) centroid energy value.

a) Department of Physics, Western Michigan University, Kalamazoo, MI 49008, USA

[1] B.S. Dassanayake, R.J. Berezky, Tókési, J.A. Tanis, NIM. B 269 1243 (2011).

4.13 Charge evolution associated with electron transmission through a single glass macrocapillary

R.J. Berezky, B.S. Dassanayake^{a)}, K. Tőkési, J.A. Tanis^{a)}

The interaction of slow highly charged ions (HCIs) and electrons with insulator surfaces has been vigorously studied in the last few decades. In recent years focus has been shifted to the more challenging and difficult transmission of charged particle through linear structures such as capillaries of nano- and macro-meter scales.

Studies on ion guiding have revealed that the inner walls of the capillaries collect charges in a self-arranging manner such that electrostatic repulsion inhibits close collisions with the surface and, in turn, prevent electron capture to the projectile, allowing ions to be guided through.

Electrons on the other hand have somewhat different transmission characteristics compared to those of HCIs. In addition to electrostatic deflection caused by electron deposition close to the capillary entrance, similar to the case of HCIs, a significant contribution from inelastic electron transmission has also been observed. The energy losses which give rise to inelastic transmission have been identified as a result of interactions of electrons with the inner capillary surface (or bulk) close to the entrance caused by weak charge up effects. These energy losses are attributed to processes such as ionization and excitation of valence band and inner- shell electrons of the capillary material.

In this work we studied the charge evolution at observation angles slightly away from the centroid angular position at 520.7 and 824.5 eV incident beam energies [1]. Transmission of 313.3, 520.7, 824.5, and 1028.8 eV electrons through the straight glass capillaries were investigated. This further proves the existence of a discharging/charging mechanism of the inner surface close to the capillary entrance. We found that the results give evidence for beam movement across the capillary exit, attributed to the changing electric field distribution caused by charge accumulation close to the capillary entrance at the beginning until equilibrium is reached. The dynamics of the

centroid energy values as a function of time (charge) elapsed suggest that the initial inelastic interactions of the transmitted electrons with the inner walls becomes less prominent with increasing charge deposition on the capillary surface (see Fig. 1), giving rise to more relatively elastic transmission at the end. Moreover, in the direct region of transmission, the centroid energy values were found to be almost equal to the primary beam energy, whereas an exponential decrease was observed with the increase of sample tilt angle into the indirect region.

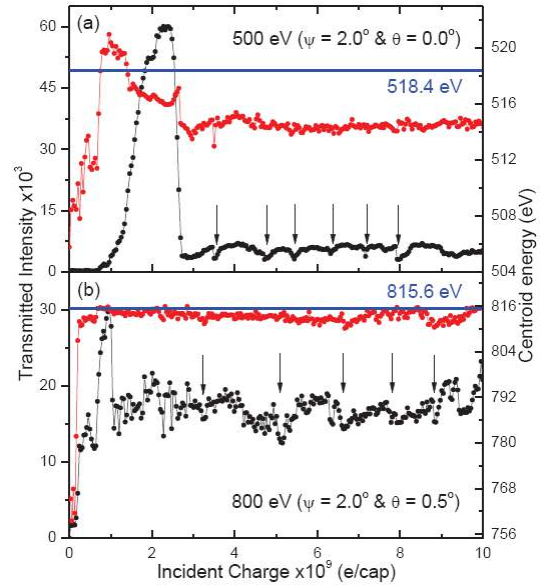


Figure 1. Variation of intensity (black points) and centroid energies (red points) with integrated charge at $\Psi = 2^\circ$ for 520.7 and 824.5 eV with $\Theta = 0^\circ$ and 0.5° , respectively. Blue solid lines show the centroid (520.7 and 824.5 eV) values for the primary (bare) beam without the sample. Black arrows point to the sudden intensity drops that occurred from time to time.

a) Department of Physics, Western Michigan University, Kalamazoo, MI 49008, USA

[1] B. S. Dassanayake, R. J. Berezky, S. Das, A. Ayyad, K. Tőkési and J. A. Tanis, Phys. Rev. A. 83, 012707 (2011).

4.14 Mutual neutralization in low-energy $H^+ + F^-$ collisions

J.Zs. Mezei, N. Elander^{a)}, Å. Larson^{a)}

In hydrogen and fluorine containing plasmas, mutual neutralization in collisions of H^+ and F^- ions can be an important source of charge removal. The mutual neutralization reaction among the two ions has as far as we know never been studied theoretically nor experimentally. We have previously studied dissociative recombination [1] and ion-pair formation [2] in electron recombination with HF^+ ions.

In the present work [3], the cross section for mutual neutralization in collisions between H^+ and F^- ions at low energies ($E < 10$ eV) is calculated using a molecular close-coupling approach with a quasidiabatic representation of the potentials and couplings determined from adiabatic potentials [2]. The nuclear dynamics for the coupled electronic states was described quantum mechanically including very high angular momentum for the colliding fragments. The effect of autoionization was considered in the so-called local (boomerang) model by letting the potential energy curves become complex valued.

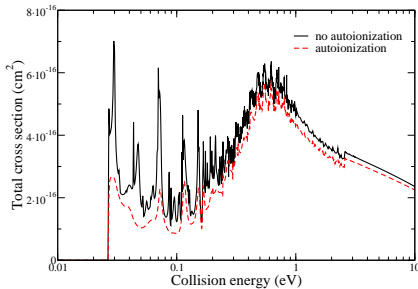


Figure 1. Total cross section for mutual neutralization in low-energy collisions of H^+ and F^- .

The coupled Schrödinger equation for the nuclear motion is solved using a numerical integration of the corresponding matrix Riccati equation and the cross section for mutual neutralization is computed from the asymptotic value of the logarithmic derivative of the radial wave function.

The cross section has a sharp threshold and is dominated by the formation of the $H(n = 2) + F(^2P)$ fragments. The magnitude of the cross section is small compared to a system

such as $H^+ + H^-$, which in contrary to the $H^+ + F^-$ colliding system, has curve crossings between ionic and covalent states occurring at large internuclear distances. For $H^+ + F^-$, sharp oscillations are observed in the cross section. The structures are broadening or smeared out and the magnitude of the cross section is decreased when autoionization is added to the model. In order to understand and identify these resonant structures, angular momentum quantum numbers are assigned to them.

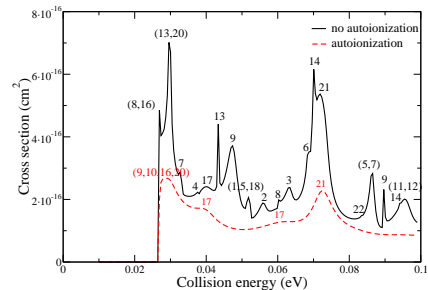


Figure 2. Labeling of the resonant structures with the angular momentum quantum number.

Some resonant structures originate almost exclusively from a single partial wave, while for other structures, several partial waves contribute.

Surprisingly little has been done on mutual neutralization reactions both experimentally and theoretically. Currently a new electrostatic storage device DESIREE [4] is being built at AlbaNova, SU, in order to fill this gap. The colliding system studied here, can be a good candidate to be studied using this device.

Acknowledgements

Å.L. and N.E. acknowledge support from the Swedish Research Council. J.Zs.M. acknowledges support from the Wenner-Gren Foundation.

- a) Department of Physics, Stockholm University, S-106 91 Stockholm, Sweden
- [1] J. B. Roos, Å. Larson and A. E. Orel, Phys. Rev. A **76** (2007) 042703.
- [2] J. B. Roos, A. E. Orel and Å. Larson, Phys. Rev. A **79** (2009) 062510.
- [3] J. Zs. Mezei, J. B. Roos, K. Shilyaeva, N. Elander and Å. Larson, Phys. Rev. A **84** (2011) 012703.
- [4] R. D. Thomas et al., Rev. Sci. Instr. **82** (2011) 065112.

4.15 Resonances in photoionization: Cross section for vibrationally excited H₂

J.Zs. Mezei^{a,b}, I.F. Schneider^b, E. Roueff^c, Ch. Jungen^a

Diatomic molecular Hydrogen is the most abundant molecule in interstellar molecular clouds. The modeling of these environments relies on accurate cross sections for the various relevant processes. Among them, the photoionization plays a major role in the kinetics and in the energy exchanges involving H₂. The recent discovery of vibrationally excited molecular hydrogen in extragalactic environments revealed the need for accurate evaluation of the corresponding photoionization cross sections.

In the present work [1] we report theoretical photoionization cross sections for excitation from excited vibrational levels of the ground state, dealing with the Q($N = 1$) ($\Delta N = 0$, where N is the total angular momentum of the molecule) transitions which account for roughly one third of the total photoabsorption cross section. We will focus on the $v'' = 1$ excited level of the ground electronic state.

Our calculations are based on Multichannel Quantum Defect Theory (MQDT) [2], which allows us to take into account of the full manifold of Rydberg states and their interactions with the electronic continuum.

We have carried out two types of MQDT calculations. First, we omitted all open channels and calculated energy levels, wave functions and spontaneous emission Einstein coefficients, making use of the theoretical method presented in [2]. In a second set of calculations we included the open ionization channels in the computations getting the continuum phase shifts, channel mixing coefficients and channel dipole moments and finally the photoabsorption/photoionization cross section.

The cross section is dominated by the presence of resonance structures corresponding to excitation of various vibrational levels of bound electronic states which lie above the ionization

threshold.

In order to assess the importance of the resonances we have calculated for each vibrational interval (the energy interval between two consecutive ionization thresholds) the averaged photoabsorption/photoionization cross section and we found that at low photon energies, near the ionization thresholds (vibrational levels of the ground electronic states of the molecular ion), the resonance enhancement exceeds the background cross section (direct ionization) by more than one order of magnitude, while at higher energies it is still more than a factor of two larger than the latter.

A detailed examination on the relative contributions to the photoabsorption and photoionization cross sections of the resonances associated with the vibrational levels of $n\pi\pi$ $^1\Pi_u^-$, $n = 3 - 6$ electronic states shows that more than 42% of the total photoionization cross section and more than 35% of the photoabsorption cross section are produced by the four lowest electronic states.

Acknowledgements

J.Zs.M. acknowledges support from the French ANR project *SUMOSTAI* and from the *CPER Haute-Normandie/CNRT Energie, Electronique, Matériaux*. I.F.S., E.R. and Ch.J. were supported by the ANR (France) under the contract *09-BLAN-020901*.

a) Laboratoire Aimé-Cotton, CNRS et Université Paris Sud, Bat. 505, F-91405, Orsay, France

b) Laboratoire Ondes et Milieux Complexes, CNRS et Université du Havre, F-76058 Le Havre, France

c) LUTH, Observatoire de Paris et Université Paris 7, F-92190 Meudon, France

[1] J. Zs. Mezei, I. F. Schneider, E. Roueff and Ch. Jungen, submitted to *Phys. Rev. A*.

[2] Ch. Jungen, *Elements of Quantum Defect Theory*, edited by M. Quack and F. Merkt, *Handbook of High Resolution Spectroscopy*, (Wiley, Chichester and New York, 2011).

4.16 Photon energy dependence of left-right asymmetry parameters of Kr 4p photoelectrons in the vicinity of 3d resonant excitations

S. Ricz^{a,b)}, T. Buhr^{a,b,c)}, K. Holste^{b)}, A.A. Borovik, Jr.^{b)}, D. Bernhardt^{b)}, S. Schippers^{b)}, Á. Kövér^{a)}, D. Varga^{a)}, and A. Müller^{b)}

A left-right asymmetry was observed experimentally for the outer s -shell photoelectrons of noble gases and of the H_2 molecule in our previous studies [1,2] (see the cited articles for the definition of “left” and “right” as well as for the details of the experimental method). Recently, the angular distribution of $4p$ photoelectrons of Kr was measured with linearly polarized synchrotron radiation in the photon energy range (90 – 94.4 eV) of the $3d^{-1} \rightarrow np$ resonant excitations in order to determine the anisotropy parameters [3]. Now, also the left-right asymmetry parameters have been determined from the measured spectra of Ref. [3]. The experiment was performed at beamline BW3 of the DORIS III storage ring at HASYLAB (Hamburg, Germany). The emitted electrons were analyzed using the ESA-22D electrostatic electron spectrometer [4].

Fig. 1 shows the measured left-right asymmetry parameters (A_{LR}) of the two fine structure components of Kr $4p$ photoelectrons. The asymmetry parameters (A_{LR}) are increasing with increasing photon energies reaching a maximum value of 0.04, definitely different from zero when considering the error bars. Furthermore, the left-right asymmetry parameters oscillate around the $(3d_{3/2,5/2})^{-1} \rightarrow 5p$ resonant excitation for both fine structure components. Currently, we do not know what kind of interaction can produce a left-right asymmetry in photon-atom collisions but the shape of the oscillations shows interference between the unknown and the resonant excitation channels. One of the most important observations is that the sign of A_{LR} changes from positive to negative and then back again to positive just within a narrow photon energy range of only 250 meV around the $(3d_{5/2})^{-1} \rightarrow 5p$ resonant excitation. Within such a narrow range artificial asymmetry of the experimental setup is totally unconvivable.

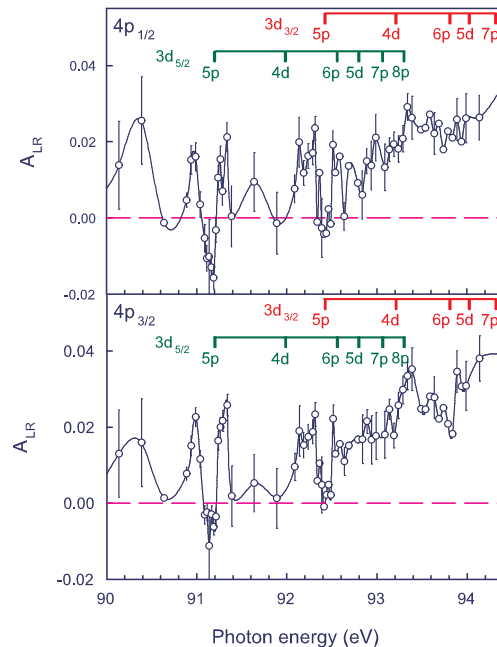


Figure 1. Experimental left-right asymmetry parameters for the Kr $4p_{1/2,3/2}$ photoelectrons (open circles with connecting line). The vertical bars with assignments show the resonance energies. The dashed lines represent the left-right asymmetry parameters predicted by quantum mechanics.

Acknowledgements

The authors thank the DORIS III staff for providing excellent working conditions. This work was supported by the NKTH-OTKA (Grant No. K67719), and by the European Community-Access to Research Infrastructure Action of the Improving Human Potential Program. Financial support by DESY is gratefully acknowledged.

- a) ATOMKI, Debrecen, P.O. Box 51, H-4001, Hungary
- b) Institut für Atom- und Molekülphysik, Justus-Liebig-Universität Giessen, D-35392 Giessen, Germany
- c) PTB, D-38116 Braunschweig, Germany

- [1] T. Ricsóka, *et al.* J. Phys. Conf. Ser. 194 (2009) 012003
- [2] S. Ricz, *et al.* New J. Phys. 9 (2007) 274
- [3] S. Ricz, *et al.* Phys. Rev. A 81 (2010) 043416
- [4] S. Ricz, *et al.* Phys. Rev. A 65 (2002) 042707

4.17 Interaction between 4p photoionization and 3p resonant excitation channels of krypton

T. Buhr^{a)}, S. Ricz^{b,c)}, K. Holste^{c)}, A.A. Borovik, Jr.^{c)}, D. Bernhardt^{c)}, S. Schippers^{c)}, Á. Kövér^{a)}, D. Varga^{a)}, and A. Müller^{a)}

The angular distribution of Kr 4p photoelectrons was measured employing a linearly polarized photon beam at energies from 205 eV to 230 eV. In this range the Kr 3p \rightarrow ns/md (n,m=4,5,6,...) resonances can be excited. The experimental anisotropy parameters (β , γ and δ) were determined for the Kr 4p shell and its fine structure components.

The measurement was carried out at beam-line BW3 of the DORIS III synchrotron light source at HASYLAB (Hamburg, Germany). The ESA-22D electrostatic electron spectrometer was used to analyze the emitted electrons. The spectrometer consists of a spherical and a cylindrical mirror analyzer. The spherical mirror focuses the electrons from the scattering plane to the entrance slit of the cylindrical analyzer performing the energy analysis of the electrons. (For detailed description of an ESA-22-type electron spectrometer see Ref. [1].)

The measured dipole anisotropy parameters β of Kr 4p photoelectrons are shown in Fig.1 as a function of photon energy. Resonance-like structure can be seen in the photon energy dependence of the dipole parameters. This structure indicates that the channel interactions are important between the 3p resonant excitation-autoionization and 4p direct photoionization processes in krypton. The natural line width of the 3p photoelectron peaks was determined from the measured spectra and it is about 0.8 eV while the experimental width of the resonance near 220 eV photon energy ($3p_{1/2}^{-1}\rightarrow 5s$ resonant excitation) is approximately 2 eV in Fig. 1. This broadening can be explained with the strong interference between the ionization and excitation channels. As before [2], we conclude that the angular distribution of photoelectrons is strongly influenced by the excitation processes.

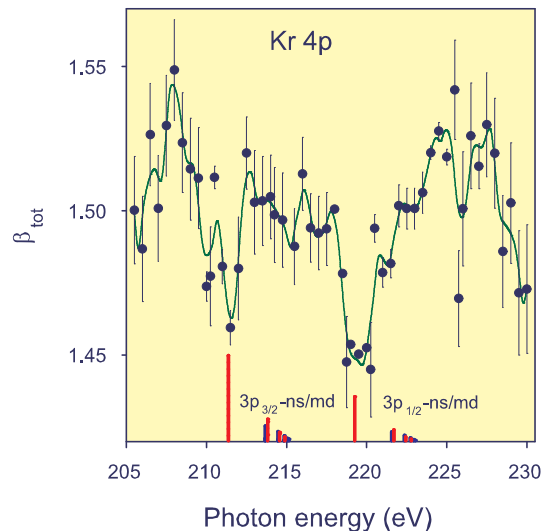


Figure 1. Photon energy dependence of the experimental dipole parameter β (solid circles) of Kr 4p photoelectrons. The solid (green) line is a smoothed curve guiding the eye. The vertical bars at the bottom (red bars: *ns*, blue bars: *md* excitations) denote the energy positions of the resonances shifted by 2.6 eV to lower energies with respect to calculated values obtained within the present investigation. The heights of the vertical bars are proportional to the oscillator strengths of the excitations.

Acknowledgements

The authors wish to thank the DORIS III staff for providing excellent working conditions. This work was supported by the NKTH-OTKA (Grant No. K67719), and by the European Community-Access to Research Infrastructure Action of the Improving Human Potential Program. Financial support by DESY is gratefully acknowledged.

- a) Physikalisch -Technische Bundesanstalt, Bundesallee 100, D-38116 Braunschweig, Germany
- b) ATOMKI, Debrecen, P.O. Box 51, H-4001, Hungary
- c) Institut für Atom- und Molekülphysik, Justus-Liebig-Universität Giessen, D-35392 Giessen, Germany

[1] S. Ricz, *et al.* Phys. Rev. A 65 (2002) 042707

[2] S. Ricz, *et al.* Phys. Rev. A 81 (2010) 043416

4.18 Lifetime measurement of the metastable $1s2s2p^4P_J^o$ state of the He^- ion in a cryogenically cooled electrostatic ion-beam trap

A. Orbán, P. Reinhed^{a)}, J. Werner^{a)}, S. Rosén^{a)}, R.D. Thomas^{a)}, I. Kashperka^{a)}, H.A.B. Johansson^{a)}, D. Misra^{a)}, L. Brännholm^{b)}, M. Björkhage^{b)}, H. Cederquist^{a)}, H.T. Schmidt^{a)}

The investigations of biomolecular and heavy cluster ions have focused the interest on electrostatic storage devices since the trapping conditions are mass independent. To get differentiated information about processes in which these ions are involved the determination of the initial quantum state is crucial. The majority of molecular ions relax to their rovibrational ground state during long-time storage in low temperature environment. At the moment two large scale electrostatic storage rings are under construction meant to operate in the 10-20 K temperature range: the Cryogenic Storage Ring in Heidelberg [1] and the Double ElectroStatic Ion Ring ExpERiment, DESIREE, at Stockholm University [2].

Combining electrostatic ion storage with low temperature environment we performed the first correction-free high-precision lifetime measurement of the metastable $1s2s2p^4P_{5/2}^o$ level of the He^- ion [3]. A small ion trap, Cone-Trap [4], was mounted in a cryogenic chamber designed for testing purposes for the DESIREE. Figure 1 shows the decay curve obtained by detecting the yield of neutrals as a function of time while trapping He^- ion. The fast-decaying component of the decay curve was assigned to the $^4P_{1/2}$ and $^4P_{3/2}$ levels (inset) while the slow-decaying component to the $^4P_{5/2}$ level. The detachment of the 4P_J state is not exclusively caused by the autodetachment process. Blackbody radiation induced photodetachment, collisional detachment between stored ions and residual gas particle, collisions between trapped ions, losses due to the presence of electrostatic field, instrumental effects also contribute to the measured decay rate:

$$\Gamma_{\text{measured}} = \Gamma_{\text{autodetach}}(^4P_J) + \Gamma_{BB} + \Gamma_{\text{coll}} + \Gamma_{\text{ion-ion}} + \Gamma_{\text{field}} + \Gamma_{\text{instr}} \quad (1)$$

We pointed out that all contributions to the measured rate except the autodetachment rate are negligible in our measurement. Namely, Γ_{BB} is 0.1 s^{-1} at 100 K and is decreasing considerably at 10 K. Γ_{coll} at 4×10^{-10} mbar we estimated to be $0.52 \pm 1.27 \text{ s}^{-1}$, and $\Gamma_{\text{ion-ion}} = 0$ since in each cycle we trapped 3-4 ions on aver-

age. Quasiclassical calculations show that the electrostatic field induced detachment through tunneling at our maximum electric field intensity of 1.7 kV/cm is not a significant process. The fine structure splitting of the $^4P_J^o$ levels of He^- is in the μeV range while the energy shift due to the Stark effect is in neV range therefore there is no mixing between different J levels. These facts lead to a negligible Γ_{field} . The instrumental contribution was estimated to be $\Gamma_{\text{instr}} = 0.17 \pm 0.06 \text{ s}^{-1}$. In this way the correction-free lifetime of the $^4P_{5/2}$ level was determined with unprecedented precision being $359.0 \pm 0.7 \mu\text{s}$. Assuming that the fine-structure levels were populated corresponding to their statistical weight the lifetime of the $^4P_{3/2}$ level was found to be $12.3 \pm 0.5 \mu\text{s}$ and $7.8 \pm 1.0 \mu\text{s}$ for the $^4P_{1/2}$ level.

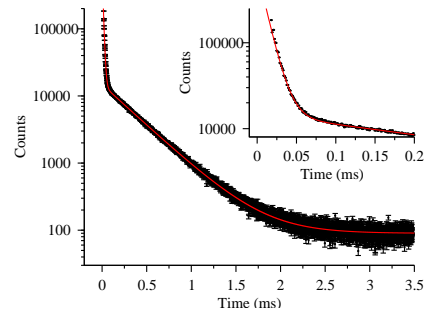


Figure 1. He signal on the MCP detector as the function of time in case of 2.5 keV He^- storage at 10 K and 1.5×10^{-10} mbar.

This result indicating the potentials of electrostatic and cryogenic storage devices also provides important data for theory.

- a) Department of Physics, Stockholm University, Alba-Nova University Center, 106 91 Stockholm, Sweden
- b) Manne Siegbahn Laboratory, Stockholm University, Frescattivägen 28, 11418 Stockholm, Sweden
- [1] D. Zajfman *et al.*, J. Phys. Conf. Ser. **4**, 296 (2005)
- [2] R.D. Thomas *et al.*, Rev. Sci. Instr. **82**, 065112 (2011)
- [3] P. Reinhed *et al.*, Phys. Rev. Lett. **103**, 213002 (2009)
- [4] H.T. Schmidt *et al.*, Nucl. Instr. & Meth. **173**, 523 (2001)

4.19 Classical Monte Carlo code for the determination of atomic cross sections for fusion related collision systems

K. Tórkési, M. O'Mullane^{a)}, D. Coster^{b)}

Interpretation of the cross sections in multi-electron ion-atom collisions is a challenging task for theories. The main difficulty is caused by the many-body feature of the collision, involving the projectile, projectile electron(s), target nucleus, and target electron(s). In the last decade large numbers of non-perturbative studies have been performed to explain experimental total-, single- and double-ionization and charge exchange cross sections. The success of various approaches depends strongly on how far a given theory is capable to describe the many-body character of the collision. Along this line the classical trajectory Monte Carlo (CTMC) method has been quite successful in dealing with the atomic processes in ion-atom collisions. The CTMC method treats the atomic collisions in a non-perturbative manner. Classical equations of motions are solved numerically with randomly selected initial conditions. One of the main advantages of the CTMC method is that the three-body interaction is exactly taken into account during the collision at a classical level.

The Integrated Tokamak Modeling Task Force (ITM-TF) was set up in Europe, under EFDA (the European Fusion Development Agreement), in 2004. The main target is to coordinate the European modeling effort and provide a complete European integrated modeling structure, with the highest degree of flexibility, for prediction of actual experiments and -in the long term - of the International Thermonuclear Experimental Reactor (ITER). For the ITM-TF a large numbers of atomic data is necessary. We have experience in theoretical interpretations of processes in ion-atom and ion-solid collisions based on classical descriptions. We developed a classical code for the determination of the cross sections for fundamental scattering processes.

To demonstrate the validity and the effi-

ciency of the present code we performed test calculations to determine the state selective charge exchange cross sections for collision system of $N^{7+} + H(1s)$ at a 50 keV/amu projectile energy (see Fig. 1). The present results are in excellent agreement with the previous results [1]. We also performed systematic calculation to determine charge exchange cross sections with other charge states of N ion. Further works are in progress and will be published soon.

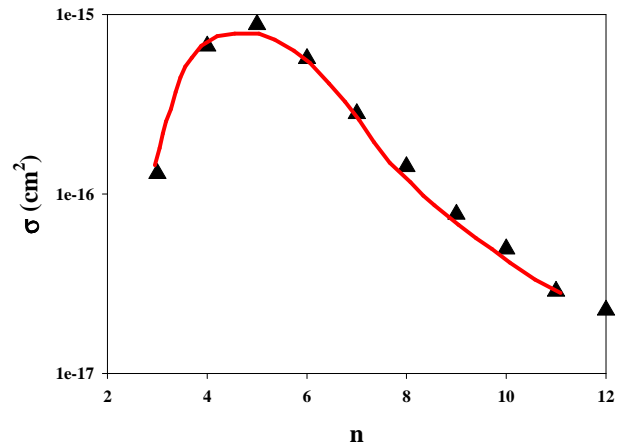


Figure 1. Electron capture cross sections to product n -levels for a N^{7+} colliding with $H(1s)$ at 50 keV projectile impact. Triangles: present results Solid line: previous calculations from Ref. [1].

Acknowledgements

This work, supported by the European Communities under the contract of Association between EURATOM-HAS, was carried out within the framework of the Task Force on Integrated Tokamak Modelling of the European Fusion Development Agreement.

a) CCFE, Culham Science Centre, Abingdon, Oxon, OX14 3DB, UK

b) Max-Planck-Institut für Plasmaphysik, Garching, Germany

[1] R.E. Olson, PRA **24** (1981) 1426.

4.20 Fragmentation of H_2O and CH_4 molecules induced by 1 MeV N^+ ion impact

S.T.S. Kovács, Z. Juhász, P. Herczku, B. Sulik

Fragmentation experiments performed with simple few-atomic molecules are important to understand fundamental molecular processes. In radiotherapy these processes cause radiation damages in biological systems, which may lead to cell death. Water and methane molecules as tissue-equivalent materials are regularly used to study radiation effects for the human body. Free radicals originating from water molecule fragmentation have major importance in DNA damages.

At Atomki we installed a new setup in order to investigate fragmentation of small molecules by ion impact. It was designed for accurately measuring the angular distribution of fragments in wide angular and energy range using an effusive molecular gas jet target and a specific electrostatic spectrometer placed in a large experimental chamber [1-3]. The first tests and preliminary measurements have been performed at the VdG 5 accelerator. Water and methane molecules in gas phase were used as targets and 1 MeV N^+ ions as projectiles. The energy of the fragments were measured at different angles from 20° to 160° relative to the incident N^+ beam. Figure 1 and 2 show the measured low energy methane and water spectra respectively. The peaks above 3 eV are due to H^+ ions originating from the target.

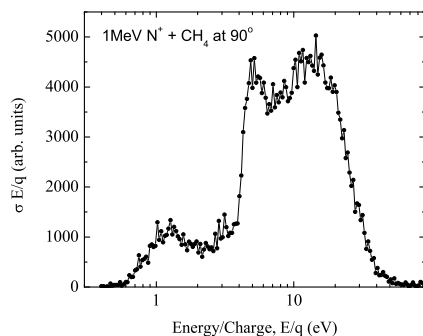


Figure 1. Measured methane fragment energy spectrum at the observation angle of 90° .

At higher energies only weak emission was

found. This is the range, where fragmentation is induced by binary collisions of the atomic centers, which is object of further studies. In both cases similar spectra were obtained as in earlier measurements with 800 keV He^{2+} projectile [4]. For the water spectrum the identification of different fragmentation channels is also shown in figure 2.

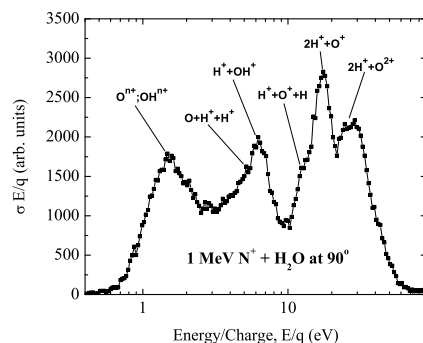


Figure 2. Measured water fragment energy spectrum at the observation angle of 90° .

Detailed analysis of the measured data is in progress.

Acknowledgements

This work was supported by the Hungarian National Science Foundation OTKA (Grant: K73703) and by the TÁMOP-4.2.2/B-10/1-2010-0024 project, co-financed by EU and the European Social Fund.

- [1] S. T. S. Kovacs, Effusive molecular gas jet target for molecule fragmentation experiments, ATOMKI Annual Report 2010 (2011) 56.
- [2] S. T.S. Kovács, P. Herczku, Z. Juhász, L. L. Horváth, B. Sulik, A new VdG-5 beamline for studying ion-atom and ion-molecule collisions, ATOMKI Annual Report 2010 (2011) 57.
- [3] P. Herczku, The development of an electrostatic spectrometer for low energy ions, ATOMKI Annual report 2010 (2011) 55.
- [4] B. Sulik, Z. Juhász, T. Ricsóka and N. Stolterfoht, Fragmentation of H_2O and CH_4 molecules in collisions with 800 keV He^+ , 13th ICPHCI, 2006, Belfast, Northern Ireland, UK, (Poster, Book of abstracts: p. 2-23), (2006).

4.21 Electron cloud simulation of the ECR plasma

R. Rácz, S. Biri, J. Pálkás

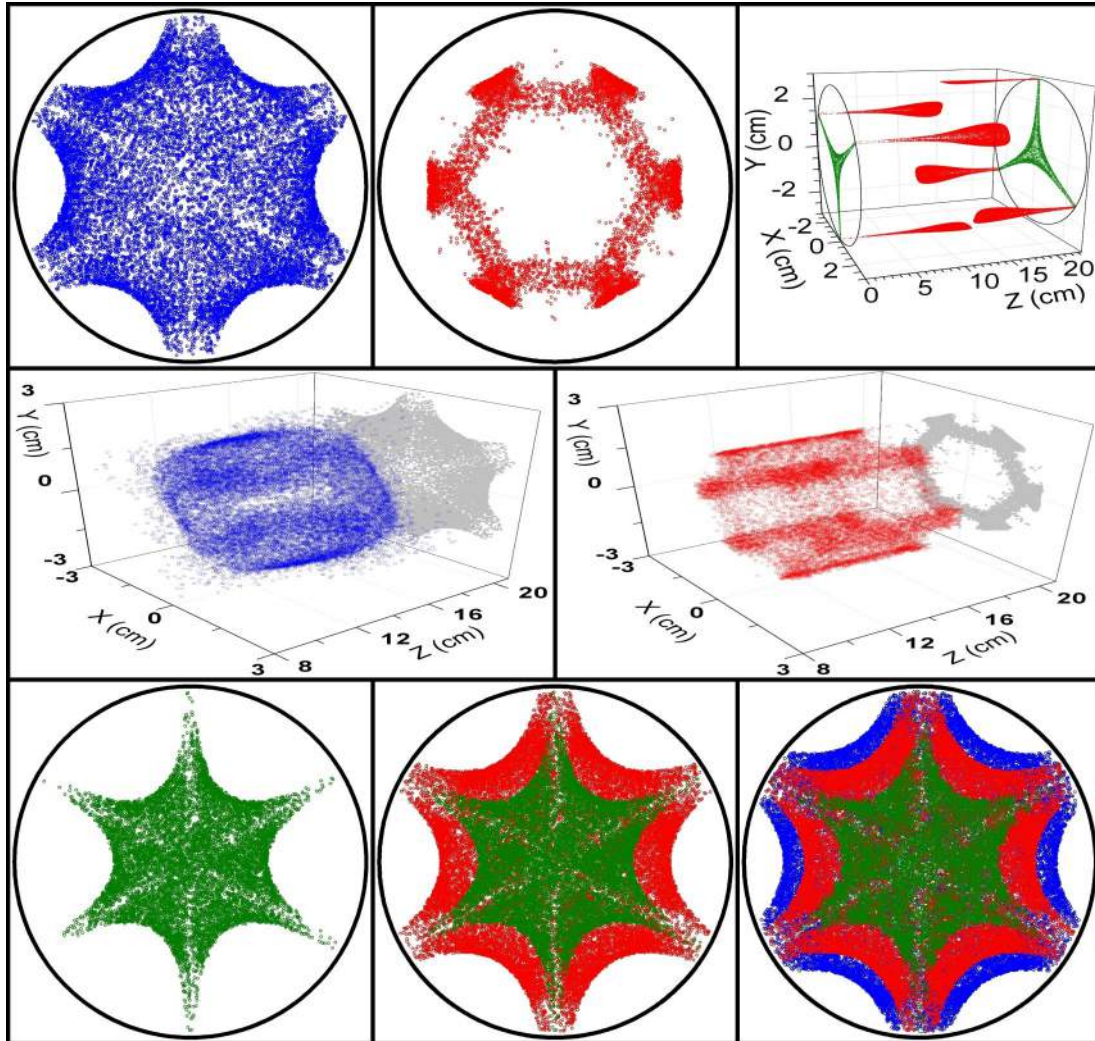


Figure 1. Simulated electron clouds. (Top part, from left to right) Cold and warm electron clouds followed by the traces of the hot electrons when stopped at the plasma chamber wall. (Middle part) Same cold and warm electron clouds in 3-D view. (Bottom) Single, double, and triple frequency couplings at ECR plasmas in 2-D axial view.

The plasma of the Electron Cyclotron Resonance Ion Source (ECRIS) of ATOMKI is being continuously investigated by different diagnostic methods: using small-sized probes or taking X-ray and visible light photographs. In 2011 three articles were published by our team in a special edition of the IEEE Transactions on Plasma Science (Special Issue on Images in Plasma Science) describing our X-ray [1] and visible light [2] measurements and plasma modeling and simulating studies [3]. Simulation

is in many cases the base for the analysis of the photographs. The outcomes of the X-ray and visible light experiments were presented already in earlier issues of the Atomki Annual Report [4, 5, 6], therefore in this year we concentrate on the results of the simulating studies.

The spatial distribution of the three main electron components (cold, warm and hot electron clouds) of the ECR plasmas was simulated by TrapCAD code [3]. TrapCAD is a “limited”

plasma simulation code. The spatial and energy evolution of a large number of electrons can be realistically followed; however, these particles are independent, and no particle interactions are included.

In ECRISs, the magnetic trap confines the electrons which keep together the ion component by their space charge. The electrons gain high energies while the ions remain very cold throughout the whole process. Thus, the spatial and energy simulation of the electron component gives much important and numerical information even for the ions.

The electron components of ECRISs can artificially be grouped into three populations: cold, warm, and hot electrons. Cold electrons (1-200 eV) have not been heated by the microwave; they are mainly responsible for the visible light emission of the plasma. The energized warm electrons (several kiloelectronvolts) are able to ionize atoms and ions and they are mainly responsible for the characteristic X-ray photons emitted by the plasma. Electrons having much higher energy than necessary for an effective ionization (10 keV or higher) are called hot electrons. Majority of them are lost in the walls of the plasma chamber, creating Bremsstrahlung X-ray photons. After a full simulation by TrapCAD, an energy filtering post process reveals these three main electron populations.

For these simulations, TrapCAD was run on an average personal computer. The geometrical, magnetic, and microwave parameters of the ATOMKI ECRIS were used as input. The initial electrons started from the resonance zone (closed equimagnetic surface where the ECR phenomena take place) with randomly equal spatial distribution. The initial energy of the electrons was a random value between 1 and 200 eV. Usually, 50-100 thousand electrons were started, and the typical real (plasma) time was between 10 and 30 ns, which corresponded to about 5-15-h CPU time.

Data post processing (energy filtering, ordering, and visualization) was performed by commercially available codes. Fig. 1 actually contains eight sub pictures in three lines. The left and middle pictures in top line are the cold and warm electron parts of the ECR plasma. For cold electron filtering, the upper energy limit was chosen below 200 eV, while the warm electron gap was 3-10 keV. The remarkable spatial difference between the two populations is well visible. The right picture in the top line shows the lost positions of the hot electrons (energy range: 10-100 keV) in the closed cylindrical plasma chamber walls. Those triangles are caused by electron-wall interactions where the electrons are guided by bunches of magnetic loss lines. In the middle line, the previous cold and warm electron components are visualized from the side direction in 3-D mode. The coupled microwave frequency at pictures in the top and middle lines was 14.5 GHz. The three pictures at the bottom line show the cases when single, double, and triple microwave injections were simulated, resulting in single, double, and triple resonance zones and plasmas. The injected microwave frequencies (from left to right; in gigahertz) were 8, 8 + 14.5, and 8 + 14.5 + 18.0. The double and triple frequency couplings at ECRISs are used to increase the energy content of the plasma with the final goal to produce very highly charged ions.

- [1] R. Rácz, S. Biri, J. Pálinkás, *IEEE Transactions on Plasma Science* **39** (2011) 2462-2463
- [2] S. Biri, E. Takács, R. Rácz, L. T. Hudson, J. Pálinkás, *IEEE Transactions on Plasma Science* **39** (2011) 2494-2495
- [3] S. Biri, R. Rácz, J. Imrek, A. Derzsi, Zs. Léczi, *IEEE Transactions on Plasma Science* **39** (2011) 2474-2475
- [4] E. Takács, S. Biri, A. Valek, J. Pálinkás, Cs. I. Szabó, L. T. Hudson, B. Juhász, T. Suta, J. Imrek, B. Radics, *Atomki Annual Report 2002 0* (2003) **37**
- [5] R. Rácz, S. Biri, J. Pálinkás, *Atomki Annual Report 2009 0* (2010) **48**
- [6] R. Rácz, S. Biri, J. Pálinkás, *Atomki Annual Report 2010 0* (2011) **54**

5.1 Stabilization of intermediate NiSi phase in NiPt/Si(001) and Ni/Pt/Si(001) nanodimensional film compositions

*Yu.N. Makogon^{a)}, G. Beddies^{b)}, D.L. Beke^{c)}, A. Csik, E.P. Pavlova^{a)}, S.I. Sidorenko^{a)},
T.I. Verbitska^{a)}*

Currently NiSi is the most favorable low-resistivity ($\rho_v \sim 10\mu\Omega\cdot\text{cm}$) interconnect material in semiconductor technology. The increase of the thermal stability of NiSi and prevention of transition of this phase to high-resistivity NiSi₂ is a topical problem of material science.

The goal of present study is to investigate the influence of Pt on the development of thermally activated solid state reactions and on the thermal stability of NiSi in [(Ni+x at.%Pt)30 nm]/Si(001) and Ni(30 nm)/Pt(2;6 nm)/Si_{epi}(50 nm)/Si(001) nanodimensional film compositions, where x=0.73; 3.35; 8.24; 19. The samples were produced by magnetron sputtering from mosaic target of NiPt with different content of Pt and also by layer-by-layer deposition of Ni and Pt on Si(001) substrate at room temperature. Annealing of samples were carried out in vacuum ($\sim 10^{-3}$ Pa) and in nitrogen atmosphere in the temperature range of 450-900 °C for 30 seconds. Solid state reactions were characterized by methods of X-ray diffraction, Secondary Neutral Mass Spectrometry (SNMS - SPECS, INA-X type), Transmission Electron Microscopy (TEM) and resistometry.

During annealing the thermally activated solid state reactions began by formation of intermeditated silicide phases. It is show that the presence of the intermediate Pt layer stabilizes the NiSi phase and hinders the formation of NiSi₂ phase. It is established that in samples, regardless of Pt concentration, during annealing in vacuum the solid state reaction begin at 450 °C with formation of intermediate NiSi and Ni₂Si phases. By the increasing of Pt content the NiSi→NiSi₂ transition shifts in side of

more high temperatures. During annealing of samples in nitrogen atmosphere at 450 °C only NiSi phase formation was observed. In samples with small Pt content (0.73; 3.35 at.%) the annealing at 700 °C is accompanied by start of phase transition of NiSi to Ni₂Si. In samples with large content of Pt (8.24; 19 at.%) the NiSi remains stable up to the temperature of 900 °C, which is in 150 °C higher than in samples of Ni(30 nm)/Si(001) without alloying of Pt. It is confirmed by the low value of electric resistance.

The presence of the Pt in the grain and interphase boundaries can explain the detection of small amount of the PtSi phase by XRD. On the other hand these can not be observed by TEM or SNMS. It was shown recently [1] that the diffusion intermixing in Co/Si systems started with fast (triple junctions/grain-boundary) diffusion of the Si into the Co layer. After some incubation time Si atoms appeared and enriched on the Co surface and acted as a reservoir for back-diffusion into the Co layer from the Co surface through the slower grain-boundaries. Thus, assuming similar Si diffusion mechanisms in Ni/Si system, formation of different Pt_xSi_y phase in the grain boundaries or at the interphase boundaries can take place and the Si enrichment at the free surface can also be explained.

a) National Technical University of Ukraine "KPI", Peremogy Avenue 37, Kiev, Ukraine

b) Institute of Physics, Chemnitz University of Technology, Reichenhainer Street 70, Germany

c) University of Debrecen, Department of Solid State Physics, H-4010 Debrecen, P.O. Box 2, Hungary

[1] A. Lakatos *et al.*, Vacuum **85**, 493 (2010).

5.2 Effect of pressure on photo-induced expansion of $\text{As}_{0.2}\text{Se}_{0.8}$ layer

S. Charnovych^{a)}, G. Erdélyi^{b)}, S. Kokenyesi^{a)}, A. Csik

Amorphous chalcogenide glasses are well known as materials where different kinds of structure-related transformations, like amorphisation-crystallization, volume and chemical stability changes take place under certain external influences (heat-, light-, and electric field) [1]. In spite of a rather long history of investigations and even some important applications in memory devices the mechanism of these effects is not completely clear, since besides the necessary condition of light interaction with glass and charge generation of the mass transport, shift or diffusion of atoms must occur. Unfortunately, we have only very little information about the light induced atomic transport processes in amorphous chalcogenides.

Recent investigations on light-induced expansion, and holographic recording in chalcogenide glasses show that $\text{As}_{0.2}\text{Se}_{0.8}$ composition reveals giant photo-expansion and photo-plasticity effects [2]. We selected this material for more detailed investigations of the direct relief formation process. In this work we investigate the influence of hydrostatic pressure on photo-stimulated surface relief formation in $\text{As}_{0.2}\text{Se}_{0.8}$ thin films.

1 μm thick layers were evaporated from bulk glassy materials. Silica glass plates were used as substrate for films. The thickness of the layers were measured with profilometer type Ambios XP-I. The samples were illuminated with red laser beam (633 nm, output power $P=7.5\text{mW}$) through a copper grid, which resulted to an imprint picture on the surface of the film with interference fringes at the edges. In this way surface relief with different heights were formed after the given exposure according to the distribution of light intensity. The measurements were carried out at room temperature in a large-volume (1 cm^3) optical cell having sapphire windows. The hydrostatic pressure was generated by means of a

3-stage gas compressor. We used profilometer as well as scanning electron- and atomic force-microscope for measurements of the surface changes due to the illumination.

It was shown that the surface relief growth in a non-homogeneously illuminated light sensitive $\text{As}_{0.2}\text{Se}_{0.8}$ layer suppressed essentially by the applied hydrostatic pressure. Measured data support the model of light-induced expansion, which includes formation of localized defects and appropriate free volume changes at the initial stage of exposure as well as the mass-transport at higher exposures, based on the motion of the created defects. Our results can be used in the complex model of induced surface modulations, which is under development now.

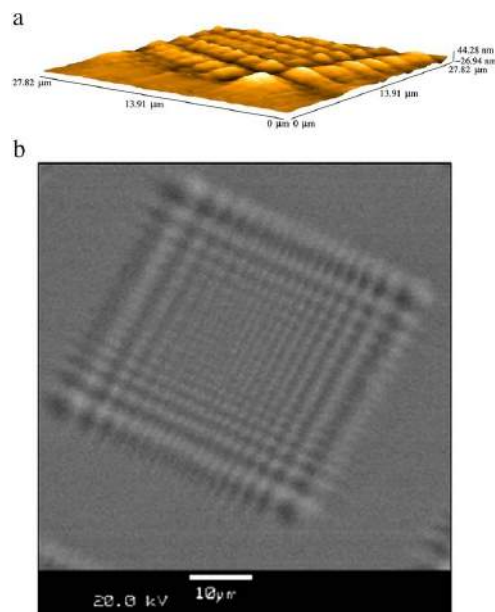


Figure 1. a) AFM picture of the surface pattern developed under illumination by the light diffracted on the grid mask. b) SEM picture of the matrix of surface relief structures.

a) Uni. Debrecen, Dept. of Exp. Phys.

b) Uni. Debrecen, Dept. of Solid State Phys.

[1] V. Kolobov, S.R. Elliott, *Adv. Phys.* 40 (1991) 625

[2] M.L. Trunov, *Non-Cryst. Solids* 355 (2009) 1993

5.3 Enhancement of photoinduced transformations in amorphous chalcogenide film via surface plasmon resonances

S. Charnovych^{a)}, S. Kokenyesi^{a)}, Gy. Glodán^{b)}, A. Csik

Different photo-induced effects like photo-darkening and bleaching, local expansion or contraction, changes of the reflectivity and refraction index take place in thin films of semiconductor chalcogenide glasses from As(Ge)-S(Se) systems [1]. These are essential for the development of amplitude-phase optical recording and memory devices, fabrication of photonic elements. Metals as Au, Ag and Cu are widely used for Surface Plasmon Resonance (SPR) experiments, not in the last place because of the manifestation of optical resonances in the visible spectral region [2]. The SPR appears due to the excitation of surface plasmons by light for planar metal surfaces at special matching conditions, while the localized surface plasmon resonance (LSPR) is rather easily observed in nanometer-sized metallic structures. The last are widely used for the development of ultrahigh-sensitive fluorescence measurements, semiconductor devices and even in optical data storage. Gold nanoparticles (GNP) on a silica glass substrate satisfied with the conditions for SPR in a green-red spectral range, where the selenide and sulphide glasses are the most sensitive. It is known that the increase of the size and the change of the shape of the metallic nanoparticles lead to the red shifts of the SPR. So the SPR wavelength can be varied this way and we used this opportunity in our experiments. Because of the localized electromagnetic field amplification near the nanoparticle the enhanced interaction of the exciting light with surrounding media occurs and electron-hole processes in it as well as the interatomic bonds and the structure in the whole can be more easily altered. We used this effect for the enhancement of photoinduced transformations and so of amplitude-phase optical recording based on the amorphous chalcogenide films made of glasses from As-Se system.

Experiments have been made on struc-

tures which contain appropriate plasmonic element and a chalcogenide layer suitable for optical measurements of photo-induced effects. Firstly, 30 nm thick gold layers were deposited on silica glass substrates. The obtained samples were annealed at 400, 500 and 600 °C for 1 h. As a result of this process separated non-spherical GNP were observed with different sizes (60 nm at 400 °C, 75 nm at 500 °C and 90 nm at 600 °C) that caused the shift of the plasmon resonance wavelength. Further a thin, 500-700 nm thick chalcogenide layer (As₂Se₃ or As₂₀Se₈₀) has been deposited on the GNP by thermal evaporation technique. The investigated structures have been irradiated by red ($\lambda=633$ nm, output power P=7 mW) laser beam through a diaphragm with 1.2 mm diameter. The layer thickness and its changes have been measured by Ambios XP-I profilometer. Optical transmission spectrum has been used for calculations of the refractive index.

Optical darkening, changes of the refractive indexes and the absorption coefficient, as well as the red shift of the fundamental absorption edge have been observed at the initial stage of the illumination in samples. We can conclude that the presence of plasmon fields enhances the photo-induced transformations in amorphous chalcogenide films. The investigated effect of enhanced structural transformations can be used for direct recording of holographic gratings, waveguides and other elements of integrated optics, made of chalcogenide glasses.

a) Uni. Debrecen, Dept. of Exp. Phys.

b) Uni. Debrecen, Dept. of Solid State Phys.

[1] K. Shimakawa, A. Kolobov and S.R. Elliott, *Adv. Phys.* **44**, 475 (1995).

[2] R.B.M. Schasfoort and A.J. Tudos, *Handbook of Surface Plasmon Resonance*, RSC Publishing, Cambridge (1998).

5.4 Heat treatment induced structural modification of boron-doped ZnO layers

R. Lovics, A. Csik, V. Takáts, J. Hakl, K. Vad

In the case of solar cells, to optimize the properties of photovoltaic (PV) modules one of the important issues is the diffusion of sodium from the glass substrate into the layered structure. There are many discussions about the role of the Na during preparation of PV modules: i) selenisation of Mo interlayer between the ZnO and active layers to obtain a lower series electrical resistance without changing the transmittance of the ZnO layer [1]; ii) the diffusion of Na from glass substrate to a-Si:H/c-Si or Cu(In,Ga)Se₂ (CIGS) layer [2]. In certain cases the ZnO layers must be annealed in air or in hydrogen atmosphere to improve electrical conductivity. At the same time, the annealing temperature induces diffusion of Na. Thus, detailed investigation of appropriate layered materials is required.

Present work was initiated in the framework of developing the solar cell technology. The goal was to investigate suitable substrates appropriate for desirable Na diffusion. Boron-doped ZnO layers were prepared by Low Pressure Chemical Vapour Deposition (LPCVD) method on three different types of substrate: soda-lime windows glass (*s1*) and Schott AF-45 alkali-free thin glass (*s2*) were selected for our experiments. Polished Si substrate (*s3*) was used as a reference sample. After sample preparation procedure, the samples were annealed in air at 300°C. As it can be seen in Fig.1, significant structural changes occurred at the surface of boron-doped ZnO layers in the form of bubble formation. We experienced that Na diffusion directly connected with hydrogen precipitation. Formation of bubbles observed was most probably due to enhanced hydrogen accumulation from the ZnO:B structure or decomposition of physisorbed precursor. After the annealing, the bubbles on the sample surface were blown up and cracked, i.e. were de-

stroyed on polished Si and Soda-lime glass substrates. However, the samples prepared on AF 45 Schott alkali-free thin glass substrate had visually much less bubbles originated from the ZnO film.

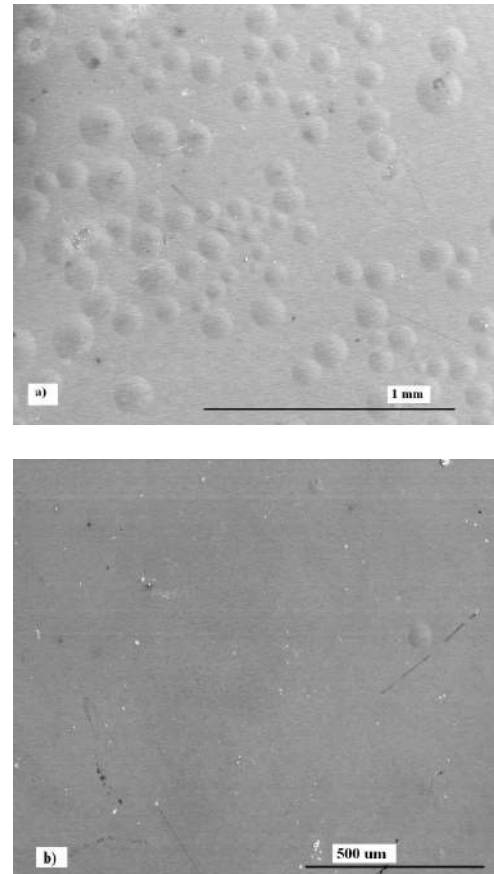


Figure 1. SEM image of ZnO:B sample prepared on Soda-lime glass for windows (a) and AF 45 Schott alkali free thin glass (b) substrates after 1440 minutes annealing.

Acknowledgements

This work was supported by the National Office for Research and Technology (Grant nos. OTKA 73424 and TFSOLAR2).

- [1] P.J. Rostan, *Thin Solid Films* 480-481 (2005) 67
- [2] R. Kaigawa, *Thin Solid Films* 519 (2011) 5535

5.5 Determination of chemical state of Al doping element in ZnO layer

A. Csik, J. Tóth, Z. Lábadi^{a)}, R. Lovics, V. Takáts, J. Hakl, K. Vad

Transparent and conducting oxides (TCO) thin films are very important from the scientific and technological point of view. The co-existence of electrical conductivity and optical transparency in these materials makes it possible to use them in modern technologies: transparent electrodes for flat panel displays and photovoltaic cells, low emissivity windows, transparent thin films transistors, light emitting diodes. One of the important TCO semiconductors is the impurity-doped zinc-oxide (ZnO) layer, for example aluminium doped zinc-oxide layer (AZO), due to its unique physical and chemical properties. It has wide band gap (3.44 eV) and large exciton binding energy (60 meV). ZnO thin layers have a great interest for potential applications in optical and optoelectronic devices [1]. Furthermore, high quality single crystal ZnO wafers has already been available as a result of new developments in ZnO growth technologies with the capability to scale up wafer size, which is an important factor for increasing efficiency of solar cells. Nonetheless, in order to enable the use of ZnO layers with enhanced electrical properties, higher conductivities can be obtained by doping with donor elements such as aluminium, gallium, indium, boron or fluorine [2]. Investigation of p-type doping possibilities, diffusion processes and thermal stability of these layers are in the focus of interest in the interpretation of their optical and electrical properties, and the prediction of their lifetime.

In our SNMS/SIMS-XPS laboratory, experiments on TCO layered structures were carried on. Depth profile and chemical state analyses of ZnO/AIO/ZnO layered structures were performed by Secondary Neutral Mass Spectrometry (SNMS) and X-ray photoelectron spectroscopy (XPS). The samples were produced by atomic layer deposition technique with the following layered structure: between a few hundred atomic layers of ZnO was an AlO atomic layer. The SNMS was used for depth profiling of these layered structures. Af-

ter determination of the depth of the embedded AlO layer with the precision of 1 nm, we sputtered the upper ZnO atomic layers until the AlO layer was revealed and determined the chemical state of Al in the thin AlO layer by the XPS instrument. During the whole experiment the samples were in high vacuum so as to exclude the contamination of the surface.

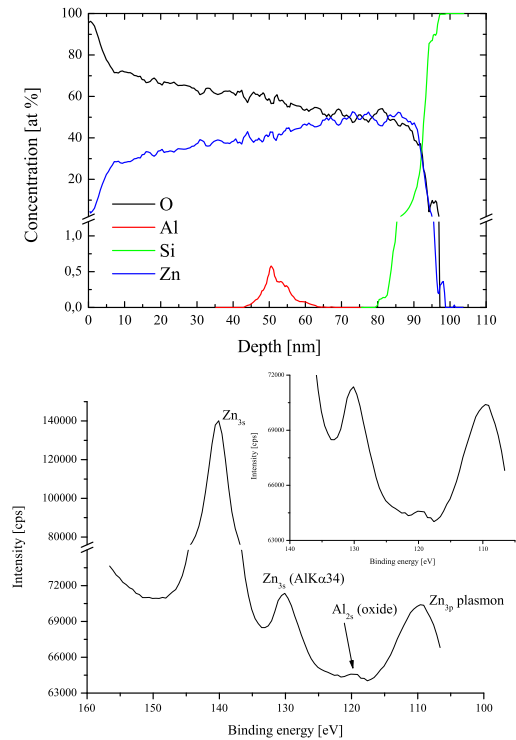


Figure 1. SNMS depth profile of ZnO layer and chemical state of Al measured by XPS method.

Acknowledgements

This work was supported by the National Office for Research and Technology (Grant nos. OTKA 73424 and TFSOLAR2).

- a) Hungarian Academy of Sciences, Research Centre for Natural Sciences, MTA TTK, P.O. Box 49, 1525 Budapest, Hungary
- [1] U. Ozgur *et al.*, J. Appl. Phys. **98**, 041301 (2005).
- [2] K. Ellmer, A. Klein and B. Rech, Transparent Conductive Zinc Oxide. Basics and Applications in Thin Film Solar Cells, Springer, 2008.

5.6 Scanning transmission ion microscopy of polycarbonate nanocapillaries

G.A.B. Gál, I. Rajta, S.Z. Szilasi, Z. Juhász, S. Biri, Cs. Cserhádi^a), A. Csik, B. Sulik

Nanochanneled materials are of a great interest due to their peculiar properties and high potential impact for the fabrication of nanostructures and nanodevices. Polycarbonate membranes are produced by heavy ion irradiation followed by chemical etching of the ion tracks. The irradiation parameters determine the porosity (areal density of the capillaries) and angular spread, while the channel diameters and shapes depend on the chemical process parameters. Such polycarbonate (and other materials) membranes are commercially available from a few manufacturers. The primary use of the filters involves packaging and filtering applications. Moreover, they are used for collecting atmospheric aerosols for environmental research.

The nanocapillaries formed in membranes are particularly suitable for ion and electron guiding studies of a recently discovered, but not yet completely understood capillary guiding phenomenon [1]. This interesting guiding effect is very promising for patterning by parallel writing with ions and/or electrons through masks.

In order to get a better understanding of this phenomenon, we need a better characterization of the capillaries themselves.

This study [2] is addressing the angular distribution of the nanochannels in the polycarbonate filters by using a nuclear microprobe facility and the method of scanning transmission ion microscopy (STIM) [3].

The STIM experiments in this work have been performed at ATOMKI. The proton energy was 2 MeV, the beam intensity was about 1000 protons s^{-1} , the beam spot size was about $1 \times 1 \mu\text{m}$, the scan size was $100 \times 100 \mu\text{m}$ and the beam divergence was smaller than 0.07° .

A scanning electron microscope (SEM, Hi-

tachi S4300 CFE) was used to measure the capillary diameters and the membrane porosity. The sample thickness was determined by a profilometer (AMBIOS XP-I).

We have investigated two different pieces of Millipore IsoporeTM samples. A typical SEM image showed several overlapping holes, while the sample porosity is not as high as it would be characteristic for ordered arrays of capillaries.

The angular width of the transparency has been determined by the STIM method. The investigated membranes have shown a larger angular range for ion transmission than it could be expected by their geometrical parameters. This indicates that there is a significant angular spread in the direction of the capillary axes. This method can be useful to provide feedback for improving the ion irradiation process if it is necessary to produce arrays of properly aligned, parallel capillaries.

If such samples are intended to be used for ion guiding studies, where high parallelism are required, these types of STIM measurements are always advantageous as input information for the sample characteristics. For the conventional application areas of these samples (filtering) such information are more or less irrelevant.

Acknowledgements

The support of EU co-funded Economic Competitiveness Operative Programme (GVOP-3.2.1.-2004-04-0402/3.0) as well as from the Hungarian Scientific Research Fund (OTKA) under contracts K83886 and CK84225 is gratefully acknowledged.

a) Dept. of Solid State Physics, Uni. Debrecen, Hungary

[1] N. Stolterfoht, *et. al*, PRL 88 (2002) 133201

[2] G.A.B. Gál, *et. al*, NIMB 269 (2011) 2322

[3] M.B.H. Breese, *et. al*, NIMB 64 (1992) 505

5.7 Compaction of PDMS due to proton beam irradiation

S.Z. Szilasi, J. Kokavecz^{a)}, R. Huszánk, I. Rajta

This work is about the detailed investigation of the changes of the surface topography, the degree of compaction/shrinkage and its relation to the irradiation fluence and the structure spacing in *poly(dimethylsiloxane)* (PDMS) patterned with 2 MeV proton microbeam [1].

Sylgard 184 kit (Dow-Corning) was used to create the PDMS samples. The density of the PDMS samples was determined with pycnometer. The penetration depth for 2 MeV protons is $\sim 85 \mu\text{m}$, the PDMS layer was $\sim 95 \mu\text{m}$ thick, so the incident protons stop in the PDMS, they do not reach the substrate. The irradiations have been performed at the nuclear microprobe facility at ATOMKI. The irradiated periodic structures consisted of parallel lines with different widths and spacing. To achieve different degrees of compaction, each structure was irradiated with five different fluences. The surface topography, the phase modification of the surface, and the connection between them were revealed using an atomic force microscope (AFM PSIA XE 100).

The shrinkage data were obtained from the topography images. The structures with different line widths and spacing show different degrees of compaction as a function of irradiation fluence. By plotting them in the same graph (Fig. 1) it is clearly seen that the degree of compaction depends on both the irradiation fluence and the distance of the structures.

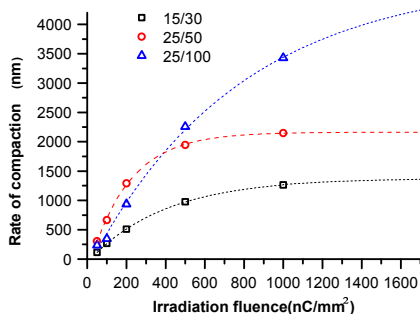


Figure 1. The degree of compaction as a function of the irradiation fluence in cases of different line widths/spacing. The lines show the fitted $y = a - bc^x$ asymptotic function for each dataset.

The fluence dependence of the compaction can be explained with the chemical changes of PDMS. When an energetic ion penetrates through the material it scissions the polymer chain, whereupon among other things volatile products form. In the case of PDMS, these are mainly hydrogen, methane and ethane gases that can be released from PDMS. The irradiated volume shrinks due to significant structural change during which silicate derivatives (SiO_x) are formed.

The phase change and the corresponding surface topography was compared and studied at all applied irradiation fluences. It was concluded that at low fluences the surface topography does not follow the phase change that corresponds to the irradiation pattern. At higher fluences the surface topography follows the irradiation pattern, i.e. the phase change, quite well but not perfectly. The irradiated regions are compacted significantly but their bottom is not flat. Between the irradiated regions, the unirradiated areas show a regular curved surface. This can be explained with the developed stress caused by compaction due to irradiation. During irradiation the irradiated areas start to shrink while the unirradiated areas try to remain unchanged. The topographical transition between the two phases is not a step function, but it is continuous due to the rubbery nature of PDMS.

The PBW technique, that utilizes a focused MeV ion beam, is capable of the production of devices in PDMS, which have curved-edge relatively shallow, a couple of microns deep, structures on the surface. The curvature of the surface and the degree of compaction can be adjusted with the applied ion fluence and with the distance of the structures. By choosing the proper irradiation parameters short or even long range symmetrical surface curvatures can be achieved.

a) Department of Optics and Quantum Electronics, University of Szeged, Hungary

[1] S.Z. Szilasi, *et. al.*, Appl. Surf. Sci. 257 (2011) 4612

5.8 Chemical changes in PMMA as a function of depth due to proton beam irradiation

S.Z. Szilasi, R. Huszánk, D. Szikra^{a)}, T. Váczi^{b)}, I. Rajta I. Nagy^{c)}

In this work we investigated the depth profile of the chemical changes in *poly(methyl methacrylate)* (PMMA) due to 2 MeV proton irradiation [1]. The measurements were carried out on 10 μm thin stacked foil samples using an infrared spectrometer in universal attenuated total reflectance (UATR) and transmission modes; while the thick samples were analyzed with a confocal micro-Raman spectrometer.

The IR results showed that the amount of all of the functional groups decreases as a function of depth, corresponding to the energy loss of the incident protons. At the low LET part of the ions trajectory (close to the surface) less change occurs. The region of the maximal change is localized at about 70-80 μm depth from the surface, which is in good agreement with the position of the place of the maximal energy loss. In the IR spectra no new bands appeared at the applied fluence indicating that only chain scissioning prevails during irradiation. The surface ATR technique was complemented with transmission measurements that confirmed the ATR results and revealed the depth dependence of the shrinkage as well.

Micro-Raman measurements (e.g. Fig. 1) showed the strong dependence of the degree of modification on the energy transfer from the decelerating protons. Depth profiles reveal that at the fluences applied in this work the entire irradiated volume suffered some chemical modifications, but in the case of low-fluence samples the zone of maximal modification (i.e., the saturation of radiation-induced chemical changes) is restricted only to the Bragg peak. As the fluence increases, the region of maximal modification also extends towards the sample surface, reaching it at about 6.25×10^{14} ions/cm² (1000 nC/mm²) delivered fluence. The quality of the occurred chemical processes does not change, but the yield of chain scissioning changes as a function of depth, following the energy dissipation (the Bragg curve) of

decelerating protons. The degree of chemical alteration is limited by the saturation level of radiation-induced chemical changes, i.e. where certain bonds are all destroyed, or broken and newly formed bonds are in equilibrium.

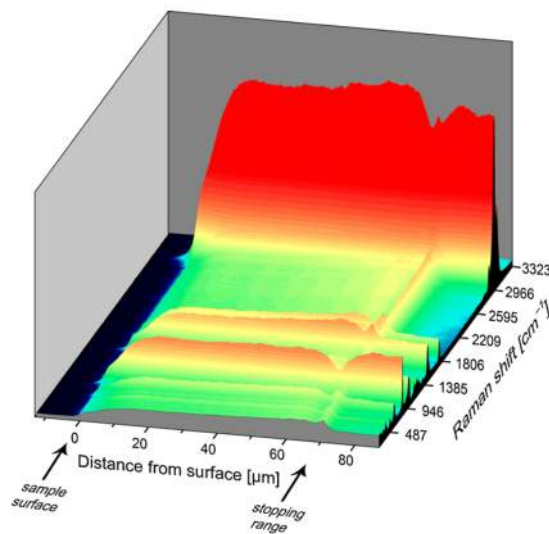


Figure 1. Surface plot of a Raman line scan (250 spectra) along the irradiation direction (1.25×10^{14} ions/cm² fluence, 200 nC/mm²). The dark band on the left is outside the PMMA block. The pronounced rise in background intensity below 70 μm corresponds to the Bragg peak. On the right is unirradiated PMMA.

C-C bonds were found to be slightly more radiation-sensitive than C-H and C=O bonds. Under the fluences applied in this study, a radiation-induced peak was found at 1635 cm⁻¹ that increases with increasing LET.

a) University of Debrecen, Institute of Nuclear Medicine, H-4032 Debrecen, Nagyerdei krt. 98, Hungary

b) Institute for Nanotechnology, Bay Zoltán Foundation for Applied Research, H-3515 Miskolc-Egyetemváros, P.O. Box 46, Hungary

c) Department of Physical Chemistry, University of Debrecen, P.O. Box 7, H-4010 Debrecen, Hungary

[1] S.Z. Szilasi, *et. al.*, *Mat. Chem. and Phys.* 130 (2011) 702

[2] S.Z. Szilasi, *et. al.*, *Appl. Surf. Sci.* 257 (2011) 4612

5.9 The use of electron scattering for studying atomic momentum distributions: the case of graphite and diamond

M. Vos^{a)}, R. Moreh^{b)} and K. Tórkési

The momentum distributions of C atoms in polycrystalline diamond (produced by chemical vapor deposition) and in highly oriented pyrolytic graphite (HOPG) were studied by scattering of 40 keV electrons at 135° [1]. By measuring the Doppler broadening of the energy of the elastically scattered electrons, we resolved a Compton profile of the motion of the C atoms. The aim of the present work was to resolve long-standing disagreements between the calculated kinetic energies of carbon atoms in HOPG and in diamond films and the measured ones, obtained both by neutron Compton scattering (NCS) and by nuclear resonance photon scattering (NRPS).

We have shown that electron scattering can be used to obtain information about the kinetic energies of atoms in solids. The values obtained by electron scattering are (after correction for multiple scattering and isotope effects) within 3%- 6% with the most recent neutron results for HOPG [2]. There is good agreement between our angular averaged results and the calculations of Nicklow et al., [3] and somewhat larger ($\approx 6\%$) than the calculated values of Young and Koppel [4] and Al-Jishi and Dresselhaus [5]. There is still a sizable difference in the anisotropy as calculated ($T_p/T_c = 1.45$) (Ref. 4) and as measured here ($T_p/T_c = 1.88$) or as measured by the most recent neutron experiment ($T_p/T_c = 1.93$) [2] (T_p and T_c refer here to the effective temperatures along and normal to the graphite planes.)

The present value is also within 6% with the calculated value for diamond. This spread is small compared to that of the earlier NCS measurements and the results of the NRPS method. The deviation is, however, still larger than the statistical uncertainty which is somewhat surprising as the calculations are

straightforward, and the experimental techniques rather direct.

Finally, it should be emphasized that the ECS technique requires relatively modest hardware. Increasing its energy resolution (and hence its ability to measure the momentum distribution of, in particular, heavier elements) is a very realistic possibility. This contrasts with the photon and neutron techniques that rely on the sharpness of resonances of suitable isotopes. Electron scattering is somewhat surface sensitive (probing depth about 30 nm for 40 keV electrons in carbon) compared to the other techniques, but this is very bulk sensitive by surface science standards. This means that some influence of surface effects could affect its result, but also opens up the possibility of studying momentum distributions in thin films.

Acknowledgements

We would like to thank Dr. J. E. Butler from the Naval Research Center in Washington DC for the CVD diamond sample used in the ECS measurements and Professor Weigold for critically reading the manuscript. This work is made possible by a grant of the Australian Research Council.

- a) Atomic and Molecular Physics Laboratories, Research School of Physics and Engineering, Australian National University, Canberra, Australian Capital Territory 0200, Australia
- b) Physics Department, Ben-Gurion University of the Negev, Beer-Sheva 84105, Israel
- [1] M. Vos, R. Moreh, K. Tórkési, *J. of Chem. Phys.* **135** 024504 (2011).
- [2] A.L. Fielding, D.N. Timms, and J. Mayers, *Europhys. Lett.* **44**, 255 (1998).
- [3] R. Nicklow, N. Wakabayashi, and H.G. Smith, *Phys. Rev. B* **5**, 4951 (1972).
- [4] J.A. Young and J.U. Koppel, *J. Chem. Phys.* **42**, 357 (1965).
- [5] R. Al-Jishi and G. Dresselhaus, *Phys. Rev. B* **26**, 4514 (1982).

5.10 Interpretation of eRBS for H quantification at surfaces

R. Álvarez^{a)}, K. Tőkési and F. Yubero^{a)}

The quantification of H at the surface is a subject of key importance. However, direct quantification of this element at the surface region (<2-3 nm) is not an easy task. Note for example that H does not show photoemission peaks in standard surface analysis by XPS. An indirect way to quantify it is by means of High Resolution Electron Energy Loss Spectroscopy, but only those H atoms participating in the vibrational absorption spectra would be observed. It is also possible H quantification with surface sensitivity by means of Nuclear Reaction Analysis, but this technique is not easily available.

Recently it has been proposed a method (Electron Backscattering spectroscopy, eRBS) to quantify the H content at the surface of a-C:H samples based in the analysis of elastically backreflected electrons with primary energies about 1500 eV [1,2]. It is based on the fact that the recoil energy of the incident electrons depends on the atomic mass of the atoms located at the surface that act as scatter centres. Fairly consistent analysis were found for a-C:H

materials and polymer surfaces [1,2]. This new strategy of analysis has also been use to distinguish between H and deuterium at the surface of ice water [3].

We have shown that the presence of Hydrogen at surfaces can be detected by standard electron spectroscopy, i.e. the eRBS complements XPS for elemental surface studies [4]. We demonstrated that the Monte Carlo simulations help to understand/visualize capabilities of this technique The naive single Rutherford scattering description of the problem is quantitatively valid but interpretation of intensity of H and C peaks in CH₂ samples have to be made with care.

a) ICMSE Sevilla, E-41092 Sevilla, Spain, EU

- [1] F. Yubero et al., Applied Physics Letters 87, 084101 (1-3) (2005)
- [2] V.J. Rico et al., Diamond and Related Materials 16, 107-111 (2007)
- [3] F. Yubero, K. Tokési, Applied Physics Letters 95, 084101 (3) (2009)
- [4] R. Álvarez, K. Tőkési, and F. Yubero, Invited talk presented at ECASIA 14th, Cardiff, UK, September 4-9, 2011.

5.11 Test of image acceleration by distant collision of proton microbeam

K. Tőkési, I. Rajta and R.J. Berezsky

The clear experimental investigation of image acceleration is a very challenging task when using ions and planar surfaces since the ion is always attracted towards the surface by its self-image potential, and will always undergo a close collision with the surface. This problem, however, can be avoided using a capillary target. This technique was introduced as an alternative way to study above-surface processes [1]. Ions traveling approximately parallel to the capillary axis also experience an image force towards the cylindrically shaped wall of the capillary, but only a small fraction of these ions will collide with the wall, while most of the ions can escape from the capillary without hitting the wall. Moreover, by measuring the charge state of the transmitted particles additional information about the image acceleration can be gained.

In the present work, for the sake of simplicity, we used single metallic capillary as target and a well focused proton microbeam as projectile. In our measurements a steel capillary with a radius of 0.28 mm and length of $L_c=10$ mm was used. We performed the measurements with a 1 MeV proton beam. The beam spot size was $1 \mu\text{m}$, with beam current of ~ 1000 proton/s, and the angle of the beam divergence was less than 0.07° .

The combination of capillary target with the proton microbeam allows us to investigate distance-dependent features of the image acceleration. The capillary axis, at the beginning of the measurement, was aligned to the direction of the proton microbeam (capillary displacement of 0, see Fig.1.). The capillary was fixed to a moveable target holder, and the capillary was moved in the perpendicular direction with respect to the beam. The capillary axis was always parallel with the beam axis. The schematic diagram of the measurements can be seen in the inset of Fig. 1. We measured the beam deflection at $L_s=103$ mm from the entrance of the capillary as a function of the

capillary displacement with respect to the geometrical axis of the capillary. We found that the 1 MeV proton beam suffered a significant deflection due to the pure image acceleration [2]. In the next step we plan to measure the energy distribution of the transmitted particles. The investigation of the correlation pattern of beam deflection and the energy loss may offer us the ability to study the dielectric properties of the capillary material [3,4].

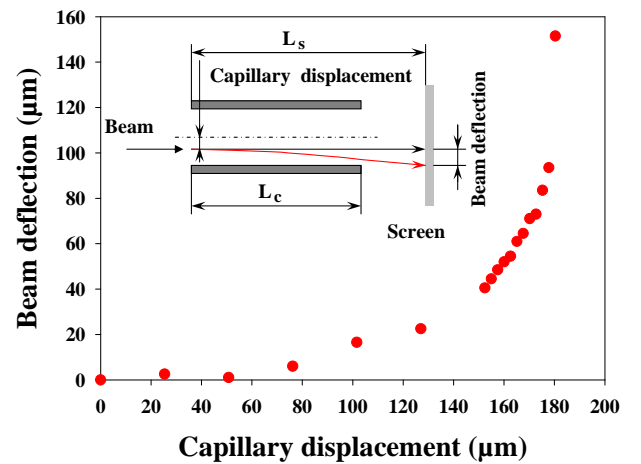


Figure 1. The beam deflection as a function of the capillary displacement with respect to the geometrical axis of the capillary. A schematic diagram of the measurement setup used is shown in the inset.

Acknowledgements

This work was supported by the Hungarian Scientific Research Fund OTKA No. K72172.

- [1] S. Ninomiya, Y. Yamazaki, F. Koike, H. Masuda, T. Azuma, K. Komaki, K. Kuroki, M. Sekiguchi, *Phys. Rev. Lett.* **78** (1997) 4557.
- [2] K. Tőkési, I. Rajta, and R.J. Berezsky, Conference program and abstracts of the 27th International Conference on Photonic, Electronic and Atomic Collisions (XXVII ICPEAC), 27 July - 2 August 2011 Queen's University Belfast, UK, Edited by Ian Williams, Gleb Gribakin and Hugo van der Hart, CD, Mo015
- [3] K. Tőkési, and J. Burgdörfer, *Surface Science* **454-456** (2000) 1038.
- [4] K. Tőkési, X.-M. Tong, C. Lemell and J. Burgdörfer, *Phys. Rev. A* **72** (2005) 022901.

5.12 Charging dynamics in electron transmission through Al₂O₃ capillaries

A.R. Milosavljevic^{a)}, K. Schiessl^{b)}, C. Lemell^{b)}, K. Tókési, M. Mátéfi-Tempfli^{c)}, S. Mátéfi-Tempfli^{c)}, B.P. Marinkovic^{a)} and J. Burgdörfer^{b)}

Shortly after the discovery of the unexpected effect of charged particle guiding many research groups joined to this field of research and carried out various experiments with insulator nano- and with conical shaped capillaries using highly charged heavy ions (HCI). The experiments with insulating capillaries showed not only directional guiding of the ions, but also the remarkable fact that the ions keep their initial charge state as a consequence of a self-organized charge-up inside the capillary. Ion guiding through the capillary ensues as soon as a dynamical equilibrium of self-organized charge-up by the ion beam, charge relaxation and reflection is established.

The intuitive explanation in terms of charging of the inner wall of the capillary followed by projectile deflection by the Coulomb mirror without close interaction with the capillary wall was quantitatively verified by a microscopic simulation invoking a diffusion model for charges deposited on the inner capillary wall after ion impact self-consistently coupled to the determination of projectile trajectories in the Coulomb field of the charged capillary material.

However, when using electrons instead of HCI, this simple explanation fail for several reasons: a) a dominant fraction of electrons escaping the trajectory have energies smaller than the incident energy E_0 in clear contrast to the picture of (almost) loss-free reflection at large distances above the surface, b) electrons do not change their charge state and thus a clear distinction between transmission of the original projectiles (primaries) and emission of electrons set free upon impact of primaries on the capillary wall (secondaries) does not exist. Furthermore, secondary electron produc-

tion also implies that surfaces can be, dependent on energy and angle of the primaries, positively charged (secondary electron emission (SEE) coefficient larger than 1) thereby attracting rather than deflecting subsequently arriving electrons.

In this work we have presented the transmission measurements of low-energy ($E = 250$ eV) electrons through insulating Al₂O₃ nanocapillaries [1]. We found that transmission at the incident energy is quickly suppressed with increasing tilt angle of the capillary axis relative to the incoming electron beam while inelastic transmission becomes more important. For small angles of incidence charging dynamics lead to a decrease of total transmission (elastic and inelastic) with time. Our results are interpreted on the basis of a microscopic model for the electron transport within the capillary including also close interactions with the capillary wall.

Acknowledgements

The work was supported by the Ministry of Education and Science of Republic of Serbia (Project No. 171020) and the Austrian Fonds zur Förderung der wissenschaftlichen Forschung under Grants No. FWF-SFB016 ADLIS, No. 17449, No. 17359, and the TeT Grant No. AT-7/2007. The work was also motivated by COST project ECCL.

a) Institute of Physics, University of Belgrade, Pregrevica 118, 11080 Belgrade, Serbia

b) Inst. for Theoretical Physics, Vienna University of Technology, Vienna, Austria

c) Facultés Universitaires Notre-Dame de la Paix, Department of Physics, Rue de Bruxelles 61, B-5000 Namur, Belgium

[1] A.R. Milosavljevic, K. Schiessl, C. Lemell, K. Tókési, M. Mátéfi-Tempfli, S. Mátéfi-Tempfli, B.P. Marinkovic, and J. Burgdörfer, Nucl. Instr. and Meth. Phys. (2012) in press.

5.13 Ultrathin tellurium nanowires in polymer assisted solution-phase process

Z. Gácsi, M. Hunyadi, S. Charnovych^{a)}, L. Csige, A. Csik, L. Daróczy^{b)}, M. Kis-Varga, T. Papp, Z. Szűcs, J. Tóth

The availability of ultrathin ($d < 10\text{nm}$) and monodisperse ($\Delta d/d < 10\%$) 1D tellurium nanostructures is of great scientific and technological importance due to the tunability of their optoelectronic characteristics as a direct consequence of quantum size effects. 1D nanostructures of Te and its composites have a high potential for future applications in integrated nanodevices exploiting their unique electronic properties and non-linear optical behaviour.

In the present work a facile hydrothermal route was employed to synthesize Te nanowires at 80-180 °C, with the assistance of water-soluble polymer poly-vinyl-pyrrolidone (PVP). The choice of PVP, as a well-known structure directing and stabilizing agent, and the optimization of parameters of the nanoparticle synthesis were essential to precisely control the quality, size, and morphology of the nanowires. The synthesis was based on redox reaction using aqueous solution of tellurite salt and hydrazine as the reducing agent:



The major steps of the synthesis are similar to those described in Refs. [1,2]. A teflon-lined stainless steel reaction vessel, an autoclave, was designed and constructed. The solution during the synthesis quickly turned brownish then gradually deep blue, indicating the formation of ultrathin nanowires, in contrast to larger ($d > 20\text{nm}$) Te nanocrystals, which tend to appear in grey. The resulted suspension was centrifuged and washed several times to prepare samples for subsequent analysis. The morphological characterization of Te nanowires was first carried out using transmission electron microscope (Fig. 1). The centroids of particle size distributions (PSD) were found between 4-10 nm with an average dispersion of about 10%. The typical length of the nanowires was in the range of 1-10 μm . The PSD could be controlled by the adjustment of reaction parameters.

The crystallographic characterization of the samples was based on the analysis of

high-resolution TEM images (Fig. 1b), X-ray diffraction (XRD) and optical absorbance measurements (Fig. 2). The absorption maximum around 560 nm corresponds to the observed deep blue colour of the nanowire suspension. The chemical structure of Te nanowires was inspected by measuring the electron loss spectra using the ESA31 spectrometer of Atomki. A systematic evaluation of the optical measurements is in progress [3].

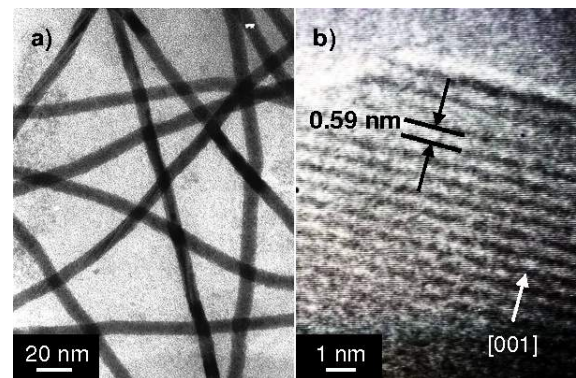


Figure 1. TEM images; (a) Te nanowires; (b) high-resolution section of a Te nanocrystal.

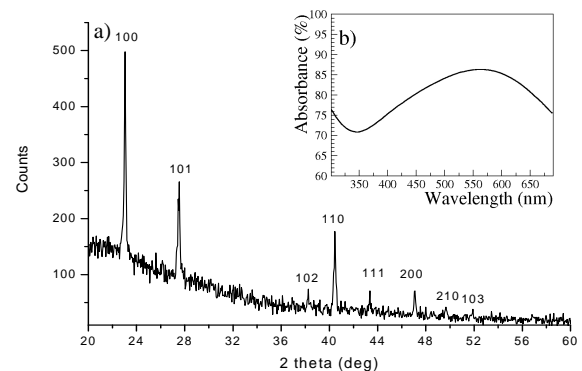


Figure 2. (a) XRD diffractogram and (b) optical absorbance spectrum of Te nanocrystals.

a) Dept. of Exp. Phys., Uni. Debrecen

b) Dep. of Solid State Phys., Uni. Debrecen

[1] H.-S. Qian et al., *Langmuir* 22 (2006) 3830

[2] H. Zhu et al., *J. Phys. Chem.* 115 (2011) 6375-6380

[3] M. Hunyadi et al., *Atomki Ann. Rep.* (2011)

5.14 Nucleation and growth dynamics of ultrathin tellurium nanowires

M. Hunyadi, Z. Gácsi, S. Charnovych^{a)}, A. Csik, S. Kökényesi^{a)}

One-dimensional nanostructures, e.g. nano-wires (NW) are currently in the focus of both research and development, due to their potential use in electronics, photonics, sensing, catalysis and nanoscaled biomedical applications as functional components of integrated nano-devices in the future. Trigonal tellurium (t-Te) with a highly anisotropic crystal structure, is an exceptional direct band-gap semiconductor for studying 1D nanostructures, which exhibits unique photoelectronic properties [1], and can easily be synthesized in simple, template-free solution-phase processes under moderate hydrothermal conditions [2].

The primary goal of recent developments is to achieve a sensitive control over the structural and electronic properties of the nanowires, which can be tuned by the shape control of the t-Te NW due to the quantum-size confinement. Therefore it is highly desired to understand their nucleation and growth dynamics and use this knowledge to engineer the product for specific applications.

We have performed a detailed study on the time evolution of the absorption maximum of t-Te NWs around 600 nm to gain a deeper insight into the formation of partially amorphous nuclei and the growth process of crystalline nanowires. The absorption maximum is attributed to the VB3-CB1 excitation, which sensitively depends on the particle size distribution (PSD).



Figure 1. (top) Cuvette heater; (bottom) photographs demonstrating the optical density change of the synthesis batch (time span: 0-45 min).

The optical spectra were measured during the course of the synthesis. To facilitate a time-scanned measurement, we designed and constructed a regulated cuvette-heater equipment (Fig. 1.), which was used in conjunction with the spectrophotometer Shimadzu UV-3600. The aqueous suspensions of t-Te nanowires were prepared at various parameters of the synthesis, such as the concentration and polymerization degree of the capping agent polymer PVP (poly-N-vinyl-pyrrolidone), temperature, pH and reactants. Selected results of the preliminary analysis are plotted in Figs. 2. The evolution of the optical characteristics of the t-Te nanowires were interpreted by numerical calculations based on the classical Gibbs nucleation theories and general population balance model [3].

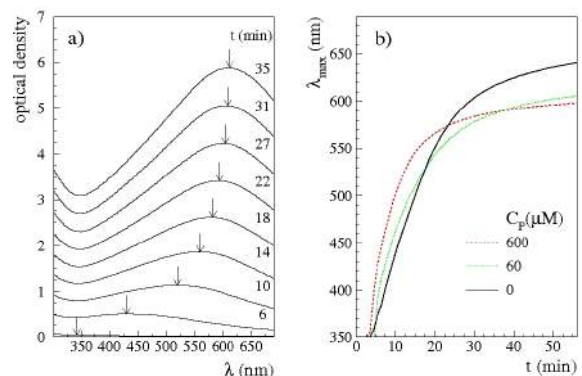


Figure 2. (a) Absorption spectra recorded as a function of synthesis time; (b) time evolution of absorption maxima under different polymer concentrations (CP).

a) Dept. of Exp. Phys., Uni. Debrecen

[1] P. Ghosh, et al., Phys. Rev. B 75 (2007)

[2] Z. Gácsi et al., Atomki Ann. Rep. (2011)

[3] R. Xie, et al., J. Am. Chem. Soc. 131 (2009) 15457-15466; J. van Embden, et al., J. Phys. Chem. C 113, (2009) 16342-16355; (see references therein)

5.15 Iron ion implantation into C⁶⁰ layer

R. Rácz, S. Biri, A. Csik, K. Vad

The soccer ball shaped carbon molecule consisting of 60 carbon atoms (C⁶⁰, fullerene) was discovered in 1985. Since that time the fullerene has become intensively studied. This special molecule has much potential in medical care, biotechnology and nanotechnology. We are motivated to produce special type fullerenes, so called endohedral fullerenes (some alien atoms are encapsulated inside the fullerene cage). The spring of our motivation is that the Fe@C⁶⁰ could be applied as a contrast material for MRI (Magnetic Resonance Imaging) or microwave heat therapy.

One way to make X@C⁶⁰ is the surface production using an ECRIS (Electron Cyclotron Resonance Ion Source). An evaporated or pre-prepared fullerene layer is irradiated by ions to form a new material during the implantation. By this method several kinds of atomic species, such as Li, Na, K, Rb, Xe were encapsulated into the fullerenes [1]. However evidence for the Fe@C⁶⁰ has not been found yet.

During the analysis of the irradiated samples three questions must be answered.

1. Are there iron atoms in the layer and where?
2. Does the iron bond to the fullerene?
3. How does the iron bond to the fullerene, inside or outside?

Using different investigation tools, SNMS (Secondary Neural Mass Spectrometer), MALDI-TOF (Matrix Assisted Laser Desorption Ionization Time of Flight), XPS (X-ray Photoelectron Spectroscopy) or HPLC (High-Performance Liquid Chromatography), all these questions could be clarified step by step.

In this paper we made the first steps to answer the first question: fullerene layers irradiated by iron ion beam delivered by the ATOMKI-ECRIS have been analyzed by the ATOMKI-SNMS. The evaporated 90 - 120 nm

thick fullerene layers on Si holder were irradiated by Fe⁵⁺ and Fe⁺ ion beams produced from Ferrocene vapor. Samples were irradiated with two different doses ($5 \cdot 10^{18}$ ion/cm³ and 10^{22} ion/cm³) at four ion energies (65 keV, 6.5 keV, 0.2 keV and two of these samples at four energies from 4 keV up to 65 keV).

The samples were investigated by SNMS and depth profiles were recorded. The continuous line in Fig. 1. shows the iron distribution in the fullerene film at 6.5 keV irradiation energy.

The well-known SRIM (Stopping and Range of Ions in Matter) code was used to check the curve measured experimentally. Longitudinal distribution of 10^5 iron ions was simulated at fullerene (dots in Fig. 1)

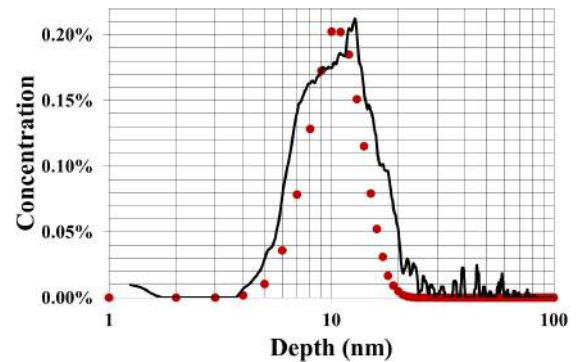


Figure 1. Distribution of the iron in the fullerene layer measured by SNMS (black line) Red dots are the results of SRIM simulation.

Good agreement was found between the measurements (SNMS) and simulations (SRIM) for all the investigated samples. New irradiations with higher Fe-dose are planned to be carried out soon in order to use other methods (e.g. XPS) for answering the second and third questions.

[1] S. Watanabe, N. S. Ishioka, H. Shimomura, H. Muramatsu, T. Sekine, Nucl. Instrum. Methods B **206** (2003) 399

5.16 Total and angular differential elastic cross sections of fusion related materials

R. Rácz, D. Tskhakaya^{a)}, D. Coster^{b)}, K. Tórkési

Within the framework of the international nuclear fusion and engineering project, ITER (International Thermonuclear Experimental Reactor) the World's largest and most advanced tokamak nuclear fusion reactor is currently being built at Cadarache in the south of France. The ITER project aims to make the long-awaited transition from experimental studies of plasma physics to full-scale electricity-producing fusion power plants. For the accurate simulation of the processes in the active fusion reactor, numerous atomic, molecular, nuclear and surface related data are required. Among other data, elastic cross sections of fusion related materials are also needed.

In this work the total and angular differential elastic cross sections of hydrogen atoms for a wide range of incident electron energy were calculated. We used the code described in Ref. [1], where the partial expansion method is applied to obtain the differential and total cross sections of the elastic scattering. The elastic scattering of relativistic particles is described by the direct $f(\theta)$ and spin-flip $g(\theta)$ scattering amplitudes. The relativistic differential cross section per unit solid angle is given by

$$(1) \quad \frac{d\sigma_e}{d\theta} = |f(\theta)|^2 + |g(\theta)|^2$$

where θ is the scattering angle. Details of the calculations can be found elsewhere [1].

Figure 1. shows our results, where the angular differential elastic cross sections for incident electron energy between 100 eV and 100 keV is plotted. The bin size of the incident electron energy was 50 eV from 100eV to 1000 eV, 500 eV from 1 keV to 10 keV and it was 5 keV between 10 keV and 100 keV. The dominant contribution appears at forward scatter-

ing angles. The cross sections decrease significantly with increasing scattering angles. We also found that the higher incident electron energies correspond to lower cross sections.

Further calculations are in progress for other target materials and the results will be published soon.

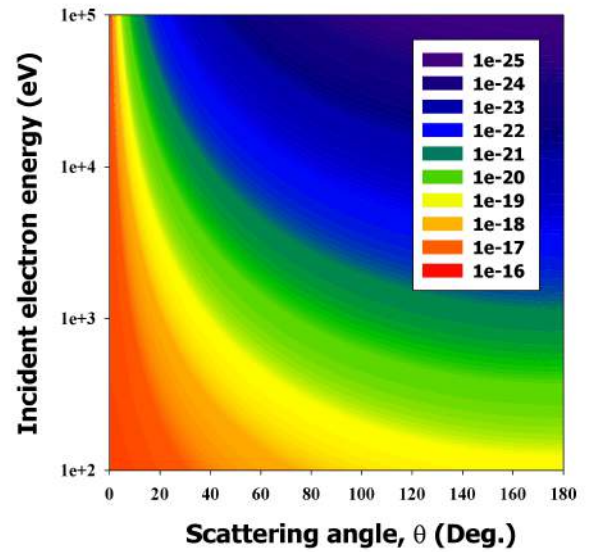


Figure 1. Elastic scattering cross section as a function of the incident electron energy and scattering angle.

Acknowledgements

This work, supported by the European Communities under the contract of Association between EURATOM-HAS, was carried out within the framework of the Task Force on Integrated Tokamak Modelling of the European Fusion Development Agreement.

a) Institute for Theoretical Physics University of Innsbruck, Innsbruck, Austria

b) Max-Planck-Institut für Plasmaphysik, Garching, Germany

[1] F. Salvat, R. Mayol, *Comput. Phys. Commun.* **74** (1993) 358

6.1 Fourth interlaboratory comparison exercise for $\delta^2\text{H}$ and $\delta^{18}\text{O}$ analysis of water samples (WICO2011)

G. Vodila, I. Futó

The IAEA Isotope Hydrology Laboratory organized the fourth interlaboratory comparison exercise for the analysis of hydrogen and oxygen stable isotope composition of water. Four water samples prepared and calibrated at the IAEA Isotope Hydrology Laboratory were labelled IAEA-OH-13 to IAEA-OH-16. Altogether 137 laboratories from 53 countries submitted 172 datasets to the IAEA.

Samples cover the range of $\delta^{18}\text{O}$ and $\delta^2\text{H}$ values typical of natural waters. Each laboratory received four samples with a randomly assigned identification code.

The reference values were calculated from the results of the 12 laboratories whose performance was the best in the last intercomparison exercise, WICO2002 (Table 1). Cumulative deviations for $\delta^{18}\text{O}$ and $\delta^2\text{H}$ are less than 0.2‰ and 2.0‰, respectively.

Table 1. Reference values of the samples

Sample	$\delta^{18}\text{O}$		$\delta^2\text{H}$	
	Mean [‰]	SD [‰]	Mean [‰]	SD [‰]
OH-13	-0.96	0.04	-2.84	0.60
OH-14	-5.60	0.05	-38.30	0.36
OH-15	-9.41	0.04	-78.26	0.38
OH-16	-15.43	0.04	-114.62	0.43

Statistical analysis of the submitted results was undertaken to assess the performance of each laboratory (precision and accuracy) with respect to the reference $\delta^{18}\text{O}$ and $\delta^2\text{H}$ values for the analysed four samples by a two-stage statistical treatment adopted in previous IAEA interlaboratory exercises.

Table 2. Stable isotope values of the samples measured by our laboratory

Sample	$\delta^{18}\text{O}$		$\delta^2\text{H}$	
	Mean [‰]	SD [‰]	Mean [‰]	SD [‰]
OH-13	-0.98	0.10	-2.5	1.7
OH-14	-5.51	0.11	-38.2	1.7
OH-15	-9.41	0.11	-79.0	1.8
OH-16	-15.42	0.11	-115.4	2.0

From our results (Table 2) it is generally seen that the mean values are within uncer-

tainty the same as the reference values, however, our standard deviations are significantly higher.

Fig. 1. shows the obtained value of each laboratory for the $\delta^{18}\text{O}$ of the OH-16 sample and the $\delta^2\text{H}$ value of the OH-14 sample, respectively. Our values are indicated by black arrows. The upper and the lower horizontal black lines show the 1σ deviation of the reference value (middle line).

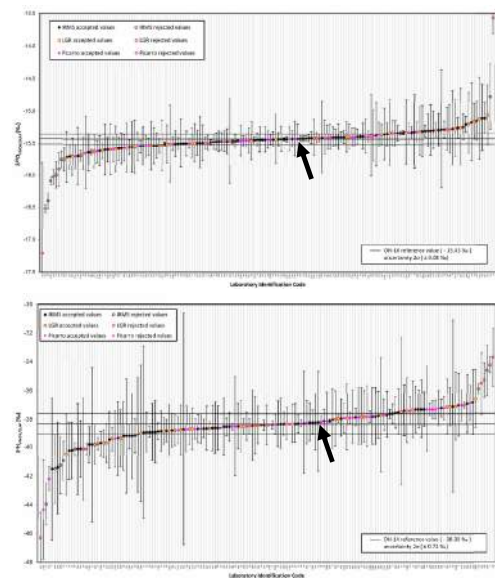


Figure 1. The obtained value of each laboratory for the $\delta^{18}\text{O}$ of the OH-16 sample (top) and the $\delta^2\text{H}$ value of the OH-14 sample (bottom).

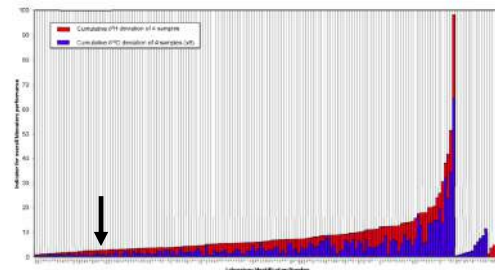


Figure 2. Cumulative deviation of our samples from the reference values determined as $8\delta^{18}\text{O} + \delta^2\text{H}$.

Fig. 2. shows the cumulative deviation of datasets from the reference values determined as $8\delta^{18}\text{O} + \delta^2\text{H}$. According to these data, our dataset (black arrow) is the 25th best out of the 172 datasets of 153 laboratories in the world.

6.2 Noble gas constraint on genesis of the multistacked Répcelak CO₂-CH₄-N₂ gas field Western-Hungary

L. Palcsu, I. Vető^{a)}, I. Futó, G. Vodila, L. Papp, Z. Major

Study of composition and isotopic composition of multistacked gas fields can result in a better understanding of the generation and migration of CO₂ and N₂-rich gases during development of the Pannonian Basin System. The gross compositions of the samples studied fit well with the trends displayed by the individual gas pools at Répcelak and Mihályi. The isotopic compositions of the main components show significantly smaller scatter at Mihályi than at Répcelak. These differences between the two sample sets are likely related to the more homogeneous gross composition of the Mihályi samples relative to that displayed by the Répcelak samples. The concentration ranges of the three noble gases are of one or in the case of the neon, even two orders of magnitude broader at Répcelak than at Mihályi. These marked differences in concentrations of argon, helium and neon between the two sample sets are likely related to the more homogeneous gross composition of the Mihályi samples relative to that displayed by the Répcelak samples. The helium isotopic composition of the two sample sets, expressed in term of R/R_a , are distinctly different. R/R_a ranges between 1.69 to 1.99 and 3.18 to 4 at Répcelak and Mihályi, respectively. Carbon isotopic composition of the CO₂ agrees with both the carbonate decomposition and mantle degassing origins. On the contrary, the very light isotopic composition of the helium (Fig 1.) shows that the CO₂ is of predominantly mantle origin in both fields. Since nitrogen is an ubiquitous minor component of gases extracted from MORB rocks, a small amount of nitrogen certainly accompanied the CO₂ accumulated at Répcelak and Mihályi. The basaltic volcanism, active in the Danube basin between 7 to 4 Ma, seems to be closely related to the CO₂ flux charging the Répcelak and Mihályi fields. This makes likely that the accumulation of the CO₂ took place between 7 to 4 Ma. It is rather possible that the accumulation was a relatively short process. Supposing a general rate of

trapping, about 20Ka were necessary for the accumulation of the about 5 Md m³ CO₂ at Répcelak.

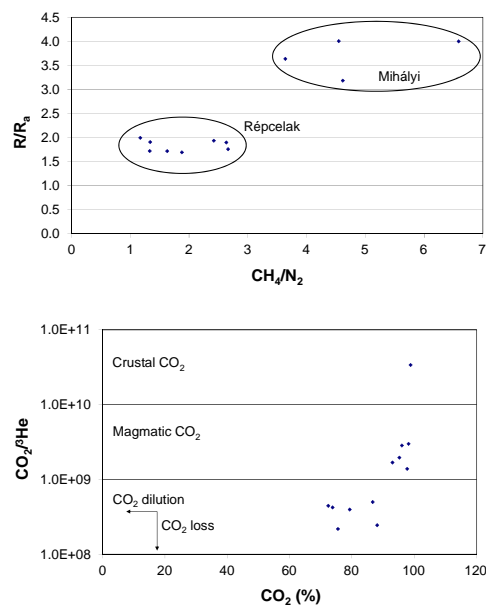


Figure 1. Isotopic and composition characteristics in the gas samples of Répcelak-Mihályi fields.

The conclusions of the present study are the follows: 1. The “pure” CO₂ accumulated in Mihályi and Répcelak has been liberated from separate mantle derived magmatic bodies during the 7 to 4 Ma time interval. 2. The bulk of the HC-gas/nitrogen mixture trapped in the middle and upper pools of the Répcelak field are of roughly common metagenetic origin. 3. The strong heating needed for metagenetic nitrogen and HC-gas generations was the result of heat production by the cooling mantle derived magmatic bodies. The source rocks, either in the basement or in the deeper part of the Danube basin, were located significantly above these magmatic bodies, hence their heating postdated the cooling of the mantle derived magmatic bodies. The HC-gas/nitrogen mixture entered the Répcelak field after the accumulation of the “pure” CO₂ gas.

a) Geological Institute of Hungary, Stefánia 14. Budapest, 1143 Hungary

6.3 Soil C-14 dating of the Lyukas-halom kurgan

M. Molnár, É. Svingor, L. Rinyu, A. Barczy^{a)}, K. Joó^{a)}

In this study we estimated the date of the construction of Lyukas-halom kurgan using C-14 measurements of the buried soil. For these purpose we used a wet combustion method and then measured the C-14 age of the bulk soils and for comparison we eliminated and dated the humic acid fraction (soil organic matter fraction soluble in 0.5 M NaOH at 80°C, 24h) of the soil samples also.

The time what we wanted to measure is the time of the burial of the mound. That time a living surface soil layer was covered with a big amount of mixed soil from another location (likely from the very close vicinity). A living soil has a steady-state "apparent" radiocarbon age which is resulted by the accumulation of biological carbon over hundreds or thousands of years (reservoir-effect) in equilibrium with the radiocarbon decay of C-14. To have an estimate about the original apparent C-14 age of the palaeosol layer under the Lyukas-halom kurgan we measured the apparent age of recent top soil at the top of the kurgan, at 30 m far from the kurgan and at 100 m distance from the kurgan.

The applied reservoir correction gave a reliable result in case of bulk recent samples at the closer reference point (R-I, 30 m far from the kurgan centre) and also at the top soil of the kurgan (Ly-layer 10, A-horizon) as their corrected age was "zero" (within the measurement error) showing that they are modern samples in fact (Figure 1.). The top recent soil of the kurgan (Ly-layer 10, A-horizon) has still a significant apparent age for the humic acid fraction after the reservoir correction (1010 ± 100 BP). Inside the kurgan body and under the kurgan (sample Ly-layer 2, Ly-layer 3, Ly-layer 6 and Ly-layer 11) the humic acid fraction age profile is systematically younger than the age profile of the parallel bulk fractions. The kurgan was dated to be at the radiocarbon age between 4670-3520 C-14 years BP using the humic acid fraction C-14 ages. However this age is in very good agreement with the reservoir corrected bulk fraction radiocarbon age of the ancient surface soil layer (4060 ± 110 C-14 years BP).

a) Szent István University, Gödöllő, Hungary

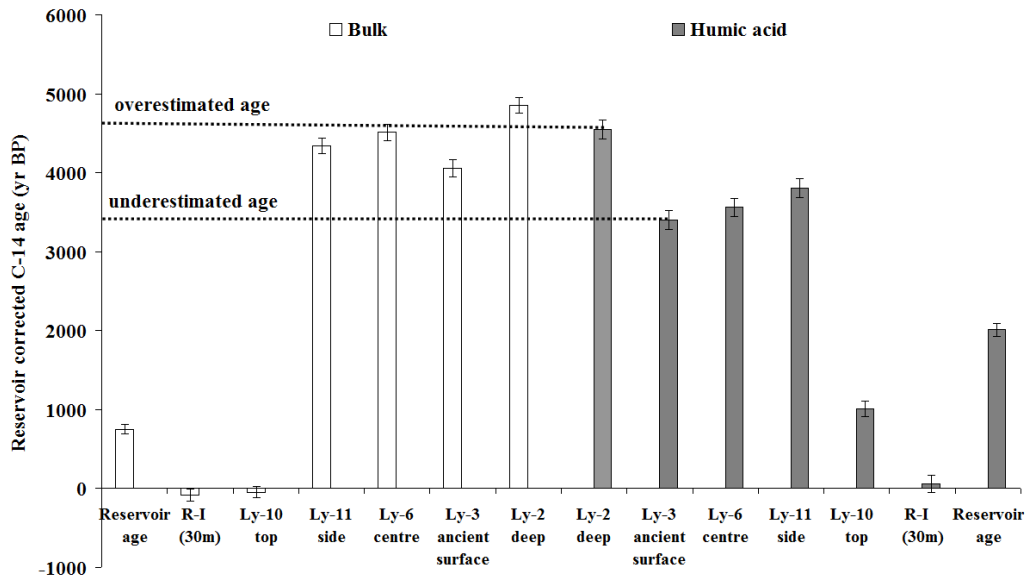


Figure 1. Reservoir corrected C-14 ages for the bulk and the humanic acid soil fractions of the kurgan

6.4 C-14 dated paleoenvironmental changes on Lake Kolon during the last 25,000 years

P. Sümegei^{a)}, M. Molnár, G. Jakab^{b)}, A.J.T. Jull^{c)}

One of Hungary's geological and environmental treasures is nestled in the heart of the Great Hungarian Plain. The catchment basin of Lake Kolon was subjected to detailed environmental historical studies starting in 2005. Undisturbed cores taken along transects of the basin were subjected to detailed sedimentological, paleoecological, and geochemical studies (Figure 1).

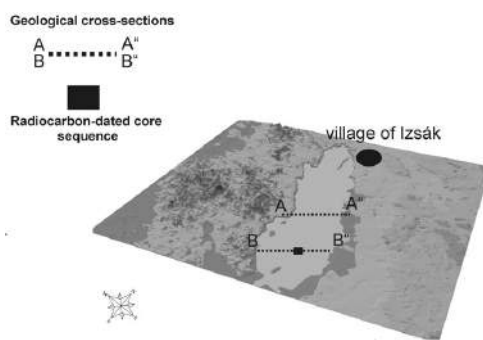


Figure 1. Catchment basin of Lake Kolon in the Danube Valley and the coring site.

To establish a reliable timeframe of the lacustrine and marshland sedimentary sequence

identified, 22 samples were analyzed by accelerator mass spectrometry (AMS) in the radiocarbon laboratories of Poznan and Tucson.

With the new results in hand (Figure 2), we had the opportunity to elucidate the geological evolution of the area for the past 25,000 yr. This sequence is highly beneficial, as it is probably the most well-dated profile of the Quaternary from the area studied. The new absolute dates enabled the comparison of local geological evolution of the studied area with those of global climatic changes.

As seen from our findings, the geological evolution of the catchment basin was congruent with major climatic events during the Pleistocene and the entire Holocene. However, a very peculiar trajectory was identified for the terminal part of the Pleistocene and the opening of the Holocene regarding the evolution of the landscape, the vegetation, and the fauna of this part of the Great Hungarian Plain.

- a) University of Szeged, Szeged, Hungary
- b) Tessedik Sámuel College, Szarvas, Hungary
- c) University of Arizona, Tucson, Arizona, USA

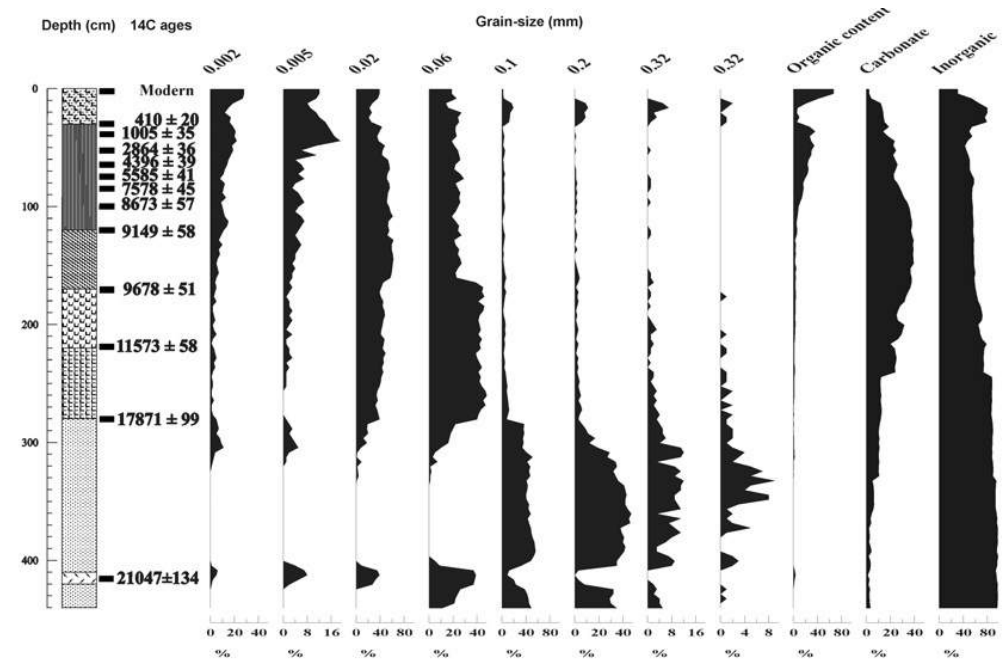


Figure 2. Results of grain-size analysis and loss on ignition (LOI) for the C-14 dated core.

6.5 Noble gas measurements from 1-3 μl of AEW

L. Papp, L. Palcsu, Z. Major

Here we describe the noble gas measurement procedure adapted to very small samples of air equilibrated water (AEW) in the range of microlitres.

In this paper we focus on the description of determination of noble gases and water. To check the reliability of the whole measurement procedure, standard water samples have been measured. As for standard samples, we prepared AEW in conditioned circumstances, and then copper capillaries were filled with AEW. When the water has been extracted from the copper capillary, the amounts of both water and dissolved noble gases have to be determined to obtain noble gas concentrations at the end. Thus, two independent measurements play an important role in this measurement procedure: 1. water determination; 2. determination of noble gas abundances. The temperature of the water was 20.5-21.5 $^{\circ}\text{C}$, and the ambient air pressure varied between 0.985 and 0.990 atm. Having completed the copper capillary assemblage, the AEW is allowed to flow through the capillary. After a few millilitres of water have passed through, two pairs of small clamps close up a certain section of the capillary. The capillary is then attached to the inlet line of the mass spectrometric system.

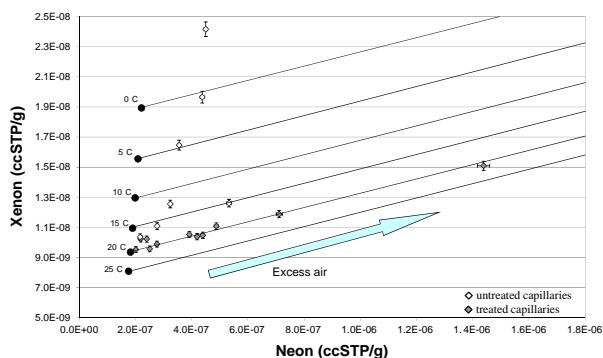


Figure 1. Xenon concentrations are plotted against neon concentrations of the air equilibrated water samples that have been prepared at ~ 21 $^{\circ}\text{C}$ (empty squares represent untreated capillaries, while full squares do treated capillaries).

In Figure 1 the measured xenon and neon concentrations are shown. It can be seen that the first results show excess xenon and neon compared to solubility concentrations. This excess cannot be explained by admission of unfractionated excess air (due to a leak, or remaining air bubble in the capillary), as its elemental ratios of xenon and neon are different from those of air. If excess air contributed to the solubility concentrations of the AEW samples the xenon-neon concentrations should be increasing along the excess air line as shown in Fig. 1.

We assume that the excess is due to an artefact of the filling procedure of the copper capillaries. This excess is much more abundant than a normal blank of the system or even a blank obtained from a squeezed empty copper capillary. To eliminate the excesses, we therefore used two pre-treatment procedures. First we flushed out the copper capillaries with pure helium, while heating it at 200 $^{\circ}\text{C}$ for an hour. After the copper had cooled down to room temperature, AEW was let through the capillary, avoiding penetration of air into the inner part of the capillary. In the second pre-treatment method, the copper capillary was submerged in the AEW, and a pump continuously pushed the water through the capillary for at least half an hour. The plot in Figure 1 demonstrates that the results obtained from measurements of pre-treated capillaries are closer to the expected values than in the case of untreated capillaries. These results do not yet completely fit the expectations, but they are much closer. We think we obtained real noble gas concentrations from tiny samples of water enclosed in copper capillaries, but they contained unexpected concentrations derived from a solubility equilibrium component and an excess as an artefact of the preparation. The pre-treatment of the capillaries allows us to obtain better results that are closer to the expected solubility concentrations.

6.6 C-14 signal of the Paks Nuclear Power Plant in the nearby treerings

R. Janovics, Z. Kern^{a)}, W. Lukas^{b)}, I. Barnabás^{c)}, M. Molnár

A part of C-14 isotope emitted by Paks Nuclear Power Plant (NPP) goes to the atmosphere as inorganic CO₂ gas, furthermore, a part of the hydrocarbons emitted in a higher quantity is oxidised to CO₂ in the environment. Trees mostly cover their carbon demands by the uptake of atmospheric CO₂, since they incorporate carbon-dioxide via photosynthesis into their organic materials. Normally cellulose is not reutilised by the metabolism once generated, therefore, the changes in the atmospheric C-14 activity concentration can possibly be fingerprinted by the measurements of the radiocarbon activity in the tree rings. We collected tree ring series representing the past 10 years from the vicinity of the nuclear power plant and from a background area (B24 at Dunaföldvár). Measurements were performed by high-precision AMS 14-C method at ETHZ Zürich. The tree ring radiocarbon activity concentration data of the surrounding tree rings were compared to the background ones for each year.

The C-14 activity concentration of the atmosphere has been continuously decreasing since the nuclear weapon tests in 1965. The decreasing trend can also be observed in case of the samples collected by the atmospheric C-14 sampling units operating at the monitoring stations of Paks NPP[1].

This decreasing trend can also be observed both in the results of the annual rings of trees in the background and in the vicinity of the NPP (Fig.1). The C-14 activity concentration of the tree rings was decreasing by nearly 4 pMC in the course of the last 10 years. The age of the sample trees is around 10 years. As they were planted saplings, the data of the first three years after 2000 for the Paks tree ring samples can be considered to be background values.

It is seen in Figure 1 that the C-14 activ-

ity concentration of the tree rings of the first three years are the same for Paks and the background site (B24) within uncertainty as it was expected.

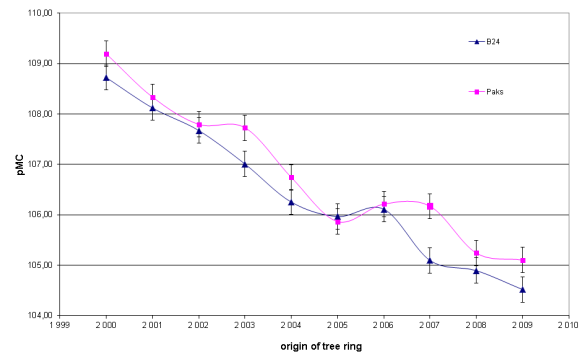


Figure 1. Ten year C-14 activity concentration record in the tree rings at Paks NPP and the background site (B14).

In 10th April 2003 a malfunction occurred at the block no.2 of Paks NPP, and a small amount of radioactive material was emitted to the environment [2]. The tree rings of 2003 and 2004 of the Paks samples have higher C-14 activity concentrations that might indicate the excess C-14 emission due to the malfunction in the NPP.

To interpret the slight increase in 2007 further research is made using the data of the emissions of the Interim Spent Fuel Storage Facility and Paks NPP.

Acknowledgements

The research project was supported by the OTKA MB-08A 81515 grant.

a) MTA GKI Budapest, Hungary

b) ETH Zürich, Switzerland

c) RHK Kft., Budaörs, Hungary

[1] Molnár M., Bujtás T., Svingor É., Futó I., Svetlik I., Radiocarbon, Vol 49, Nr 2, 2007, p 1031-1043

[2] Szatmáry Z., Fizikai Szemle 2003/8. 266.o. BME, Nukleáris Technikai Intézet

6.7 Fossil carbon in the winter time aerosol in Debrecen city, 2010

I. Major^{a)}, M. Molnár, R. Janovics, E. Furu, Zs. Kertész

From October 2010, radiocarbon measurement of atmospheric aerosol was begun in Debrecen city, Hungary. Aerosol samples were collected simultaneously with the already ongoing atmospheric CO₂ observations and were measured by a mini accelerator mass spectrometer (MICADAS) at ETHZ, Zürich [1].

Our results showed that the ratio of the fossil (radiocarbon-free) carbon is relatively higher in the carbon content of the urban aerosol (Deb-AS1, Deb-AS2) than in the carbon of the atmospheric CO₂ (Deb-CO₂) collected in the same location and time (Figure 1.). Fossil carbon content of the atmospheric carbon-dioxide samples was rather constant and low (2-3%) above to the background signal of Dunaföldvár (Dunaf-CO₂). Fossil carbon in aerosol samples was higher by an order of magnitude and during the winter a significant decrease was observed towards to the colder weather. The direction of this trend was just the opposite what we saw in case of the atmospheric fossil CO₂.

It is very likely that the reason of the increasing biogenic (modern) carbon fraction in the atmospheric aerosol could be the increasing domestic wood burning for heating purpose during the colder period of the winter as wood fire can give a significant amount to the aerosol.

For ¹⁴C measurement of aerosol samples special sample preparation methods were developed and tested. The reproducibility of preparation and C-14 analyses was checked by 2 parallel preparations for the November 2010 and December 2010 samples (Deb-AS1 and -AS2 pairs in Figure 1.). Parallel results verified the excellent reliability of the applied methods.

Acknowledgements

The research project was supported by the OTKA MB-08A 81515 grant.

a) University of Debrecen, Debrecen, Hungary

[1] Synal H.-A., Stocker M. and Suter M., Nucl. Instr. and Meth. B 259 (2007) 7-13

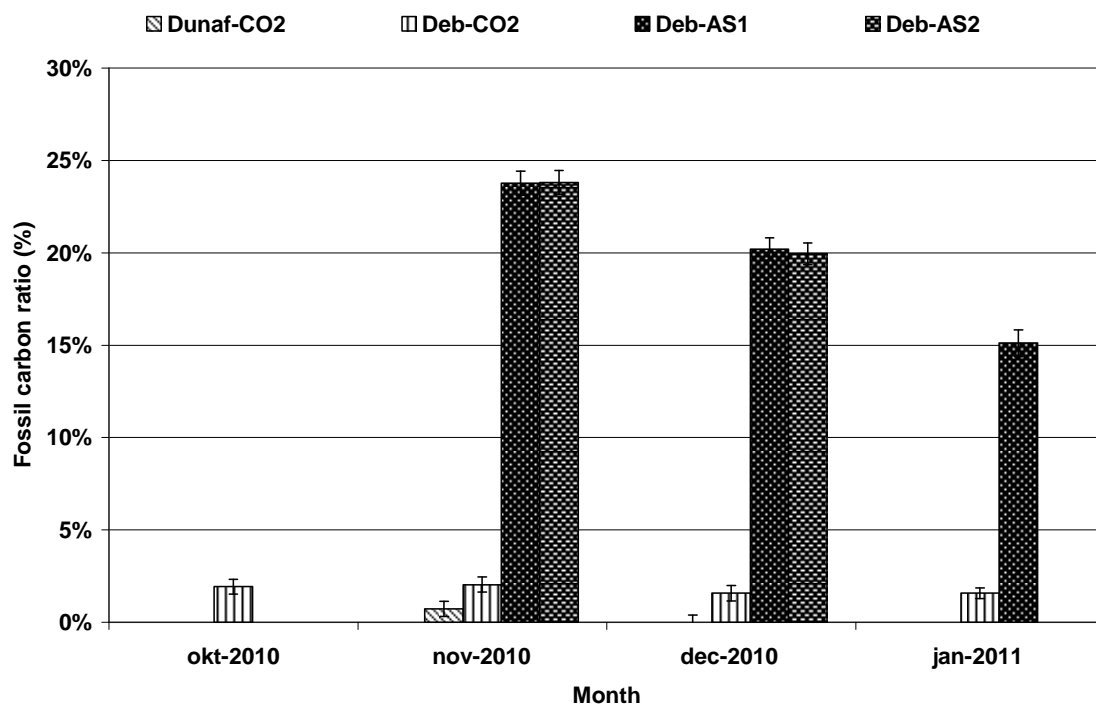


Figure 1. The fossil carbon in atmospheric aerosol and carbon-dioxide samples in Debrecen city.

6.8 Chemical characterization of workplace aerosol particles at Atomki

Z. Szoboszlai, G.U.L. Nagy, Zs. Kertész, A. Angyal, E. Furu, Zs. Török, K. Ratter^{a)}, P. Sinkovic^{a)} and Á.Z. Kiss

A workplace is typically such an environment where people are staying in a limited space during long-term periods. In this case study we selected three totally different microenvironments of the Institute of Nuclear Research (Atomki).

Four 48-h long measurement campaigns were carried out in an outdoor and in three indoor places: in the garden, in the control room of the Van de Graaff (VdG) accelerator under the ground level, in the mechanical workshop on the ground level and in the library at the 4th floor. The elemental compositions (for $Z \geq 13$) of the samples were measured by particle induced X-ray emission (PIXE) method in the IBA Laboratory of ATOMKI.

Moreover, elemental and morphological analysis was performed using a FEI (Focused Ion Beam combined with a Scanning Electron Microscope) Quanta 3D Dual Beam System at the Department of Materials Physics, Eötvös University, Budapest.

Based on the concentration data we found that relative to the outdoor atmosphere inside the working environments the air was rather polluted. The PM_{10} concentrations showed bigger variability at the workshop and at the VdG laboratory while at the library it followed the outer PM_{10n} level. However the $PM_{2.5}$ values were broadly equal with the $PM_{2.5}$ concentrations of the outer air. The fine particulate matter (PM) concentrations showed seasonal variability: higher concentrations were in winter than in summer.

The indoor/outdoor ratios, averaged over the 4 campaign showed that the coarse values were the lowest at the library (0.78) and were higher than 1 for the VdG laboratory (1.38) and for the workshop (1.35). In the case of library the reason of the low I/O ratio can be explained by the lower penetration of coarse particles from outdoor. The concentration of coarse particle at the level equal with the 4th floor is usually less than at the ground level. On the other hand, the activities - which

favours to the resuspension and generation of coarse particles - were much less in the library than in the other two places.

In the workshop high amount of heavy metal containing (Fe, Zn and Cu) particles were detected which originated from the mechanical processes (e.g. milling and turning). Immense concentration of wolfram and some amount of cobalt was also observed both in the fine and the coarse fraction. These metal elements most probably originated from the abrasion of various metal tools. This was confirmed by the fragmented morphology of a W and Co containing particle (Fig. 1a.). High amount of Fe were found both in the coarse and in the fine fraction. Based on the morphology these particles may be arisen from high temperatures (Fig. 1b.) and spindle (Fig. 1c.) processes.

In the library and the VdG laboratory we found some indoor sources such as cleaning materials (Cl) and renovation related cement (Ca, S, Fe and Zn). In the library and the workshop we showed that after replacing the windows with better isolating ones the penetration of outdoor air decreased.

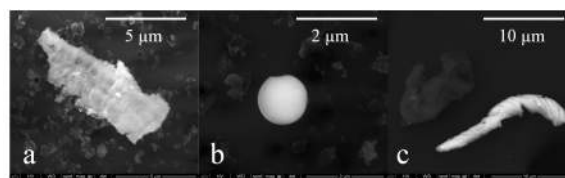


Figure 1. Secondary electron images of a W-Co (a) and a Fe-rich (b) particle. Backscattered electron image of a Fe rich particle (c).

Acknowledgements

The work was supported by the TÁMOP-4.2.2/B-10/1-2010-0024 project and co-financed by the European Union and the European Social Fund. This work was supported by the Hungarian Research Fund OTKA and the EGT Norwegian Financial Mechanism Programme (contract no. NNF78829) and the János Bolyai Research Scholarship of the Hungarian Academy of Sciences. The SEM analysis is supported by the European Union and co-financed by the European Social Fund (grant agreement no. TÁMOP 4.2.1/B-09/1/KMR-2010-0003).

a) Dept. of Materials Physics, Roland Eötvös University, Budapest

6.9 Determination of radioactivity of ^{79}Se in waste of NPP using ^{75}Se as tracer

Z. Szűcs, S. Takács, M. Mogyorósi, B. Kovács^{a)}, D. Andrásfi^{a)}

Long-lived radionuclides such as ^{79}Se in waste materials of nuclear power reactors are always a potential risk for the impact of radio-contamination in the environment of the repository site because of their potential migration ability by leaching/dissolution and then transportation by flowing groundwater [1]. The estimated activity of ^{79}Se isotope comparing to other radioisotopes in the waste is very small and its radio-detection is so difficult that radiochemical separation and enrichment is necessary before the measurement. ^{75}Se is suitable for tracking the separation method and can be used to follow the chemical yield of the separation process step by step.

The production of ^{75}Se was carried out on the compact cyclotron in Debrecen by the $^{75}\text{As}(p,n)^{75}\text{Se}$ nuclear reaction. The target material was the NaH_2AsO_4 , which can be easily dissolved in alkaline waste solution. The proton beam energy was chosen to be 13 MeV, which was below the threshold energy of the $^{23}\text{Na}(p,2n)^{22}\text{Mg}$ and $^{23}\text{Na}(p,d)^{22}\text{Na}$ reactions, avoiding the parallel production of unwanted ^{22}Na long lived contaminating radionuclide on the sodium content of the target material.

The thickness of the pressed target was optimised in order to minimize the dissipated beam energy in the low melting point target material. An irradiation with beam dose of 7 μAh was able to produce the activity of 2.2 MBq of ^{75}Se due to the high cross section of the used nuclear reaction. This amount of ^{75}Se activity could cover the necessary quantity of radio-selenium for tracing work. The chemical separation process was carried out as described earlier in [2]. ^{75}Se tracer with activity of 13-15 kBq and 50 mg of inactive Selenium in selenite form as carrier were used for each sample. The

amount of the inactive Selenium as well as of the ^{79}Se was measured by ICP-MS method. The activity of ^{75}Se was measured by high purity germanium γ -detector. The results underlined that the ^{75}Se tracer is better choice to track the chemical processes than the inactive Selenium carrier, because of limited suitability of ICP-MS in mg scale of Selenium in the sample.

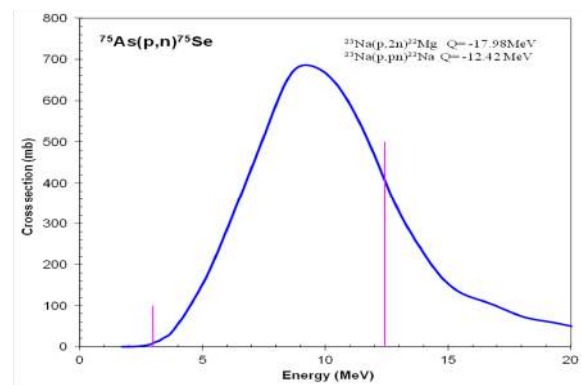


Figure 1. Optimal energy range for production of ^{75}Se by proton on MGC-20 cyclotron in ATOMKI.

Table 1. Determination limit of ^{79}Se in waste sample measured by ICP-MS.

Name of sample	01T35 bottom	02T151 middle	01TM23	02TM23
^{79}Se [Bq/dm ³]	< 15.4	< 57.1	< 140	< 18.7

a) Institute of Food Science, Quality Assurance and Microbiology Centre for Agricultural Sciences and Engineering, University of Debrecen

[1] Z F. Seby, M. Potin-Gautier, E. Giffaut, O.F.X. Donard, *Analisis* **26** (1998) 193.

[2] Á. Bihari, M. Mogyorósi, Z. Szűcs, and B. Kovács, *Atomki Annual Report 2009 (2010)* **64**

7.1 Major and trace elements in mouse bone measured by surface and bulk sensitive methods

I. Benkő^{a)}, I. Rajta, A. Csik, J. Tóth, K. Benkő^{b)}, K. Géresi^{a)}, É. Ungvári^{a)}, B. Szabó^{c)}, G. Sarkadi, B. Paripás^{d)}, I. Takács^{e)} and K. Tőkési

In the past years an increasing research interest turned to the accurate determination of the components of bone samples. These investigations focused on both the major and trace elements in the bone. Work in this field is strongly motivated because various major and trace element concentrations can be good indicators of several diseases. Number of studies also focused on the determination of the components both in the organic and inorganic parts of the bone separately, because they both have role during bone remodeling processes. Also important to note that bone can be one of the final destinations in the body where toxic elements are deposited.

In this work we performed various surface and bulk sensitive analyses for the mouse bone samples to determine its major and trace element components [1]. We have shown concentration profiles for various major and observable trace elements of the mouse bone. We found, in accordance with our expectation, that the mostly surface sensitive XPS technique is not suitable to determine the concentration of the trace elements in bone samples. It was also shown that XPS is a valuable tool not only in the determination of the chemical states of the major components of the bone powder but in the quantitative determination of their relative concentrations. Both the major and the trace elements of the bone samples are determined using PIXE and SNMS spectra. Although the information depths are very different for PIXE (a few tens of micrometer) and for XPS analysis (a few nanometers), our present PIXE result, using the bone sample in its original form for the concentration ratio between Ca and P is in excellent agreement with

the XPS results using calcinated mouse bone powder. Discrepancy in Ca/Mg ratio (PIXE: 35.7 and XPS: 12.7) maybe due to many factors, which influence this ratio in bone samples. In the case of PIXE we studied native bones and determined composition of the compact bone at outside surface. By XPS method we measured the composition of the calcinated bone powder, a mixture of the compact and trabecular bone. In the compact bone, the ratio between the cells and the extracellular matrix with minerals is less than in the trabecular bone. The most likely explanation that magnesium, which is characteristically situated in the intracellular space, deliberated during the calcination and appeared homogenously in the bone powder. Further critical analysis of larger data set is in progress and will be published soon.

Acknowledgements

The work was supported in part by the Hungarian Scientific Research Fund OTKA Nos. K67873, K72172, K73703 and by cost action No. MP1002. This work was partly carried out as part of the TÁMOP-4.2.1.B-10/2/KONV-2010-0001 project in the framework of the New Hungarian Development Plan.

- a) Dept. of Pharmacology and Pharmacotherapy, Medical and Health Science Center, Uni. Debrecen, Hungary
- b) Euromedic Diagnostics Ltd, Debrecen, Hungary
- c) Heart Center, Semmelweis University, Budapest, Hungary
- d) University of Miskolc, Miskolc, Hungary
- e) Dept. of Internal Medicine, Semmelweis University, Budapest, Hungary

- [1] I. Benkő, I. Rajta, A. Csik, J. Tóth, K. Benkő, K. Géresi, É. Ungvári, B. Szabó, G. Sarkadi, B. Paripás, I. Takács, and K. Tőkési, Nucl. Instr. and Meth. Phys. B 279 (2012) 223

8.1 Status report on the accelerators operation

S. Biri, Z. Kormányi, I. Berzi, R. Rác

During 2011 our particle accelerators operated as scheduled, safely and without major or long breakdowns. The utilization rates of the accelerators were similar to the preceding year. The cyclotron delivered 1735 hours and the 40-years old 5 MeV Van de Graaff generator supplied more than 1900 hours. The 1 MeV Van de Graaff accelerator was also operated for several short basic physics experiments last year (84 hours) with requests for much more beamtime in 2012. The plasma and beam-on-target time at the ECR ion source was less than in previous years (322 hours) due to several time-consuming technical developments in this laboratory. The isotope separator, as ion beam accelerator was utilized only for a few hours in 2011, since the research and development in this lab focused on other fields. Nevertheless it is continuously available for research requiring special deposition techniques and for isotope tracing studies.

After judging and accepting the importance and quality of our accelerators and staff the title “Strategic Research Infrastructure” was addressed to the Accelerator Center by the Hungarian authorities [1]. In order to get access to the accelerators a new system was introduced. The beamtime (within the frames of the capacities) is available for everyone with equal chance if an acceptable scientific program is provided together with the request. The users have to contact our Program Advisory Committee (PAC). Since last year the requests - both from external or local users - must be delivered by filling out and e-sending on on-line form available in the homepage of the institute [2].

In the next sub-chapters the 2011 operation and development details at the cyclotron, VdG-5 and ECR accelerators are summarized.

Cyclotron operation

The operation of the cyclotron in 2011 was concentrated to the usual 9 months; January, July and August were reserved for maintenance

and holidays. The overall working time of the accelerator was 2603 hours; the time used for systematic maintenance was 360 hours. The breakdown periods amounted to 15 hours last year. So the cyclotron was available for users during 2228 hours. The effectively used beam-on-target time is summarized in Table 1.

The project of building new power supplies for the low-current magnets of the beam transport system has been successfully completed. All quadrupole lenses and steering magnets (10 pieces of each) are now equipped with homebrew new power supplies. The new system was in full operation throughout the year without any significant failure or breakdown.

A new solid-state broadband preamplifier is being built for the cyclotron RF-system. It is not just for replacing the outdated and partly faulty preamplifier module, but also serves as a pilot project for renewal of the existing amplifiers in the RF-system. Due to the limited lifetime and unavailability of the radio-frequency power tubes applied in the driver amplifier, this project is of the utmost importance for the future operation of our cyclotron accelerator.

Table 1. Statistics of the irradiation time (beam-on-target) for different research groups.

Projects	Hours	%
Nuclear spectroscopy	200	11.6
Nuclear astrophysics	824	47.5
Radiation tolerance test	144	8.3
Neutron physics	31	1.8
Isotope production	304	17.5
Thin layer activation (TLA)	232	13.3
Total	1735	100

Van de Graaff electrostatic accelerators

At the VdG-5 machine we had similar beam requirements than in the preceding year. The accelerator was available for the users during 2200 hours and it was actually running 1917 hours in 2011. With the 5 MV Van de Graff accelerator mainly (98%) proton particles were accelerated. There was little need (2%) for ${}^4\text{He}^+$ particles. The beam time was

distributed among different research subjects as shown in Table 2.

We had to open the accelerator tank only 5 times in 2011. There was one planned maintenance week which involved the full disassembling of the charging system. In addition, we had several short-time planned maintenance works in 2011. After five years of operation without any problems, a major maintenance was made on the turbo-molecular pumps of the accelerator tube. Additionally, the 10 tons bridge-crane was renewed.

Table 2. Time distribution among different research activities at VdG-5.

Field	Sign	Hours	%
Atomic physics	AP	152	8
Nuclear physics	NP	264	14
Nuclear astrophysics	NAP	46	2
Analytical studies	IBA	1310	69
Micromachining	MM	121	6
Machine test	MT	24	1
Total		1917	100

Two computer control development projects that started in 2010 have reached the base version state. The vacuum measurement system that is based on two Pfeiffer MaxiGauge control units, has the following features: receiving and presenting data of 12 vacuum measurement heads, switching on/off the heads, writing continuous log of the vacuum data of VdG-5 accelerator tube. The hardware development of the quadrupole control system was finished in the first half of 2011. In September we started to collect data with QuadrupoleControl software to increase the efficiency of beam transport with recalling stored parameters. It has the following features: control of 1 electrostatic and 3 magnetic quadrupole dublet power supplies (Figure 1), storing/recalling of operating parameters, reading from two beam-on-target current meters, VdG-5 beam energy versus analyzing magnet calculator.

In 2011 the VdG-1 machine was working for only 84 hours. There were some test measurements with proton beam for a time-of-flight electron-spectrometer

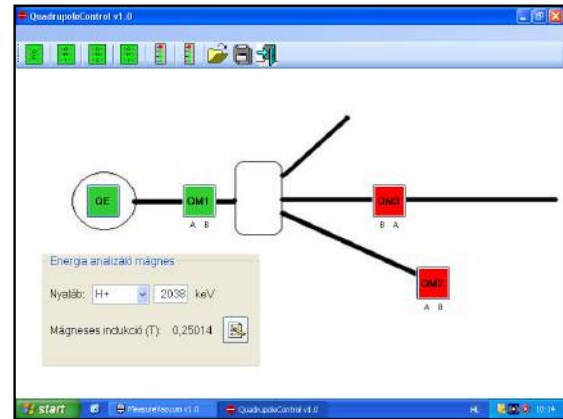


Figure 1. Typical display output of the QuadrupoleControl software installed at VdG-5 beamline.

ECR ion source

Table 3 shows the beamtime distribution the ECRIS supplied in 2011 for users.

As the main technical development, a new NdFeB hexapole permanent magnet assembly was purchased and installed because the 15 years old magnet already partly lost its radial magnetic field strength during the years (the field strength decreased from 1.1 Tesla down to 0.7 Tesla and this decreasing accelerated in the past 2-3 years). The magnetic field of the new hexapole (having almost the same geometry and structure as the old one) is 1.2 Tesla. The beam tests in 2010 with the new radial trap gave excellent results: we could reach or exceed our ever-obtained record highly charged beam intensities within a couple of days test time. In 2011 the hexapole had to be repaired in the manufacturing company due to some technical failures. Simultaneously, some additional soft iron plugs were designed, manufactured and installed for the ECRIS. The first beam tests with the repaired hexapole and with the improved magnetic yoke gave even more promising results. For example, for O^{6+} and O^{7+} a 50% increase of the beam intensity (compared to the old highest values) was detected and recorded.

The ECR ion source was designed and has been mainly used to provide HCI plasmas and positive ion beams. In atomic and molecular physics experiments however molecular ion and negative ion beams play an increasingly impor-

tant role. These ion beams are usually produced in special ion sources. In last year, without any commonly applied tricks (such as usage of cesium or magnetic filter) negative ions of H^- , O^- , OH^- , O_2^- , C^- , C_{60}^- in some cases with several μA intensity were obtained [3]. In the field of molecular ion production, positively charged ions beams of H_2^+ , H_3^+ , OH^+ , H_2O^+ , H_3O^+ , O_2^+ were generated with currents in the mA range [3]. It was found that careful tuning of the magnetic field and the double frequency

mode are very useful at both special beam productions.

The ATOMKI-ECRIS again proved that various requirements for plasma physics investigations, for low energy atomic physics measurements and for applications can be fulfilled by one multi-purpose ECR ion source. In this year a review article was written on the development history and on the main features of the ECR ion source [4].

Table 3. Positive and negative ion beams delivered by the ECRIS in 2011. The total energy of the beams is the product of the charge and the extraction voltage. DE: University of Debrecen, IEP: Institute of Experimental Physics, DAP: Division of Atomic Physics, ECR: ECR Group.

Research topic	User	Ion species	Extraction voltage (kV)	Hours	%
Ion guiding through capillaries	ATOMKI-DAP	He^+ , Ar^+ , Ar^{7+}	0.4-3.0	133.5	41
Surface coating and implantation	DE-IEP, ATOMKI-ECR	Ne^+ , Ne^{6+}	10.0	24.5	8
Fullerene(C_{60}) research	ATOMKI-ECR	C_{60}^+ , C_{60}^- , Fe^+ , Fe^{5+}	0.2-10.0	66.5	21
New hexapole test	ATOMKI-ECR	O^+ , O^{6+} , O^{7+} , Ar^+ , Ar^{8+} , Ar^{11+}	10	22.5	7
Beam development & maintenance	ATOMKI-ECR, ATOMKI-DAP	H^+ , H_2^+ , H_3^+ , C^+ , O^+ , OH^+ , H_2O^+ , H_3O^+ , O_2^+ , H^- , C^- , O^- , OH^- , O^{2-}	5-10	75.0	23
Total				322	100

[1] <https://regisztr.nekifut.hu/en/ki/atomki-gyk>

[2] http://www.atomki.hu/PAC/index_en.html

[3] Rácz R., Biri S., Juhász Z., Sulik B., Pálincás J. : Molecular and negative ion production by a standard ECRIS. Accepted for publication in the Review of Scientific Instruments (2012).

[4] Biri S., Rácz R., Pálincás J.: Status and special features of the Atomki ECR ion source. Accepted for publication in the Review of Scientific Instruments (2012).

8.2 Creation of convex microlenses in PDMS with focused MeV ion beam

S.Z. Szilasi, N. Hegman^{a)}, A. Csik, I. Rajta

In this work the creation of convex microlenses is presented in *poly(dimethylsiloxane)* PDMS using shrinkage of the polymer due to energetic ions [1]. The creation process is based on the observation that the PDMS shrinks due to irradiation [2] and the surface of the unirradiated areas will have a regular curvature between the irradiated places.

The applied proton beam writing (PBW) technique is a rapid, precise and single step method for the creation of microlenses, there is no need of mould creation or further sample treatment. By the nature of this direct-writing method, structures can be positioned precisely on the sample surface.

The presented microlenses are the first direct-written three-dimensional microstructures in PDMS.

The sample preparation and irradiation parameters were described in detail in our paper [1]. The irradiated pattern was a matrix of annuli, which inner diameters were 15, 30, 60, 100 and 200 μm (see an example of the 100 μm annuli arrays on Fig. 1).

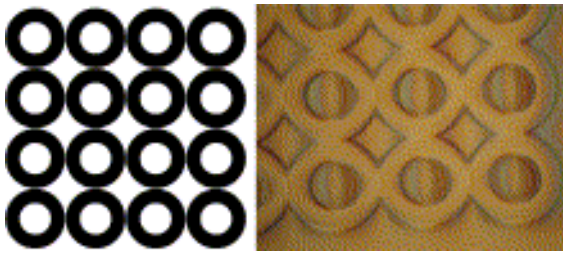


Figure 1. The irradiation pattern and the differential interference contrast microscopy (DIC) image of the 100 μm in diameter microlens array.

After the irradiation the surface topography was investigated by Atomic Force Microscopy (AFM, NT-MDT Ntegra, tapping mode) and a profilometer (AMBIOS XP-I

type). These techniques allowed us to investigate the rate of shrinkage of the irradiated area, the height and the profile of the curved surface and the focal length of the microlenses.

Due to the ion irradiation the surface topology of the PDMS changed, at the irradiated areas shrinkage/compaction occurred. The surface of the unirradiated polymer between the irradiated, and therefore compacted areas, is curved due to the rubbery nature of PDMS.

The AFM images (see e.g. Fig.2) show the geometry of the microlenses.

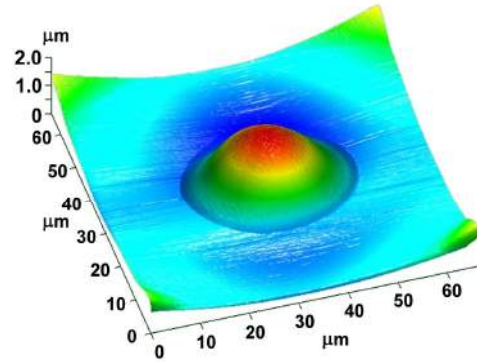


Figure 2. Typical AFM image of a 30 μm diameter microlens. (3D perspective view.)

The profile of the lenses turned out to be parabolic, the focal lengths were found to be between 18 and 180 μm , that can be adjusted with the delivered ion fluence and the lens diameter. By reducing the applied fluence, a longer focal length can be achieved also in case of the small diameter microlenses.

a) Bay Zoltán Foundation for Applied Research Institute for Nanotechnology, P.O. Box 46, H-3515 Miskolc-Egyetemváros, Hungary

[1] S.Z. Szilasi, *et. al*, Microel. Eng. 88 (2011) 2885

[2] S.Z. Szilasi, *et. al*, Appl. Surf. Sci. 257 (2011) 4612

8.3 Sample holder for studying temperature dependent particle guiding

R.J. Berezky, G. Kowarik^{a)}, K. Tókési, F. Aumayr^{a)}

The so called guiding effect is a complex process involving the interplay of a large number of charged particles with a solid. Although many research groups joined this field and carried out various experiments with insulator capillaries many details of the interactions are still unknown.

We investigated the temperature dependence of the guiding since it opens new possibilities both for a fundamental understanding of the guiding phenomenon and for applications.

For the temperature dependent guiding experiments a completely new heatable sample holder was designed [1]. We developed and built such a heatable sample holder to make accurate and reproducible studies of the temperature dependence of the ion guiding effect possible. The target holder (for an exploded view see Fig. 1) consists of two main parts, the front and the back plates. The two plates of the sample holder, which function as an oven, are made of copper. These parts surround the capillary in order to guarantee a uniform temperature along the whole tube. The temperature of the copper parts is monitored by a K-Type thermocouple. Stainless steel coaxial heaters surrounding the oven are used for heating. The heating power up to a few watts is regulated by a PID controller. Cooling of the capillary is achieved by a copper feed-through connected to a liquid nitrogen bath outside the UHV chamber. This solution allows us to change the temperature of the sample from -30°C up to 90°C .

Our experiments with this newly developed temperature regulated capillary holder show that the glass temperature (i.e. conductivity) can be used to control the guiding properties of the glass capillary and adjust the conditions from guiding at room temperature to simple geometrical transmission at elevated temperatures. This holds the promise to investigate the effect of conductivity on particle transport (build-up and removal of charge patches) through capillaries in more details.

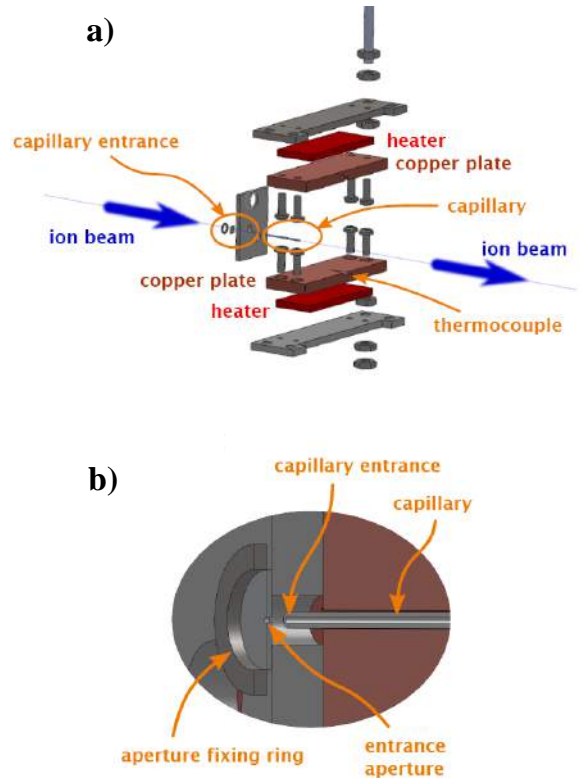


Figure 1. Details of the temperature regulated capillary holder developed in order to study the effect of electrical conductivity on guiding of slow highly charged ions through mesoscopic glass capillaries. (a) Exploded view of the heating unit and (b) a cut through of the entrance region.

Acknowledgements

The financial support received from the ITS-LEIF Project (RII3 026015) is gratefully acknowledged. This work was supported by the “Stiftung Aktion Österreich-Ungarn”, the T&T Grant No. AT-7/2007, the Hungarian National Office for Research and Technology, as well as Austrian FWF (P17499), and the Hungarian Scientific Research Found OTKA (K72172).

a) Institut für Angewandte Physik, Technische Universität Wien.

[1] R.J. Berezky, G. Kowarik, K. Tókési, F. Aumayr, NIM. B (2012) in press.

8.4 Feasibility test for production and separation of ^{103}Pd

Z. Szűcs, S. Takács, M. Hunyadi, Z. Gácsi, J. R. Zeevaart^{a)}

^{103}Pd as a well-known Auger-emitter is commonly employed in brachytherapy, but the ultra-short range stopping of Auger-electrons can be more potentially exploited in applications of targeted radionuclide therapy in the future [1]. The no-carrier-added production of ^{103}Pd is practically possible through charged-particle induced reactions. However, separation techniques of ^{103}Pd from the target material (typically Rh), as well as its recovery by wet chemistry are expensive, and yields high amounts of radioactive waste. An alternative and more efficient procedure, called dry-distillation method (DDM), is based on differences between the isothermal vapor pressures of the radionuclide element and the target element. In an appropriately selected temperature region the diffusion and out-gassing rates of radionuclides from the solid matrix of the target material are enhanced [2,3].

Optimal irradiation parameters were determined in previous experiments at ATOMKI [4]. Separation of ^{103}Pd was demonstrated at the Isotope Separator Laboratory with an evaporating-condensing system (Fig. 1).



Figure 1. Evaporation-condensation system at the Isotope Separator Laboratory of ATOMKI.

The irradiated Rh foil was kept above 1800°C in vacuum for several hours. The evaluation of γ -spectra of the Rh foil and the ^{103}Pd condensed on a low-temperature substrate (Fig. 2). The analysis resulted in a radiochemical yield of about 99.5% for ^{103}Pd and a radionuclidic purity of better than 99% with respect to the level of ^{101}Rh in the end product.

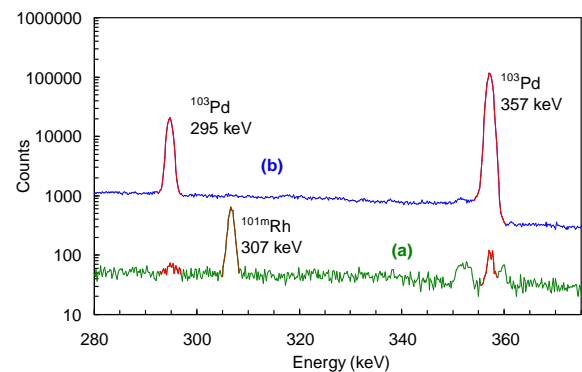


Figure 2. γ -spectra of the Rh matrix after heating (a) and of the ^{103}Pd condensed on the cooled substrate (b).

Acknowledgement

The work was partly supported by the Hungarian Tét Bilateral Cooperation (OMFB-00138/2009) and by the South African NRF (UID 68768).

a) Radiochemistry, NECSA & CARST, North West University - Mafikeng Campus, South Africa

[1] Z. Szűcs, J. Van Rooyen, J. R. Zeevaart. Applied Radiation and Isotopes, 2009, 67, 1401-1404

[2] I. E. Alekseejev, Radiochemistry 45, 2003, 429-456

[3] W. R. Jones, Partial Pressure Vacuum Processing - Parts I and II, Industrial Heating, 1997

[4] Z. Szűcs, S. Takács, J. Topkin, J.R. Zeevaart, Atomki Ann. Rep. 2009, 72

8.5 γ - and X-ray sensitivity comparison of a LEPS and a coaxial HPGe detector for astrophysical γ -process experiments

T. Szücs, G. G. Kiss, Z. Elekes, J. Farkas, Zs. Fülöp, Gy. Gyürky, Z. Halász, E. Somorjai

In our γ -process related studies charge particle capture cross sections are measured, from which the photodisintegration rates can be calculated applying the principle of detailed balance [1]. Many of these reactions can be measured via the activation method, where the sample is irradiated by the ion beam provided by an accelerator, the activated sample is transported to a shielded detector for activity measurement. From the detected activity, the reaction cross section can be derived. This method was successfully applied for the determination of several α induced reaction cross sections for the astrophysical γ -process at ATOMKI.

Recently, to determine the accumulated activity not only γ -ray but X-ray counting was performed [2,3]. To measure these X-rays a low energy photon spectrometer (LEPS) was used, which consists of a thin crystal of high purity germanium (HPGe). It has high efficiency for low energy γ - and X-rays and insensitive to the high energy γ -s. With a graded shield (4 mm Cu, 2 mm Cd, 8 cm Pb) it is more suited for the low energy counting experiments, compared to a coaxial HPGe detector in a 10 cm lead shield lined with 1 mm copper and 1 mm cadmium.

The minimum detectable activity (MDA) is a measure to test the performance of a counting system. The MDA is inversely proportional to the absolute detection efficiency (ϵ), and proportional to the square root of the background (B) and to the full width at half maximum (FWHM) energy resolution.

$$\text{MDA} \propto \frac{\sqrt{B} \cdot \text{FWHM}}{\epsilon}$$

The ratio of two MDAs is a good measure to compare the two counting systems, because it is independent from the source and counting parameters, only depends on the detectors. The following MDA ratio is calculated and shown in figure 1:

$$\frac{\text{MDA}_{\text{LEPS}}}{\text{MDA}_{\text{HPGe}}} = \sqrt{\frac{B_{\text{LEPS}}}{B_{\text{HPGe}}}} \frac{\epsilon_{\text{HPGe}}}{\epsilon_{\text{LEPS}}} \frac{\text{FWHM}_{\text{LEPS}}}{\text{FWHM}_{\text{HPGe}}}$$

It turned out that the LEPS for γ - or X-ray counting is preferable up to 350 keV. In the X-ray region (up to 100 keV) the LEPS can measure 4 time less activity. Between 100 keV and 250 keV it is still better than a factor of 2.

This finding opens the way to measure lower cross sections for the astrophysical γ -process, if the source emits high intensity γ - or X-rays in the low energy region.

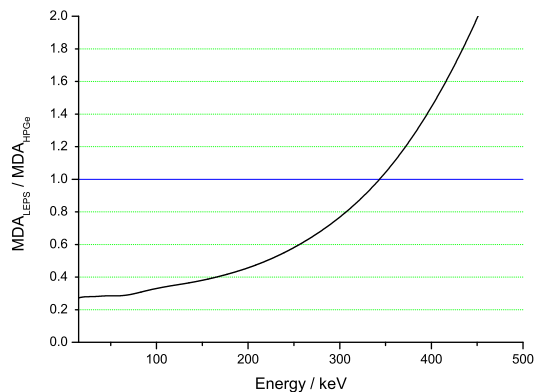


Figure 1. Minimum detectable activity ratio of the two mentioned counting systems.

- [1] G. G. Kiss *et al.*, PRL **101**, 191101 (2008)
- [2] G. G. Kiss *et al.*, Phys. Lett. B **695**, 419 (2011)
- [3] G. G. Kiss *et al.*, Nucl. Phys. A **867**, 52 (2011)

8.6 Simulations for a compact electron-positron spectrometer

T. Filep, A. Krasznahorkay, M. Csatlós, J. Gulyás

In the frame of the ENSAR (FP7) project, we are constructing a Compact Positron-Electron spectrometer (COPE) using toroidal magnetic field. It will be used for studying the internal pair creation process in nuclear transitions.

It will look like a miniaturized model of the ATLAS spectrometer at CERN at a scale of 1:100. The mean design parameters are high efficiency, good energy resolution and precise angle reconstruction. By our plans the size of this spectrometer would be limited to a diameter of about 30 cm and length about 20 cm, having 1 % energy- and 2° angular resolutions. The solid angle of the planned spectrometer will be 2π . It is necessary to develop a geometry in which the inhomogeneity of the field can be easily handled.

Prior to the construction it was necessary to perform computer simulations in order to avoid rough construction mistakes. The better approach of the reality with simulations is very important. The problem what we have to solve is very complicated. We need to simulate the magnetic field and trajectory of the particle moving in that field. We started our simulations using the PerMag software package [1].

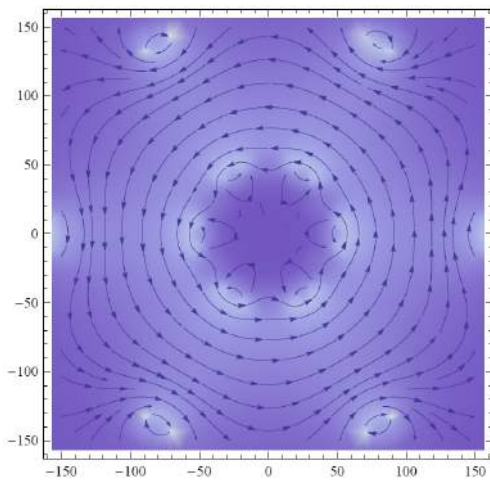


Figure 1. The magnetic field distribution calculated in 2 dimensions with the PerMag package.

From the result we learned the followings: 1) It has no meaning to cover the magnets with iron coat because it complicates the magnetic field. 2) It is not a good idea to form the magnetic one-segment from a big magnet and 12 smaller magnets. The fringing field of the small magnets significantly modifies the magnetic field distribution around the segment. On the other hand the construction of one segment from pieces is very difficult in reality. 3) The best shape for a segment which can easily be constructed is simple box.

The PerMag package could simulate the magnetic field only in 2D, but we wanted to do more precise simulation in 3D. The free package developed by the European Synchrotron Radiation Facility (ESRF) was used for the simulation of the magnetic field applying the finite element method (FEM) [2].

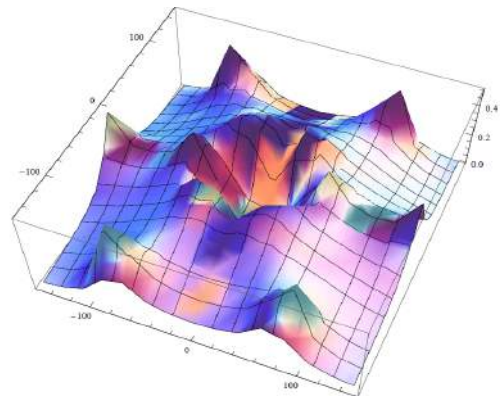


Figure 2. The magnetic field distribution calculated in 3 dimensions.

The resulted field was implemented into the Geant3 package [3]. In order to test the simulation of a charged particle trajectory using this field in Geant3, first we checked the shape of the expected trajectories with a simple and reliable Euler simulation method.

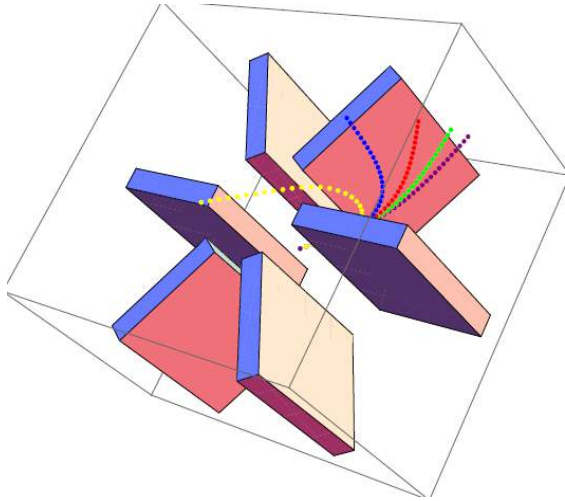


Figure 3. Trajectories of particles having different kinetic energies of 3,6,9,12,15 MeV calculated by the Euler-method.

Based on the results of the simulations we are planning to arrange six $100 \times 150 \times 15$ (mm) NbFeB N48 (1.42T) bars around a thin carbon fibre beam pipe having a radius of 35 mm as shown in Fig. 4.

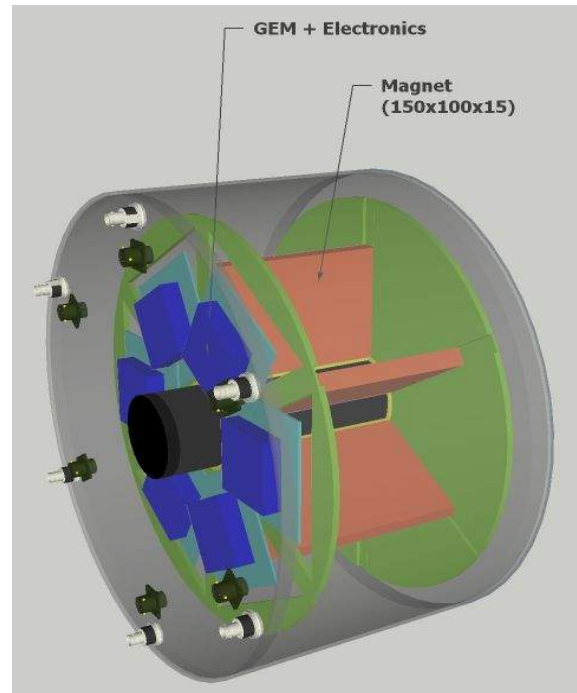


Figure 4. Mechanical layout of the spectrometer.

Acknowledgements

The work has been supported by the ENSAR FP7 project (project number: 262010) and the Hungarian OTKA Foundation No. K72566.

[1] <http://www.fieldp.com/permag.html>

[2] <http://www.esrf.eu/Accelerators/Groups/InsertionDevices/Software/Radia/Documentation/Introduction>

[3] <http://wwwasd.web.cern.ch/wwwasd/geant/>

8.7 Investigation of the absolute full-energy peak efficiency of a large LaBr₃ detector

L. Stuhl, A. Krasznahorkay, M. Csatlós, A. Bracco^{a,b}, N. Blasi^a, S. Brambilla^a, F. Camera^{a,b}, A. Giaz^{a,b}, J. Gulyás B. Million^a, L. Pellegrini^{a,b}, S. Riboldi^{a,b}, O. Wieland^a

In a recent experiment, we performed at GSI aiming at studying the neutron-skin thickness of ¹²⁴Sn, six large volume (3.5"x8") LaBr₃ scintillation detectors were used for detecting the γ -decay of the giant dipole resonance. These scintillators have very good energy and time resolution [1].

The aim of the present work was to study the absolute full-energy peak efficiency of such LaBr₃ detectors, in such conditions, which was used during the experiment (5 mm Pb, 3 mm Cu and 10 mm thick Al absorbers in front of the detectors).

The experiments were performed at the Institute of Nuclear Research of the Hungarian Academy of Sciences (ATOMKI). At low energies the efficiency was measured using ⁶⁰Co and ⁶⁶Ga gamma-ray emitters, which were placed at 25 cm from the front face of LaBr₃ detector.

At higher energies a version of the point-pair or two-line method [2] combining low-energy radioactive lines with proton resonance capture lines was applied in the efficiency calibrations. This procedure requires two gamma transitions in a cascade. The efficiency for the high-energy region was obtained by normalizing in to the low energy part in the overlapping range around 1.4 MeV (internal radiation). The target - detector distance was also 25 cm, and we got statistical errors less than 1%. The values of the following sources and reactions are used: ⁶⁰Co, ⁶⁶Ga, ²³Na(p, γ)²⁴Mg, ²⁷Al(p, γ)²⁸Si, ³⁹K(p, γ)⁴⁰Ca and ¹¹B(p, γ)¹²C, ⁷Li(p, γ)⁸Be. All targets were made by evaporation onto thick tantalum backings in vacuum (0.1 mm).

The absolute normalization of the efficiency was carried out by the ⁶⁰Co source (calibrated by the National Office of Measures of Hungary), which had an activity of 47.52 kBq during the measurement. The full absorption efficiency of the detectors were divided by their

solid angle, to get the internal efficiency.

The measured efficiencies were compared with the calculated ones (shown by the red curve in Fig. 1) obtained using a GEANT4 code. The simulated efficiency was normalized to the measured values, by the factor of 1.15. The results are in a good agreement with the experimental data. The efficiency decreases with the γ -ray energy from 19.7(6) % for 1173.2 keV to 4.5(5) % for 17.6 MeV. Without absorbers the above efficiencies were 32 % for 1,17 MeV and 18 % for 17.6 MeV, respectively.

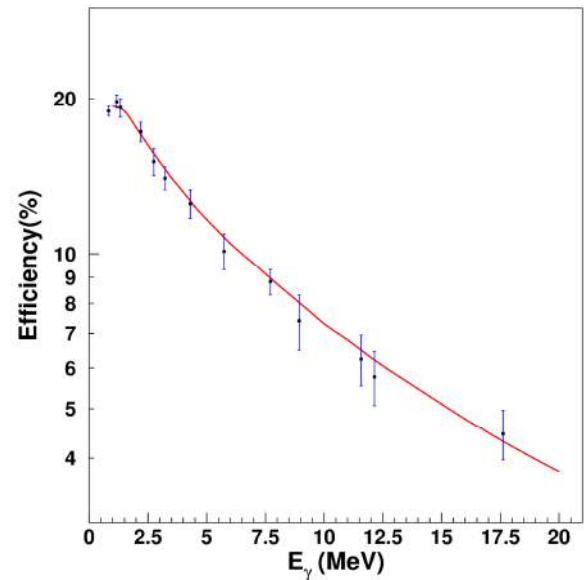


Figure 1. The efficiency of a LaBr₃ detector.

Acknowledgements

The work has been supported by the Hungarian OTKA Foundation No. K 72566.

- a) INFN, Istituto Nazionale di Fisica Nucleare, sezione di Milano, Milano, Italy
- b) Universita degli Studi di Milano, Dipartimento di Fisica, Milano, Italy

[1] R. Nicolini, *et al.*, NIMA **582** (2007) 554

[2] G.L.Molnar, *et al.*, NIMA **489** (2002) 140

9.1 International Workshop on Dynamics and Control of Atomic and Molecular Processes Induced by Intense Ultrashort Pulses

K. Tókési, R.J. Berezky, G. Sarkadi and G. Tókési

The workshop was organized by the Institute of Nuclear Research of the Hungarian Academy of Sciences (Atomki) Debrecen, Hungary from 27th of September till 30th of September 2011. The sponsor of the workshop was the COST Action CM0702 Chemistry with Ultrashort Pulses and Free-Electron Lasers: Looking for Control Strategies through Exact Computations (CUSPFEL). The workshop focused on all aspects of processes and phenomena stimulated by intense ultrashort pulses. The aim of the interdisciplinary work-

shop was to bring together senior scientists as well as students from countries working in diverse subfields closely connected to the common underlying theme of atomic and molecular processes induced by intense ultrashort pulses. Although the topic of the workshop was mainly belong to the theoretical physics, prominent representatives of the experimental physics from various Hungarian institutes (Budapest, Szeged, Pécs) attended on the workshop.



Figure 1. A lecture on the third day of the workshop.

The workshop contained only invited talks. The length of the oral presentations was 30 minutes. The conference program included 25 talks in 9 sessions. The sections of the program were:

1) Bio-molecules, 2) Control, 3) Strong Field, 4) Dissociation, 5) Photoelectron, 6) Ultrashort, 7) Scattering, 8) Ultrafast, 9) Control II.

During the workshop we had 32 registered participants from 9 countries (Austria, Croatia, France, Germany, Hungary, Romania, Spain, Switzerland, and UK).

Acknowledgements

The organizers would like to acknowledge the excellent cooperation of all contributors providing high standard lectures to ensure the success of the workshop. The organizers express their thanks for the support of the sponsors of the conference.

9.2 The FLAME project in Atomki

M. Hunyadi, N. Iski^{a)}

Eleven regions of eight Central European countries have launched the FLAME Project in 2010 (Future Laboratory for the diffusion and Application of innovation in Material Sciences and Engineering) to start and manage a new initiative of a network for innovation activities in the MS&E sector. The project aimed at supporting actors in the field of materials science and exploiting their research and commercial potentials. FLAME partners encourage trans-regional cooperation between R&D centres, universities, start-ups and SMEs by helping companies to distribute their innovations and supporting research in transferring results to the market.

The project will implement a new cooperation model: the ‘Future Lab’, where duly trained “regional facilitation coaches” will assist SMEs in accessing the whole Central European MS&E market and research potential. Each Future Lab will be specialized on thematic fields and help to make efficient use of local and regional potentials. The three Future Labs will be hosted by the Austrian, Italian and Slovenian partner organizations.

As the first step of project implementation in 2011 the competence and innovation maps within the participating regions were elaborated in order to list the relevant actors in the MS&E sector (Figure 1). In 2011, each project partner delegated two regional professionals as facilitation coaches to attend four training weeks across Europe. The facilitation coaches play an active role in the exchange of information and in motivating collaboration between research institutions and enterprises on technology based projects. The training sessions were located at four of the project partners: Kapfenberg/Austria (lead partner - Area m Styria); Warsaw/Poland (PP2 - Warsaw University of Technology); Debrecen/Hungary (PP5 - Atomki); Milan/Italy (PP10 - Innovhub). Each training session was devoted to a specific theme, which was treated and supported by the contribution of international experts increasing the competences of the facilitation coaches in different fields.



Figure 1. Competence and innovation landscape on the FLAME website. *Source:* <http://www.flameurope.eu/mse-actors-145.html>



- Project duration: 3 years
- Project period: 1/03/2010 - 31/08/2012
- Number of project partners: 11
- Target sector: Materials Science
- Target groups: SMEs, research institutions, intermediary organizations
- Regional facilitation coaches: M. Hunyadi (Atomki), N. Iski (Uni. of Debrecen)
- Official website: <http://www.flameurope.eu>



Acknowledgements

The project is implemented through the CENTRAL EUROPE programme co-financed by the ERDF.

- a) Knowledge and Technology Transfer Office, Uni. Debrecen

10.1 Events

Physicists' Days – 100 years of the nucleus

7-12 March 2011

László Stuhl (Atomki): *A trip into the heart of matter; Recent trends in nuclear physics*

Ádám Kiss (Eötvös Loránd University): *The role of accelerated particles in our life*

Gábor Veres (CERN / Eötvös Loránd University): *CERN - a modern Rutherford experiment*

Dezső Horváth (RMKI / Atomki): *Microcosmos - macrocosmos*

Traveling Exhibition of CERN

2-15 June 2011

ESFRI meeting

European Strategy Forum on Research Infrastructures

6 June 2011

WIRE conference

Week of Innovative Regions in Europe

7-9 June 2011

FLAME training

Future Laboratory for the Diffusion and Application of Innovation in Materials Science and Engineering

11-14 July 2011

Researchers' Night

23 September 2011

István Vajda (Budapest Uni. of Technology and Economics): *Superconductors in daily life - present and future*

Wordcampus

Workshop on Dynamics and Control of Atomic and Molecular Processes Induced by Intense Ultrashort Pulses

27-30 Sept 2011

Atomki Advisory Board meeting

6 October 2011

Celebration of Hungarian Science

Innovative pharmaceutical developments in Hungary - Symposium

10 November 2011

National Instruments Labview training

28 November - 2 December 2011

10.2 Hebdomadal Seminars

January 27

T. Fényes
Physics of hardons

February 3

I. Tüttő (SZFKI)
Nobel Prize in Physics 2010: Graphene

February 7

B. Rubio (Instituto de Física Corpuscular, Valencia, Spain)
From Rising to NUSTAR-FAIR

February 8

A. Diaz-Torres (University of Surrey, UK)
Reaction dynamics of weakly-bound nuclei at near-barrier energies

February 17

D. Horváth (Research Institute for Particle and Nuclear Physics, Budapest and Atomki)
Antihydrogene: producing, storing, spectroscopy

February 24

J. Gyulai (Institute for Technical Physics and Materials Science, Budapest)
SURVEY - or Rutherford's landing on the Hungarian Plane

March 2

A. Sófalvi (Haáz Rezső Museum, Szekelyudvarhely)
Latest results of the research of long fortifications

April 12

B.M. Nyakó
Proton-neutron pair interaction

April 13

L. Csernai (University of Bergen, Norway)
Collective hydrodynamical phenomena in ultrarelativistic heavy ion reactions

May 4

A. Kmety (Elsevier)
Introduction to the Scopus database

May 18

L. Palcsu
1. Using an ultrapure ^4He spike in tritium measurements of environmental water samples by the ^3He -ingrowth method
2. Research of temperatures of the past by noble gases dissolved in water
(Institute habilitation)

May 31

G. Bonheure (Plasma Physics Department, Brussels)
Measurement challenges in fusion plasmas

June 14

Zs. Fülöp and M. Pálinkás
State of affairs

June 16

D. Horváth (Research Institute for Particle and Nuclear Physics, Budapest and Atomki)
Search of supersymmetry at LHC

June 23

Gy. Radnai (Eötvös Loránd University, Budapest)
The first Solvay conference 100 years ago

June 24

J.F. Sharpey-Schafer (University of Western Cape, Belleville, South Africa)
Collective excitations of deformed nuclei and their coupling to single particle states

June 30

B. Singh (McMaster University, Hamilton, Ontario, Canada)
One-stop shopping for nuclear data

- July 19
C.T. Whelan (Old Dominion University, Norfolk, Virginia, USA)
Atomic processes relevant to inertial confined fusion experiments at the national ignition facility
- August 18
T. Jull (University of Arizona)
Cosmogenic nuclides in meteorites, lunar samples and terrestrial rocks
- August 25
E. Molnár (Research Institute for Particle and Nuclear Physics, Budapest)
Hydrodynamical modelling in ultra-relativistic heavy-ion collision
- September 8
H. Masui (Kitami Institute of Technology, Japan)
An aspect of the cluster-shell competition for light neutron-rich nuclei
- September 15
K. Arai (Nagaoka National College of Technology, Japan)
Tensor force manifestations in ab initio study of the ${}^2\text{H}(d,\gamma){}^4\text{He}$, ${}^2\text{H}(d,p){}^3\text{H}$ and ${}^2\text{H}(d,n){}^3\text{He}$ reactions
- September 20
G. Laricchia (Department of Physics and Astronomy, University College London)
Positron and positronium interactions with atoms and molecules
- September 22
L. Zolnai and D. Adománné-Zolnai
((MT)²!)?
- September 28
A. Makovec, T. Molnár, G. Pál, K. Szitha, M. Takács, L. Tóth
Reports on student-researcher's work in 2010-2011
- October 20
T. Fényes
Neutrino oscillation, leptogenesis, neutrino factories
- October 25
G. Demortier (University of Namur, Belgium)
The construction of the Cheops pyramid revisited based on IBA results
- October 28
T. Pálmai (Budapest University of Technology and Economics, Theoretical Physics Dept.)
Model independent potentials from phase shift series
- November 14
Zs. Révay (TU Munchen, FRM-II; Institute of Isotopes, Budapest)
Prompt-gamma activation analytical laboratories in Europe
- November 16
C. Stoyanov (Institute for Nuclear Research and Nuclear Energy, Bulgarian Academy of Sciences)
Valence shell excitations in even-even spherical nuclei within microscopic model
- November 24
Gy. Nagy, A. Ornelas, Z. Korkulu
Introduction of new colleagues in Atomki
- December 1
S. Aoyama (Niigata University, Niigata, Japan)
An ab-initio reaction calculation for four-nucleon scattering
- December 9
E. Bene
1. Analytic study of excited state effects in slightly bent tetra-atomic Renner-Teller molecules
2. Theoretical investigation of charge exchange processes in ion-atom collisions
(Institute habilitation)
- December 15
D. Berényi
Alternative energy sources – a critical approach
- December 22
D. Horváth (Research Institute for Particle and Nuclear Physics, Budapest and Atomki)
How to measure neutrino speed?

10.3 Awards

Zsolt Dombrádi and Barna Nyakó
Physics Prize of the Hungarian Academy of Sciences

János Farkas and Szabolcs Szilasi
Young Scientist Award of Atomki

György Gyürky
Roland Eötvös Physical Society: Budó Ágoston Award

Árpád Z. Kiss
Roland Eötvös Physical Society: ELFT Medal

Rezső Lovas
Officer's Cross Order of Merit of the Republic of Hungary
Membership Academia Europaea
Pro Scientia Award

Károly Pál and Tamás Vértesi
Szalay Sándor Award of Atomki

Pálinkás Miklósné dr.
Special Award by the Faculty of Economics and Business Administration, University of Debrecen

Sándor Mészáros
Presentation Prize by National Instruments

József Molnár
Dennis Gabor Award

Dóra Sohler
Roland Eötvös Physical Society: Selényi Pál Award

Géza Székely
Regard of the General Secretary of MTA

Ferenc Tárkányi
Roland Eötvös Physical Society: Szalay Sándor Award

10.4 List of Publications

The total number of publications in 2011 was 445, of which 266 SCI papers, 147 other papers and proceedings, 6 theses, 5 diploma works, 13 books or book chapters and 8 edited works.

The list of the Institute's publications can be found on-line at:

<http://www.atomki.hu/p2/years/yea02011.htm>

10.4.1 Highlights

Highlighted papers of 2011:

8 January 2011

Evidence for a spin-aligned neutron-proton paired phase from the level structure of ^{92}Pd

Nature 469, 68-71 (2011)

B. Cederwall, F. Ghazi Moradi, T. Bäck, A. Johnson, J. Blomqvist, E. Clément, G. de France, R. Wadsworth, K. Andgren, K. Lagergren, A. Dijon, G. Jaworski, R. Liotta, C. Qi, *B. M. Nyakó*, J. Nyberg, M. Palacz, H. Al-Azri, A. Algora, G. de Angelis, A. Ataç, S. Bhattacharyya, T. Brock, J. R. Brown, P. Davies, A. Di Nitto, *Zs. Dombrádi*, A. Gadea, *J. Gál*, B. Hadinia, F. Johnston-Theasby, P. Joshi, K. Juhász, R. Julin, A. Jungclaus, *G. Kalinka*, S. O. Kara, A. Khaplanov, J. Kownacki, G. La Rana, S. M. Lenzi, *J. Molnár*, R. Moro, D. R. Napoli, B. S. Nara Singh, A. Persson, F. Recchia, M. Sandzelius, J.-N. Scheurer, G. Sletten, *D. Sohler*, P.-A. Söderström, M. J. Taylor, *J. Timár*, J. J. Valiente-Dobón, E. Vardaci & S. Williams

8 February 2011

Determining reaction cross sections via characteristic X-ray detection: α -induced reactions on ^{169}Tm for the astrophysical γ -process

Physics Letters B 695 (2011) 419-423

G. G. Kiss, T. Rauscher, *T. Szücs*, *Zs. Kertész*, *Zs. Fülöp*, *Gy. Gyürky*, C. Fröhlich, *J. Farkas*, *Z. Elekes*, *E. Somorjai*

24 March 2011

Classical trajectory Monte Carlo model calculations for ionization of atomic hydrogen by 75-keV proton impact

Physical Review A 82, 052710 (2010)

L. Sarkadi

21 April 2011

ECR plasma photographs as a plasma diagnostic

Plasma Sources Science and Technology 20 (2011) 025002 (7)

R. Rácz, *S. Biri*, *J. Pálinkás*

11 May 2011

Activation of Nonlocal Quantum Resources

Phys. Rev. Lett. 106, 060403 (2011)

M. Navascués and *T. Vértesi*

5 July 2011

$^4\text{He}^+$ ion beam irradiation induced modification of poly(dimethyloxane).
Characterization by infrared spectroscopy and ion beam analytical techniques
Langmuir 27 (2011) 7:3842

R. Huszánk, D. Szikra, A. Simon, S.Z. Szilasi, I.P. Nagy

8 August 2011

A 9-year record of stable isotope ratios of precipitation in Eastern Hungary:
Implications on isotope hydrology and regional palaeoclimatology

Journal of Hydrology 400 (2011) 144-153.

G. Vodila, L. Palcsu, I. Futó, Zs. Szántó

7 September 2011

Two-photon laser spectroscopy of antiprotonic helium and the antiproton-to-electron mass ratio

Nature 475 (2011) 484

M. Hori, A. Sótér, D. Barna, A. Dax, R. Hayano, S. Friedreich, B. Juhász, T. Pask, E. Widmann, D. Horváth, L. Venturelli & N. Zurlo

4 October 2011

Trajectories of S-matrix poles in a new finite-range potential

Phys. Rev. C 84, 037602 (2011)

A. Rácz, P. Salamon, T. Vertse

4 November 2011

Spectroscopy of $^{39,41}\text{Si}$ and the border of the $N = 28$ island of inversion

Physics Letters B 703 (2011) 417-421

D. Sohler, S. Grévy, Zs. Dombrádi, O. Sorlin, L. Gaudefroy, B. Bastin, N.L. Achouri, J.C. Angélique, F. Azaiez, D. Baiborodin, R. Borcea, C. Bourgeois, A. Buta, A. Burger, L. Caceres, R. Chapman, J.C. Dalouzy, Z. Dlouhy, A. Drouard, Z. Elekes, S. Franchoo, S. Iacob, I. Kuti, B. Laurent, M. Lazar, X. Liang, E. Liénard, S.M. Lukyanov, J. Mrazek, L. Nalpas, F. Negoita, F. Nowacki, N.A. Orr, Yu.E. Penionzkhevitch, Zs. Podolyák, F. Pougheon, A. Poves, P. Roussel-Chomaz, M. Stanoiu, I. Stefan, M.G. St-Laurent

3 December 2011

Reciprocity in the degeneracies in some tetra-atomic molecular ions

Journal of Chemical Physics 135 (2011)8:4101(6)

E. Bene, T. Vértesi, R. Englman

20 December 2011

Refractive index depth profile and its relaxation in polydimethylsiloxane (PDMS) due to proton irradiation

Materials Chemistry and Physics 131 (2011) 370-374

S.Z. Szilasi, J. Budai, Z. Pápa, R. Huszánk, Z. Tóth, I. Rajta

Index

- Algora A., 1
Almehed D. , 37
Álvarez R., 71
Andrási D., 86
Angyal A., 85
Arbó D.G., 46
Astier A., 35
Aumayr F., 92
- Barczy A., 80
Barnabás I., 83
Bazacco D., 35
Beddies G., 62
Bednarczyk P., 35
Beke D.L., 62
Benkő I., 87
Benkő K., 87
Berezky R.J., 41, 51, 52, 72, 92, 98
Bernhardt D., 55, 56
Berzi I., 88
Biri S., 60, 67, 76, 88
Björkhage M., 57
Blasi N., 97
Borbély S., 48
Bordeanu C., 31
Borovik, Jr. A.A., 55, 56
Boston A.J., 35, 37
Bracco A., 97
Brännholm L., 57
Brambilla S., 97
Buforn N., 35
Buhr T., 56
Burgdörfer J., 42, 73
- Camera F., 97
Cederquist H., 57
Chantler H.C. , 35, 37
Charnovych S., 63, 64, 74, 75
Chiara C.J., 35, 37
Clark R.M., 35
Clark R.M. , 37
Coster D., 58, 77
Cromaz M., 35
Cromaz M. , 37
Csatlós M., 1, 95, 97
Cserháti Cs., 67
Csige I., 74
Csige L., 1
Csik A., 62–67, 74–76, 87, 91
- Daróczi L., 74
Dassanayake B.S., 51, 52
Descovich M., 35
Descovich M. , 37
Doblhoff-Dier K., 42
Dombrádi Zs., 1, 35
DuBois R.D., 45
- Elander N., 53
Elekes Z., 31, 32, 94
Erdélyi G., 63
- Fallon P., 35
Fallon P. , 37
Farkas J., 31, 36, 94
Feist J., 42
Fényes T., 1
Filep T., 95
Fossan D.B., 35, 37
Fox C., 35
Fraser P.R., 39
Frauendorf S. , 37
Fülöp Zs., 31–34, 36, 94
Furu E., 84, 85
Futó I., 78, 79
- Gácsi Z., 1, 74, 75, 93
Gál G.A.B., 67
Galaviz D., 33
Géresi K., 87
Giaz A., 97
Gizon A., 35
Gizon J., 35
Glodán Gy., 64
Gulyás J., 1, 95, 97
Guray R. T., 34
Gyürky Gy., 31–34, 36, 94
- Hakl K., 65, 66
Halász Z., 31, 34, 36, 94
Hecht A.A., 35, 37
Hegman N., 91
Herczku P., 40, 59
Hess P.O., 39
Holste K., 55, 56

Hunyadi M., 1, 74, 75, 93, 99
 Huszánk R., 68, 69
 Iski N., 99
 Jakab G., 81
 Janovics R., 83, 84
 Johansson H.A.B., 57
 Joó K., 80
 Juhász Z., 59, 67
 Jull A.J.T., 81
 Jungen Ch., 54
 Kashperka I., 57
 Kern Z., 83
 Kertész Zs., 84, 85
 Kintz N., 35
 Kis-Varga M., 74
 Kiss Á.Z., 85
 Kiss G.G., 31, 33, 34, 94
 Kiss Zs., 48
 Koike T., 35, 37
 Kokavecz J., 68
 Kokenyesi S., 63, 64, 75
 Korkulu Z., 34
 Kormámy Z., 88
 Kovács B., 86
 Kovács S.T.S., 40, 59
 Kövér Á., 40, 55, 56
 Kowarik G., 92
 Krasznahorkay A., 1, 95, 97
 Kuti I., 1, 35, 37
 Lábadi Z., 66
 Larson Å., 53
 Lee I.Y., 35
 Lee I.Y., 37
 Lemell C., 42, 73
 Lévai G., 29, 39
 Lovics R., 65, 66
 Lukas W., 83
 LUNA collaboration, 32
 Lunardi S., 35
 Macchiavelli A.O., 35, 37
 Major I., 84
 Major Z., 79, 82
 Makogon Yu.N., 62
 Marinkovic B.P., 73
 Máté Z., 1, 33
 Mátéfi-Tempfli M., 73
 Mátéfi-Tempfli S., 73
 Mezei J.Zs., 53, 54
 Million B., 97
 Milosavljevic A.R., 73
 Misra D., 57
 Mogyorósi M., 86
 Mohr P., 33, 38
 Molnár M., 80, 81, 83, 84
 Moreh R., 70
 Mukoyama T., 43, 44
 Müller A., 55, 56
 Nagashima Y., 43
 Nagele S., 42
 Nagy G.U.L., 85
 Nagy I., 69
 Nagy L., 48
 Nándori I., 30
 Nolan P.J., 35
 Nyakó B.M., 1, 35
 O'Mullane M., 58
 Orbán A., 57
 Ornelas A., 33
 Ozkan N., 34
 Palásthy B., 50
 Palcsu L., 79, 82
 Pálinkás J., 60
 Papp L., 79, 82
 Papp T., 74
 Paripás B., 50, 87
 Paul E.S., 35, 37
 Pavlova E.P., 62
 Pazourek R., 42
 Pellegri L., 97
 Petrache C.M., 35
 Rác R., 60, 76, 77, 88
 Rajta I., 41, 67–69, 72, 87, 91
 Ratter K., 85
 Rauscher T., 33
 Reinhard P., 57
 Riboldi S., 97
 Ricsóka T., 55
 Ricz S., 55, 56
 Rinyu L., 80
 Rosén S., 57
 Roueff E., 54

Sampson J.A., 35
 Sarkadi G., 87, 98
 Sarkadi L., 40
 Schiessl K., 73
 Schippers S., 55, 56
 Schmidt H.T., 57
 Schneider I.F., 54
 Scraggs H.C., 35
 Sidorenko S.I., 62
 Sinkovic P., 85
 Sohler D., 1, 35, 37
 Somorjai E., 31–34, 36, 94
 Sonnabend K., 33
 Starosta K., 35, 37
 Stuhl L., 1, 97
 Sulik B., 59, 67
 Sümegi P., 81
 Svingor É., 80
 Szabó B., 87
 Szikra D., 69
 Szilasi S.Z., 67–69, 91
 Szoboszlai Z., 85
 Szücs T., 31, 34, 36, 94
 Szűcs Z., 74, 86, 93

 Takács I., 87
 Takács S., 86, 93
 Takáts V., 65, 66
 Tanis J.A., 51, 52
 Thomas R.D., 57
 Timár J., 1, 35, 37
 Tőkési G., 98
 Tőkési K., 41–52, 58, 70–73, 77, 87, 92, 98
 Török Zs., 85
 Tornyai T., 1
 Tóth J., 66, 74, 87
 Tskhakaya D., 77

 Ungvári É., 87

 Vácsi T., 69
 Vad K., 41, 65, 66, 76
 Vajta Zs., 1
 Varga D., 55, 56
 Verbitska T.I., 62
 Vető I., 79
 Vodila G., 78, 79
 Vos M., 70

 Wadsworth R., 35, 37

 Walker A., 35
 Werner J., 57
 Wieland O., 97

 Yalcin C., 34
 Yépez-Martínez H., 39
 Yubero F., 71

 Zeevaart J. R., 93
 Žilges A., 33
 Žitnik M., 50
 Zolnai L., 1, 35